Excursions in Chemical Dynamics

by

Shervin Fatehi

A dissertation submitted in partial satisfaction of the
requirements for the degree of
Doctor of Philosophy

in

Chemistry

in the

GRADUATE DIVISION
of the
UNIVERSITY OF CALIFORNIA, BERKELEY

Committee in charge:
Professor William H. Miller, Co-chair
Professor Richard J. Saykally, Co-chair
Professor Robert G. Littlejohn

Fall 2010

Excursions in Chemical Dynamics

Abstract

Excursions in Chemical Dynamics

by

Shervin Fatehi
Doctor of Philosophy in Chemistry

University of California, Berkeley

Professor William H. Miller, Co-chair
Professor Richard J. Saykally, Co-chair

As early as 1929, Dirac was sufficiently confident in the new quantum theory to assert that the physical laws underlying all chemistry were known; what remained, then, was to find tractable approximations within which to apply them. The most famous of these approximations, due to Born and Oppenheimer, partitions chemistry as formulated quantum mechanically into separate electronic and nuclear problems. While treatments of electronic structure within this framework are now routine among chemists, nuclei are still often treated classically. It is impossible, however, to be *certain* as to whether nuclear quantum effects will contribute to the physics of any given system. The present work addresses these effects at varying levels of approximation and in the context both of concrete systems (aqueous solutions and isolated molecules) and general methodology.

After a brief introduction in Chapter 1, we proceed in Chapter 2 to discuss recent X-ray photoelectron spectra on aqueous hydroxide solutions, which were seen to exhibit the off-site Auger decay process known as intercoulombic decay (ICD). Arguments were made regarding the necessary conditions for ICD to occur — specifically, that it would take place selectively along a hydrogen bond donated by the hydroxide ion. This mechanistic claim ties in with an ongoing controversy over the solvation structure of hydroxide and would constitute decisive evidence for the hypercoordinated model (which allows transient hydrogen bond donation by hydroxide) over the proton-hole model (which does not).

We have performed X-ray absorption calculations using the eXcited electron and Core Hole (XCH) method that indicate that hydrogen-bond donation is not a prerequisite for ICD in this system. Additional calculations suggest that X-ray absorption techniques are also unlikely to be able to distinguish between the two solvation models. In reaching these conclusions, we stress that there are general theoretical criteria for the occurrence of ICD and suggest that they may be used predictively. We further propose that our criteria can be combined with the XCH method to aid in the rational design of a new type of chemo-/radio-

therapy protocol for cancer treatment. In particular, we are preparing a proof-of-principle experiment on a model biological solution of bismuth, citrate, and urea.

In Chapter 3, we address nuclear motion explicitly. Several models of the X-ray absorption spectrum of nitrogen gas (N_2) are studied in the context of the standard Born-Oppenheimer approximation and XCH. Systematic improvements are made to an initially classical model that includes nuclear motion exactly, beginning with the substitution of the quantum mechanical nuclear density in the bond length R for its classical counterpart, followed by the addition of zero-point energy and other level-shifting effects, and finally the inclusion of explicit rovibrational quantization of both the ground and excited states. The quantization is determined exactly using the Colbert-Miller discrete variable representation (DVR), with further details provided in a pair of appendices.

It is shown that the spectrum can be predicted semiquantitatively within this simple framework and that it compares respectably well with the prediction obtained using more accurate potentials. With respect to nuclear dynamics, the key lesson is that quantization of nuclear motion is absolutely essential if one wishes to capture fine structure in the spectrum; simpler approaches will, at best, properly reproduce a sharp absorption edge.

In Chapter 4, we examine a method for the approximate inclusion of true dynamical effects associated with moment-to-moment nuclear motion. In particular, we study ring polymer molecular dynamics (RPMD), which (though developed recently) has already proven to be a useful theory for the calculation of a wide variety of properties of chemical systems. It is founded, however, on a heuristic extension of the rigorously-derived method of path integral molecular dynamics (PIMD). We attempt to *derive* the method by way of judicious approximations to exact expressions for the correlation function and, that failing, by "reverse engineering." These attempts do not succeed, in general, but may eventually provide a means of obtaining the method in the case of a harmonic oscillator, for which it is exact. At the very least, the expressions obtained offer further evidence that RPMD is a reasonable extension of rigorous methods.

In memory of my grandparents

The detail of the pattern is movement,
As in the figure of the ten stairs.

T. S. Eliot, "Burnt Norton"

Contents

List of Figures

List of Tables

Acknowledgments

Bill Miller has been a wonderfully patient advisor: He gave me the space, the time, the security, and the sense of freedom required to pursue interesting dead ends and to make many instructive mistakes. At the same time, he was never without a good idea or an interesting mathematical puzzle for me to tackle on the requisite "big sheet of paper" — not that I always did. Though I haven't been the most compliant of students, I could not have seen through any of the research discussed in this dissertation without the concepts and the modes of thinking that Bill imparted to me. In particular, I've been impressed by the way Bill combines physical intuition and a deep command of what one might call "mathematical chemical physics" with a relentless drive to tinker with methods and to find out what works. I hope to continue developing my skills along similar lines, and I thank Bill for having set a fine example. Thanks are also due to Margaret Ann Miller for the stimulating conversation and plentiful (and delicious) Italian food served up at our sporadic group dinners!

My friend and collaborator Craig Schwartz got me doing spectroscopy again after several years' hiatus. A few innocent questions about path integration soon turned into a joint effort to disentangle the nuclear contributions to the X-ray absorption spectrum of N_2. Since that effort ultimately produced a significant fraction of this dissertation, I can't thank him enough. Craig has also done more than his share to keep me physically active, irreverent, and inebriated on a world-historical scale.

The senior partners in our collaboration, Rich Saykally and David Prendergast, have provided me with more guidance, encouragement, and editing help than I would have expected when we first started out — not least since Rich ultimately became co-chair of my dissertation committee, for which I'm deeply grateful. I also appreciated the occasional energetic discussion with Rich in his eponymous group's meetings, as well as his many helpful (and prompt!) comments on the present manuscript. David, for his part, has spent hour upon hour with me and Craig, piecing together new ideas and new papers; has given me career advice and kept me abreast of job opportunities; and invited me to present some of this work to the theorists at the Molecular Foundry, which was a real treat. I hope we'll continue working together in the future.

Several other professors have helped steward me through the (at times rather painful) process of finishing my degree. Bill, Phill Geissler, Martin Head-Gordon, and Hitoshi Murayama taught me innumerable useful things in their classes, and the project I did for Martin's version of 295 may yet turn into a paper. Phill was slated for double duty on the qual. and dissertation committees, but he was let off the dissertation hook (as he put it) once Rich came on board. Nevertheless, I'm glad that he would've been willing to stay on! Robert Littlejohn eventually did serve on both committees, which I really appreciated.

Alex Pines, the chair of my qualifying exam committee, was especially helpful during the whole of that arduous process. I only wish I'd heeded his advice and cozied up to concrete chemical problems sooner. Joel Moore and Birgitta Whaley filled out the committee and asked some probing questions — thanks!

Because a fair amount of my time at Berkeley has been spent teaching as well as learning, and because I hope to spend as much or more time teaching as doing research in the future, I'd be remiss if I didn't thank the professors involved: Heino Nitsche (1A), Ron Cohen (4A), Bill Miller and Haw Yang (120A), and Charles Harris (122/222). Each of them had a unique spin on lecturing and constructing assignments, and I learned valuable lessons from each. And I'm certain I'll cherish the memory of Heino's nonchalance after being lit on fire during a demonstration (and the story of his radioactive cat) for years to come.

The undergraduate teaching staff — specifically Michelle Douskey, Bob Lamoreaux, and Dante Valdez — have been a huge help as well. I appreciate Michelle's perspective on grad. school and helpful career advice, Bob's humorously jaundiced view of bureaucracy and resourcefulness in getting me plum teaching positions, and Dante's genial (but knowledgeable) company throughout 4A. My 120A student Clarion Tung deserves mention, too: He's become a theoretical chemist, studying under Christoph Dellago in Austria — well done!

The members of the Miller group have been valuable companions on this journey. Tom Miller, my collaborator in exploring the foundations of ring polymer molecular dynamics, spent more time than he really had to ponder ideas with me and keep me optimistic in the run-up to my qualifying exam. Jian Liu kindly explained (and re-explained) a huge number of details about the initial value representation to me. Other excellent labmates and friends include Nandini Ananth, Mike Small, Cristian Predescu, Guohua Tao, Charulatha Venkatamaran, and (especially) David W. H. Swenson. Besides being great fun to talk to, administrative whiz Cheryn Gliebe has done some heroic things on my behalf, including grabbing a semester's funding practically out of thin air. I won't soon forget!

I was briefly a member of David Chandler's group. As such, I acknowledge his kind support for that first year and in the subsequent search for a new advisor. David Kelsey, Sun Kim, and Adam Willard, who entered the group with me, were fun to work with and very supportive during that period and since. Matthew Wyndham, the group's administrative assistant at the time, was a big help to me in navigating the California residency process.

Friends have helped me to keep work in perspective. Leslie Dewan was especially important for the first two years, giving me love and stability when I sorely needed it. In addition to those already mentioned, friends at Berkeley include (but were far from limited to) Lauren Comfort, Greg Dallinger, Lester Hedges, Katherine Koen, Westin Kurlancheek,

Keith Lawler, Dale Otten, my esteemed co-GSI Drew Rollins, Chris Ryan, Sassan Sheikholeslami, Rob Sindelar, and Janel Uejio, all of whom inspired frequent breaks. (Keith also provided the LaTeX template used to typeset this thesis per Berkeley standards — a godsend. I can't imagine how painful it would've been to use Word.) The following local friends from MIT also deserve thanks for their ready companionship at various concerts, meals, and debauches: Kelly Clancy, Dan Good, May Lim, Dan McAnulty, Gene Shuman, Nemanja Spasojevic, T. J. Torres, and my dear old "rheumy," George Waksman. Those college friends elsewhere in the country know who they are, I suspect, and are mostly drawn from the ranks of Random Hall's illustrious Fort Awesome and TEΦ.

Finally, support from my family has been instrumental throughout my time at Berkeley, both emotionally and materially. Space is insufficient and eloquence is lacking to do justice to my gratitude; I hope the coming months and years will serve to illustrate what I can't express.

With that said, I'll acknowledge my official sources of funding once more (and with feeling): This work was supported by the Director, Office of Basic Energy Sciences, Office of Science, U. S. Department of Energy under Contract No. DE-AC02-05CH11231 through the Lawrence Berkeley National Laboratory Chemical Sciences Division. Computational resources were provided by the National Engineering Resource for Supercomputing, a DOE Advanced Scientific Computing Research User Facility, and the Lawrencium computational cluster resource provided by Scientific Computing Services at LBNL. Funding was also provided by National Science Foundation Grant No. CHE-0809073.

Chapter 1

Introduction

1.1 Chemistry as a quantum problem

As early as 1929 [1], Dirac was sufficiently confident in the new quantum theory to assert that

> [t]he underlying physical laws necessary for the mathematical theory of a large part of physics and the whole of chemistry are ... completely known, and the difficulty is only that the exact application of these laws leads to equations much too complicated to be soluble.

Although this statement was founded partially on the assumption that relativity would be of little or no consequence for chemistry — which has not proven wholly justified in the case of heavier elements, like gold [2, 3] — the subsequent development of theoretical chemistry has largely borne out Dirac's claim.

1.2 Chemistry formulated exactly

At the molecular level, (non-relativistic) chemistry reduces to the quantum mechanics of assemblages of electrons and nuclei interacting through the Coulomb force. The governing equation of chemistry is thus the time-dependent Schrödinger equation (TDSE)

$$i\hbar\frac{\partial}{\partial t}|\Psi(t)\rangle = \hat{H}|\Psi(t)\rangle \tag{1.1}$$

with the Hamiltonian operator (in atomic units)

$$\hat{H} = -\sum_i \frac{1}{2}\nabla_i^2 + \sum_{i>j}\frac{1}{r_{ij}} - \sum_A \frac{1}{2M_A}\nabla_A^2 - \sum_{i,A}\frac{Z_A}{r_{iA}} + \sum_{A>B}\frac{Z_A Z_B}{R_{AB}} \tag{1.2}$$

Lower-case indices label the electrons of mass $m_e = 1$ and charge $-e = -1$; their Cartesian coordinates are given by $\vec{r}_i = [x_i, y_i, z_i]^T$. Upper-case indices label the nuclei of mass M_A and charge Z_A; their coordinates $\vec{R}_A$ are defined analogously. Interparticle distances of the type appearing in the latter three terms are defined, for example, by $r_{ij} = |\vec{r}_i - \vec{r}_j|$.

The first and third terms in Equation 1.2 are the total electronic and nuclear kinetic energy operators; the second and fourth terms (the interelectronic repulsion and nuclear-electronic attraction) together constitute the electronic potential energy; and the last term describes the internuclear repulsion. We rewrite the Hamiltonian accordingly,

$$\hat{H} = \hat{T}_e + V_e(\vec{\mathbf{r}}, \vec{\mathbf{R}}) + \hat{T}_N + V_N(\vec{\mathbf{R}}) \tag{1.3}$$

with bold-faced vectors denoting the full set of electronic or nuclear coordinates.

In principle, all we must do to obtain a complete description of *any* chemical system is to specify the number of electrons, the types and numbers of nuclei, and the initial state of the system $|\Psi(0)\rangle$. Then we must solve Equation 1.1. Setting aside for the moment Dirac's worries regarding the tractability of such a procedure, let's consider how one might carry it through.

$|\Psi(0)\rangle$ will (in general) be a complicated function of all of the electronic and nuclear coordinates, and it need not be anything like a typical wavefunction for the system (since the initial condition of interest may be nonequilibrium). Even so, a typical starting point is to make the separation of variables $|\Psi(t)\rangle \approx F(t)|\Psi\rangle$ yielding the equations

$$\begin{aligned} \hat{H}|\Psi\rangle &= E|\Psi\rangle \\ \dot{F}(t) &= -\frac{i}{\hbar}F(t) \end{aligned} \tag{1.4}$$

such that we obtain the set of stationary states $\{|\Psi_n(t)\rangle\}$ defined by

$$\begin{aligned} \hat{H}|\Psi_n\rangle &= E_n|\Psi_n\rangle \\ F_n(t) &= e^{-\frac{it}{\hbar}E_n} \end{aligned} \tag{1.5}$$

This procedure has the ancillary benefit of allowing us to infer the identity of the time-evolution operator, $U(t) = e^{-\frac{it}{\hbar}\hat{H}}$.

Note that we have chosen to set $F_n(0) = 1$. We incur no loss of generality in the process, because we will express $|\Psi(0)\rangle$ as a linear combination in the basis of stationary states; the $F_n(0)$ will then be absorbed into the expansion coefficients c_n:

$$|\Psi(0)\rangle = \sum_n c_n|\Psi_n\rangle \tag{1.6}$$

The solution of the time-dependent Schrödinger equation for our system at time t is, at last,

$$\begin{aligned} |\Psi(t)\rangle &= U(t)|\Psi(0)\rangle \\ &= \sum_n c_n e^{-\frac{it}{\hbar}E_n}|\Psi_n\rangle \end{aligned} \tag{1.7}$$

1.3 Exact chemistry is intractable

There is, of course, a catch: Very few systems, chemical or otherwise, have a time-independent Schrödinger Equation 1.4 (TISE) that is exactly solvable — and most of these describe single particles in one dimension (or multidimensional generalizations of the same). Examples include important model systems like the free particle, the harmonic and Morse oscillators, the rigid rotor, the hydrogenic atom, and the Eckart barrier. Among many-body systems, the most notable example is the hydrogen molecular ion H_2^+.

This limited set of model systems clearly will not suffice for the chemist, whose interests span the range from single atoms to complex mixtures of reagents in multiple phases. It is necessary, then, to solve Equation 1.4 numerically. But even this concession to complexity is more easily suggested than made: Suppose we wish to solve the Schrödinger equation by quadrature on a spatial grid. Each electron or nucleus contributes three degrees of freedom to the configurational space of the system, for a dimensionality of $d = 3P$ (where P denotes the total number of particles). Assuming that we allot an equal number of grid points M to each degree of freedom, the grid size will scale as M^d — that is, exponentially. This abysmal scaling behavior has limited the exact solution of the Schrödinger equation to very small systems [4].

1.4 The Born-Oppenheimer approximation

Dirac and his contemporaries knew that one would have to resort to approximations in order to do chemistry [1]:

> ... [A]pproximate practical methods of applying quantum mechanics should be developed, which can lead to an explanation of the main features of complex atomic systems without too much computation.

The most famous and fundamental of these approximations is due to Born and Oppenheimer [5, 6]. The TISE is itself solved using a direct product form, $|\Psi\rangle = |\psi\rangle \otimes |\chi\rangle$, separating electronic states $|\psi\rangle$, chosen to be dependent on the nuclear coordinates only

parametrically, and nuclear states $|\chi\rangle$, which do not depend on the electronic coordinates. The standard form of the approximation then yields a pair of eigenvalue equations

$$\begin{aligned} \left[\hat{T}_e + V_e(\vec{\mathbf{r}};\vec{\mathbf{R}})\right]|\psi_n\rangle &= E_e^{(n)}(\vec{\mathbf{R}})|\psi_n\rangle \\ \left[\hat{T}_N + V_N(\vec{\mathbf{R}}) + E_e^{(n)}(\vec{\mathbf{R}})\right]|\chi_k^{(n)}\rangle &= E|\chi_k^{(n)}\rangle \end{aligned} \tag{1.8}$$

which may be solved separately. The most general solution to the TISE then becomes a linear combination of the direct-product states,

$$|\Psi\rangle \approx \sum_{n,k} c_{nk}|\psi_n\rangle \otimes |\chi_k^{(n)}\rangle \tag{1.9}$$

Implicit in this division between the electronic and nuclear degrees of freedom is the assumption that nuclear motion will take place on a single electronic potential energy surface and, furthermore, will not itself give rise to coupling between them (a phenomenon known as vibronic coupling). Put more precisely, it is assumed that the matrix element $\langle\psi_m|\hat{T}_N|\psi_n\rangle = \hat{T}_N\delta_{mn}$, such that the full TISE for direct-product states partitions cleanly into the form given in Equation 1.8.

1.5 Electronic structure and nuclear dynamics

As we have seen, the Born-Oppenheimer approximation separates the problem of solving the TISE into electronic and nuclear components. By the time Dirac had declared the foundations of chemistry complete, a number of techniques for treatment of the electronic structure had already been developed, such as the Hartree self-consistent field method and Heitler-London valence bond theory [1]. Electronic structure theory has remained a fertile area of research, and there is now a veritable cornucopia of methods (some based on the wavefunction, others on the density) [7–9].

Solving the electronic structure problem within a variational framework yields the nuclear potential energy surface associated with the electronic ground state. One may then proceed to solve the nuclear Schrödinger equation of Equation 1.8 — perhaps further separating nuclear vibrational and rotational motion using the Eckart conditions [10], treating vibrations using normal modes or other methods [11], including vibronic couplings if necessary [12], etc. The result is, once again, essentially complete knowledge about the system, at least to the extent that these solutions provide a "good enough" basis for solving the TDSE for any chosen boundary conditions. For systems undergoing chemical reactions — which is, excepting pure redox chemistry, fundamentally a process of nuclear rearrangement — one may further apply the robust machinery of scattering theory [13].

Of course, other options are available to the chemist who wants to study nuclear dynamics. One can use exact Feynman path integral representations of the time-evolution operator, though these are susceptible to the "sign problem" arising from cancellation of the amplitudes associated with distinct paths [14]; study the system using semiclassical theory and the associated initial value representation of the propagator [15, 16]; apply other approximate dynamical schemes, such as ring polymer or centroid molecular dynamics [17–19]; neglect nuclear quantization altogether and proceed classically; or adopt some combination of the preceding methods, with higher-level theory applied to the subsystem where quantum effects are crucial [20]. For sufficiently large systems, many authors neglect the electronic problem as well, instead using parameterized force fields for atoms and molecules in combination with empirical valence bond techniques that allow for creation and destruction of bonds [21].

1.6 Motivation: caveat approximator

The purely classical approach has its attractions, not least in that it reduces the complexity of the problem at hand. Even then, problems relevant to chemistry may be difficult or even intractable to solve, as the extensive machinery developed for classical molecular dynamics simulation (and the continued vitality of classical statistical mechanics) will attest [22, 23]. But there are dangers inherent in making this simplifying choice — in particular, one cannot know a priori whether nuclear quantum effects are going to be important for the accurate description of a given chemical system. There are circumstances for which this judgment is relatively straightforward — any reaction involving proton transfer over a barrier, for example, would be expected to require less energy quantum mechanically than classically, owing to tunneling effects — but it is very difficult (if not impossible) ever to discount quantum effects entirely.

The research compiled in this dissertation is certainly of interest on its own merits. But it also admits consideration of a number of questions: Is nuclear motion important for the system being studied and the properties we wish to investigate? If so, what level of approximation is sufficient to capture the fundamental physics? Is that approximation well-founded and systematically improvable? If so, how much better (and how much more costly) is the next most accurate approximation? And, ultimately, what is the observable experimental signature of the nuclear dynamics? These questions are addressed throughout, sometimes implicitly, at other times explicitly.

1.7 Outline of the present work

Excursions in Chemical Dynamics has been organized as a progression along the conceptual road leading from purely classical nuclear dynamics toward exact quantum mechanics.

Development along these lines is rough, because the subject of each chapter is substantially self-contained. (It is also incomplete, since I have yet to perform any research using exact scattering theory or outside of the Born-Oppenheimer approximation.) We begin in Chapter 2 by omitting nuclear quantization altogether; proceed to incorporate equilibrium (static) nuclear quantum effects, such as rovibrational quantization and discrete spectral transition energies, in Chapter 3; and describe an attempt to derive a pre-existing heuristic method for approximate quantum dynamics in Chapter 4.

1.7.1 Chapter 2

Recent X-ray photoelectron spectra on aqueous hydroxide solutions were seen to exhibit intercoulombic decay (ICD), an off-site Auger decay process. Arguments were made regarding the necessary conditions for ICD to occur — specifically, that it would take place selectively along a hydrogen bond donated by the hydroxide ion. This mechanistic claim ties in with an ongoing controversy over the solvation structure of hydroxide and would constitute decisive evidence for the hypercoordinated model (which allows transient hydrogen bond donation by hydroxide) over the proton-hole model (which does not).

We have performed X-ray absorption calculations using the eXcited electron and Core Hole (XCH) method that indicate that hydrogen-bond donation is not a prerequisite for ICD in this system. Additional calculations suggest that X-ray absorption techniques are also unlikely to be able to distinguish between the two solvation models. In reaching these conclusions, we stress that there are general theoretical criteria for the occurrence of ICD and suggest that they may be used predictively. We further propose that our criteria can be combined with the XCH method to aid in the rational design of a new type of chemo-/radio-therapy protocol for cancer treatment. We are preparing a proof-of-principle experiment along these lines for a model biological solution of bismuth, citrate, and urea.

1.7.2 Chapter 3

The work just described ignored nuclear motion, except to the extent that it is implied by the use of multiple configurations of the hydroxide solution in determining the spectrum. In Chapter 3, we address nuclear motion explicitly. Several models of the X-ray absorption spectrum of nitrogen gas (N_2) are studied in the context of the standard Born-Oppenheimer approximation and XCH. Systematic improvements are made to an initially classical model that includes nuclear motion exactly, beginning with the substitution of the quantum mechanical nuclear density in the bond length R for its classical counterpart, followed by the addition of zero-point energy and other level-shifting effects, and finally the inclusion of explicit rovibrational quantization of both the ground and excited states. The quantization is determined exactly using the Colbert-Miller discrete variable representation (DVR).

It is shown that the spectrum can be predicted semiquantitatively within this simple framework and that it compares respectably well with the prediction obtained using more accurate potentials. With respect to nuclear dynamics, the key lesson is that quantization of nuclear motion is absolutely essential if one wishes to capture fine structure in the spectrum; simpler approaches will, at best, properly reproduce a sharp absorption edge.

Further details regarding the potentials used in Chapter 3 are provided in Appendix A, including fitted and derived potential parameters and convergent parameters for use with the Colbert-Miller DVR. Appendix B consists of a brief discussion of the Voigt lineshape, the relationship between its exact formulation and the approximate one commonly used in the literature, and the implementation of the underlying complex error function in C (including source code).

1.7.3 Chapter 4

Having established the statistical importance of nuclear quantization, we proceed in Chapter 4 to examine a method for the approximate inclusion of true dynamical effects associated with moment-to-moment nuclear motion. Specifically, we study ring polymer molecular dynamics (RPMD), which (though developed recently) has already proven to be a useful theory for the calculation of a wide variety of properties of chemical systems. It is founded, however, on a heuristic extension of the rigorously-derived method of path integral molecular dynamics (PIMD). Here we discuss an effort to *derive* the method by way of judicious approximations to exact expressions for the correlation function and, that failing, by "reverse engineering." These attempts do not succeed, in general, but may eventually provide a means of obtaining the method in the case of a harmonic oscillator, for which it is exact. At the very least, the expressions obtained offer further evidence that RPMD is a reasonable extension of rigorous methods.

1.8 Concluding remarks

Taken together, the work in this dissertation presents an argument by example for the perhaps common-sense propositions that one must be aware of the possible importance of nuclear motion for chemical systems; that one should treat salient nuclear dynamics with as few approximations as feasible in a given application; that one had best proceed with caution when using approximate methods (and test their foundations); and that what at first glance appears to be a negative result can, when viewed from a slightly different perspective, suggest new and fruitful avenues of inquiry. These are general principles, not concrete results (though these latter are not lacking in the text). As such, they constitute the real lessons learned to date in my development as a scientist. Long after the details have faded, these habits of thought will remain.

Chapter 2

Auger decay and the solvation structure of the hydroxide ion

2.1 Introduction[1]

There is currently some controversy over the solvation structure of aqueous hydroxide ion. On the one hand, hydroxide has often been treated as $OH^-(H_2O)_3$, a "water" accepting three hydrogen bonds and with a proton hole in its solvation shell — rather like the water in hydronium [24]. On the other hand, ab initio theory has suggested that hydroxide exists predominantly in a so-called hypercoordinated form, $OH^-(H_2O)_4$, with OH^- accepting four hydrogen bonds from the solvating waters and donating none [24–27]. Hypercoordinated hydroxide can interconvert with a three-coordinate form, and the OH^- transiently *donates* a hydrogen bond of its own in the process. Although a variety of experiments supports the hypercoordinated model (as will be discussed in Section 2.6), there has not yet been conclusive experimental proof for either structure.

Aziz et al. recently performed photoelectron spectroscopy (PES) of $\approx$ 4.0 M hydroxide solutions; sharp features were observed which the authors maintained could only be explained by invoking intercoulombic decay (ICD), an off-site Auger process (see below) [28]. The specific mechanism suggested is that ICD takes place selectively, involving neighboring waters to which the hydroxide ion donates a hydrogen bond. This hydrogen-bond-based selectivity was used to explain why ICD was not observed for an isoelectronic solute, fluoride [28]. A question left unanswered was why the spectrum of neat water would not also exhibit ICD. If this interpretation were correct, however, it would be consistent with the hypercoordinated model alone and would provide dispositive evidence in its favor.

[1]Some of the work discussed here — which in original form was written with Craig Schwartz, David Prendergast, and Richard Saykally — is presently being reviewed for publication in Phys. Rev. Lett.

2.2 Intercoulombic decay: an off-site Auger process

Auger processes involve the decay of a photo-excited electron-hole pair via annihilation of the hole by an electron, with simultaneous emission of another electron from a bound state to the continuum [29, 30]. For photo-excited holes in inner-valence or core-level states, the associated orbitals are well-localized on a given atom, such that Auger spectra are typically dominated by atom-specific transitions. Atomic and molecular phases comprise mainly localized electronic orbitals, and the decay is consequently quite small for processes involving electron emission from any atomic site other than that originally excited. In such systems, this type of "off-site" emission has been termed ICD [31].

It has been observed that an exchange-driven enhancement of the ICD signal can be achieved in weakly-interacting systems by reducing intermolecular distances [32–34]. This effect is a natural consequence of the rate expression for ICD, given here for the dominant case in which the final dication is a singlet [35]:

$$\Gamma_{\mathrm{ICD}} = \pi \sum_{k,\mathrm{ov}_1,\mathrm{ov}_2} \left| V_{\mathrm{ov}_1,\mathrm{ov}_2,\mathrm{iv},k} + V_{\mathrm{ov}_1,\mathrm{ov}_2,k,\mathrm{iv}} \right|^2 \delta(\Delta E_{\mathrm{singlet}}) \tag{2.1}$$

where "iv" denotes the inner-valence orbital φ_{iv} from which the first electron was excited, $\{\mathrm{ov}_1, \mathrm{ov}_2\}$ denote outer valence orbitals, and k denotes the continuum state of the emitted electron. The first and second terms in the square modulus are the direct and exchange Coulomb integrals, respectively, given by

$$V_{ijk\ell} = e^2 \int_0^\infty \mathrm{d}\vec{r}_1 \int_0^\infty \mathrm{d}\vec{r}_2 \, \varphi_i(1)\varphi_k(1)\frac{1}{r_{12}}\varphi_j(2)\varphi_\ell(2) \tag{2.2}$$

In the ICD process, the inner valence and ov_1 orbitals are on one atom (A), while the ov_2 orbital is on a neighboring atom (B). We see, then, that the first term is "direct" in the sense that the initially-excited electron remains on atom A throughout, with transfer of a virtual photon resulting in emission from atom B. The second term involves "exchange" to the extent that there is an electron transfer from the inner valence of A to the outer valence of B, with simultaneous emission of an electron from atom A. The contribution to the rate from this process will therefore be controlled by orbital overlap between A and B, such that reduced intermolecular distances would be expected to enhance it.

Although ICD has been studied primarily in the context of valence excitations [31, 36, 37], recent experiments have shown that core-excited systems may also decay in this fashion, as shown schematically in Figure 2.1 [28]. (The only change in the preceding discussion would then be the replacement of the inner-valence orbital with a core orbital.) Panel A depicts the instantaneous ground-state potential landscape and electron configuration for two atoms separated by some distance. The core electrons have energy substantially lower

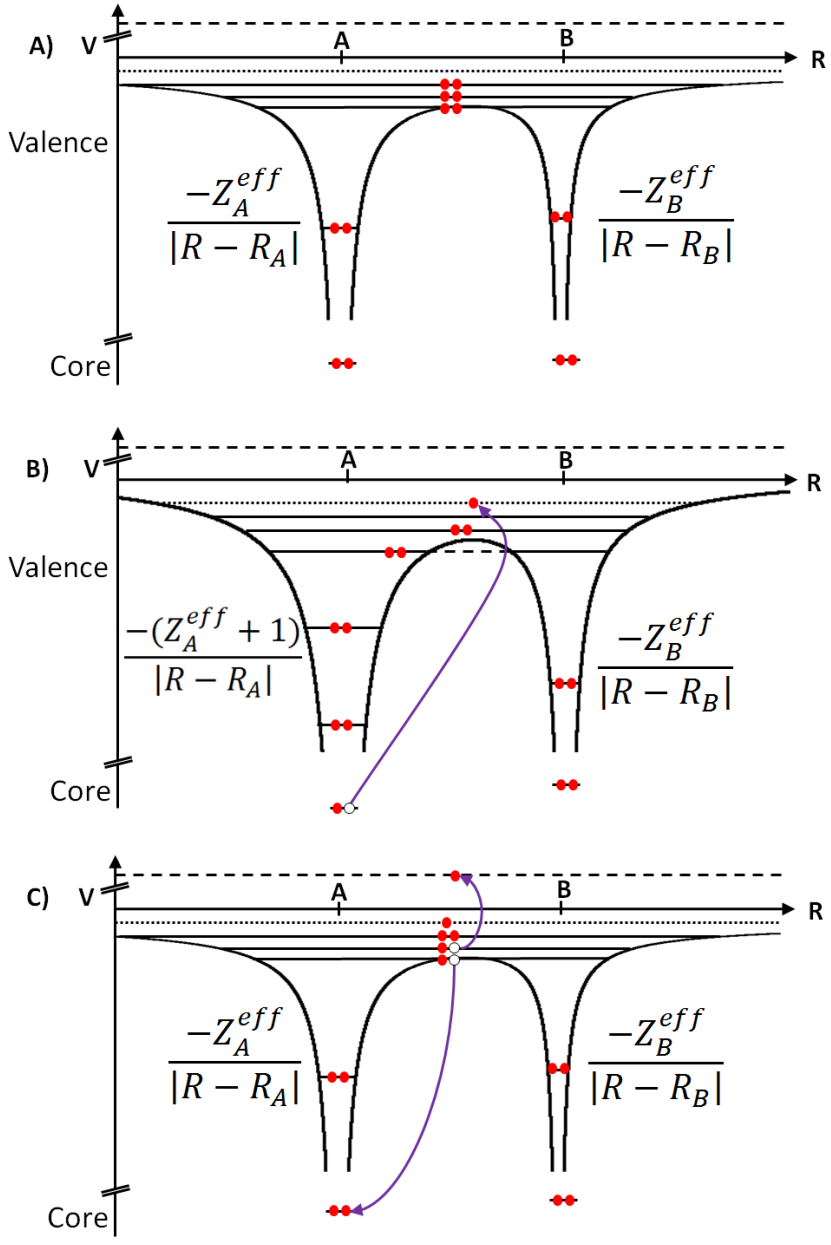

Figure 2.1: A schematic drawing of ICD in a core-excited system. Panel A depicts the effective potential landscape of the valence electrons of two neighboring atomic centers as determined by the number of core-electrons via Gauss's law. In Panel B, the left atom has been core-excited with a concomitant change in its effective valence potential. Certain states which previously were shared between both centers now are localized. In Panel C, the ICD process occurs and the effective potential for the valence electrons returns to its ground state form. See text for more details.

than the valence electrons and are tightly bound to the atomic nucleus, screening the nuclear charge Z such that the valence electrons are subject to an effective nuclear Coulomb potential proportional to $Z^{\text{eff}} = Z - 2$, consistent with Gauss's law. These effective potentials, when added together, give rise to the multiple-Coulomb-well landscape shown in Figure 2.1A, which will support some localized bound states and additional bonding states spanning multiple atomic centers. Core excitation of a given atom (Figure 2.1B) will increment the effective nuclear charge, steepening the local potential landscape at that site. This will cause a sudden downward shift in the energy of some electronic states, which in some cases may prevent coupling with states from neighboring atomic sites, or in others may lead to new electronic hybridization via tunneling through the resulting potential barrier.

The key point for the present work is that the initial excitation process takes place on a timescale of tens of attoseconds, with the subsequent Auger decay taking place on a timescale of a few femtoseconds — long enough for electronic relaxation to occur, but possibly too short a time for significant motion of the nuclei [28]. We choose, therefore, to omit any treatment of nuclear quantization and to treat them as fixed within the context of any given calculation. (This choice was further supported by the fact that propagation of the individual snapshots by a small number of ab initio molecular dynamics steps did not lead to markedly different spectra. We do recognize, however, that the local structure around the hydroxide at the time of each absorption event will differ somewhat. We incorporate these environmental effects, which include nuclear motion indirectly, by studying a subset of the possible configurations.) In the Fermi's golden rule expression for the decay rate, the appropriate initial states will then not correspond to the ground-state picture in panel A, but rather to the core-excited picture in panel B. Once the decay takes place — with a valence electron dropping into the core hole and the excited electron emitted, as shown in panel C — the effective potential seen by the valence electrons is restored to its initial form. Any electrons emitted subsequently will be found at significantly lower experimental energies.

2.3 Computing X-ray absorption spectra via the XCH method

We will now investigate the mechanistic claims of Aziz et al. on a theoretical basis. Specifically, we apply the eXcited electron and Core Hole (XCH) method, which was originally introduced in the context of calculations of the spectra of water and ice [38]. XCH was shown to be more accurate for the purpose than the related full core-hole (FCH) [39] and half core-hole (HCH) methods [40] (which we will address briefly in Subsection 2.3.3). We therefore have some reason to believe that XCH should perform well in its treatment of aqueous solutions.

Our methods have been explained quite lucidly elsewhere [38, 41, 42], but we will cover the main points again here. We calculate the X-ray absorption cross section within the framework of Fermi's golden rule [43]:

$$\sigma(\omega) = 4\pi^2 \alpha_0 \hbar\omega \sum_f |M_{i\to f}|^2 \, \delta(E_f - E_i - \hbar\omega) \tag{2.3}$$

where α_0 is the fine structure constant; $\hbar\omega$ is the energy of the absorbed photon, which must match the transition energy $E_f - E_i$ between the initial and final electronic states; and $M_{i\to f}$ is the associated transition amplitude.

Within the dipole approximation, the transition amplitude is then given by

$$\begin{aligned} M_{i\to f} &= \langle \psi_f | \hat{\epsilon} \cdot \vec{\mathbf{r}} | \psi_i \rangle \\ &\approx S \langle f | \hat{\epsilon} \cdot \vec{r} | i \rangle \end{aligned} \tag{2.4}$$

where $\hat{\epsilon}$ is the direction of polarization of the photon, $\vec{\mathbf{r}}$ is the many-electron position operator, and $\{|\psi_i\rangle, |\psi_f\rangle\}$ are the initial and final many-electron states. The second equality replaces these latter quantities with their single-electron counterparts $\vec{r}$ and $\{|i\rangle, |f\rangle\}$, which yields a result accurate within the factor $S \leq 1$ (approximately constant for all pairs of choices of i and f) [44].

2.3.1 The XCH method

The single-electron eigenstates and energies are calculated self-consistently within the framework of Kohn-Sham density functional theory (DFT) [8, 9] and the Perdew-Burke-Ernzerhof (PBE) generalized gradient approximation (GGA) to the exchange-correlation functional [45,46]. Because there is a continuum of electronic states at high energies, and because linear combinations of atomic orbitals are poorly-suited to describing the delocalized scattering states that appear above the ionization potential, we carry out our calculations in a plane-wave basis (energy cutoff of 85 Ry) using the QUANTUM ESPRESSO code [47]. Plane-wave calculations require periodic boundary conditions, even if one wishes to study an isolated molecule rather than, say, a crystal; we compensate for this by using large supercells that reduce spurious interactions between images of the system. We turn this requirement to our advantage, furthermore, by approximating the electronic continuum with a numerically-converged integration over the Brillouin zone [42, 48].

The initial state $|i\rangle$ is generally chosen to be the $1s$ atomic eigenstate of the core-excited atom, $|1s\rangle$. The final state is approximated by the relaxed, spin-unpolarized ground state of a perturbed system in which the atom is treated using a pseudopotential containing

an explicit core excitation [49]; for oxygen, this corresponds to the electron configuration $1s^1 2s^2 2p^5$. (Higher excited states, if desired, are approximated by the unoccupied Kohn-Sham spectrum.) The resulting valence pseudostate is nodeless around the nuclei, in marked contrast to the atomic core states involved. Transition amplitudes are therefore evaluated using a frozen-core approximation based on an exact transformation between all-electron and pseudo-orbitals [39, 42, 50],

$$\langle f|\hat{\epsilon}\cdot\vec{r}|1s\rangle \approx \sum_{n\ell m}{}' \langle\tilde{f}|\beta_{\ell m}\rangle\langle n\ell m|\hat{\epsilon}\cdot\vec{r}|1s\rangle \tag{2.5}$$

where $\{n,\ell,m\}$ are the hydrogenic quantum numbers, $|\tilde{f}\rangle$ is the valence pseudostate, $\{|\beta_{\ell m}\rangle\}$ are projecting functions properly localized in the atomic core region, and $\{|n\ell m\rangle\}$ are atomic valence states restricted (per the primed sum) to those dipole-allowed and consistent with conservation of angular momentum. In the case of core excitations from the $1s$ orbital, these will be p states.

2.3.2 Aligning XCH spectra

Because the zero of energy in a plane wave calculation is set by the periodic-box-averaged electrostatic potential, XCH spectra will not be referenced to the same zero of energy as any given experiment. We therefore adopt a spectral alignment scheme, as follows [42]: The XCH energy of the former ground-state lowest unoccupied molecular orbital (LUMO) — a bit of a misnomer, since it is now occupied by the excited electron — should approximate the energy at onset. We wish to align our spectra to the ionization potential (IP) as measured by X-ray photoemission, and so we estimate the position of the onset below the IP by the total energy difference between FCH (which omits the excited electron) and XCH. The mapping from our theoretical energy scale to an approximate experimental scale for the i^{th} spectrum is then

$$\begin{aligned} E(i) &\mapsto E(i) + \left[\text{IP} - \left(E^{\text{FCH}}(i) - E^{\text{XCH}}(i)\right) - \epsilon^{\text{XCH}}_{\text{LUMO}}(i)\right] \\ &\mapsto E(i) + \left[\Delta(i) - \epsilon^{\text{XCH}}_{\text{LUMO}}(i)\right] \end{aligned} \tag{2.6}$$

If many XCH spectra are to be aligned in this fashion — for use in determining an ensemble-averaged spectrum, for example — we choose the minimum-energy configuration as a reference state, $i = 0$, and offset the remaining spectra by the transition energy difference

$$\Delta E_r(i) = \left[E^{\text{XCH}}(i) - E^{\text{GS}}(i)\right] - \left[E^{\text{XCH}}(0) - E^{\text{XCH}}(0)\right] \tag{2.7}$$

Note that $\Delta E_r(i)$ reduces to the difference in XCH energy in the case that spectrum i describes the same system as the reference but with the core-excitation taking place on an inequivalent atom.

In general, then, any given spectrum will be aligned to the IP using the mapping

$$E(i) \mapsto E(i) + \left[\Delta(0) + \Delta E_r(i) - \epsilon^{\text{XCH}}_{\text{LUMO}}(i)\right] \tag{2.8}$$

2.3.3 Other methods for X-ray absorption

The HCH method has been used fairly frequently among chemists, and its theoretical foundations go back to the transition potential method of Slater [40, 51]. As the name would imply, only half of an electron is removed from the core. HCH was found to overemphasive the main peak and underestimate the near edge of the water spectrum (as compared to XCH) [38]. The FCH method removes the electron from the system altogether and treats the core-ionized system; it therefore tends to agree with XCH at high transition energies. At the same time, it overestimates the cross section near the onset of the absorption edge and, owing to a sum rule for the integrated intensity [52], underestimates the height of the main peak.

There are, of course, a number of other approaches that have been developed for treatment of the X-ray spectrum. These include full-core treatments using wavefunction theory (which will be addressed in more detail, but with a slightly different focus, in Chapter 3); a multiple-scattering approach, which is inaccurate for light elements [53]; the static exchange method, which incorporates only a fixed interaction between the molecular ion and the excited electron (but accounts for exchange) [54]; a polarization propagator method that obviates a treatment of excited states (but cannot be straightforwardly applied to large systems) [55]; and solution of the relativistic Bethe-Salpeter equation, which (at best) is at least as difficult as solving the Dirac equation [56]. All told, XCH is one of the simplest methods available, and experience has shown it to be acceptably accurate, as well [38, 41, 42, 57].

2.4 XCH calculations for hydroxide and other systems

Condensed phase snapshots of a single hydroxide ion solvated by 31 water molecules were were provided by Prof. Mark Tuckerman; these snapshots were drawn from ab initio molecular dynamics simulations using the BLYP density functional [24]. We analyzed eleven snapshots each of three- and four-coordinate hydroxide in a simulation box of size (9.8615 Å)^3, equivalent to a concentration of ≈ 1.73 M. For the isoelectronic fluoride ion, ten snapshots were generated by classical molecular dynamics using the AMBER force field, with approximately 75 solvating water molecules [21]. In order to generate comparison spectra for neat water, we used six snapshots from a plane-wave simulation of 32 molecules, meaning a total of 192 calculations were performed. All simulations were performed without counterions, and 125 k-points were used for each spectrum. The densities of states calculated include Gaussian broadening of 0.7 eV full width at half-maximum (FWHM).

Although pure versions of the GGA are known to be inferior to hybrid functionals for treatment of the hydroxide radical [58], our success in treating the X-ray absorption spec-

trum (see Section 2.6) indicates that PBE is sufficiently accurate for the purpose. We are also most interested in the relative energies of bands of states, and DFT is known to capture energy differences quite accurately. The calculations in Reference [58], on the other hand, are of structural/dynamical quantities such as the radial distribution function. We are, nevertheless, preparing an additional cross-check in the form of an XCH calculation using a hybrid functional (perhaps B3LYP [59–61], since it is closely related to the self-interaction-corrected hybrid used in Reference [58]); we do not expect our results to change significantly.

2.5 Results and discussion

Figure 2.2 shows the overall valence electronic density of states (DOS) in the photo-excited state of solutions of neat water, fluoride anion in water, and hydroxide within the hypercoordinated model for both three- and four-coordinate hydroxide in water, with the three-coordinate ion donating a hydrogen bond. The total DOS of each solution is plotted together with the corresponding s- and p-type projected densities of states (pDOSs) of the excited species, indicating the energetic overlap of its states with the surrounding solvent. The DOS includes all doubly-occupied orbitals together with the singly-occupied orbitals at the top of the valence band, which sets the zero of energy.

We assume that energetic overlap indicates the possibility of spatial overlap of valence orbitals on the excited species with neighboring water molecules (evidence to follow). The direct term in the ICD rate expression should be roughly equal for hydroxide and water, so the marked differences in their spectra must originate in the exchange term. Because this term is enhanced only when the corresponding decaying valence states overlap in space, we can literally *see* the reason for the lack of ICD in (A) water and (D) fluoride: Our calculations clearly show that the p-type pDOS of the excited molecule does not overlap significantly with the water DOS. In other words, core-excited water and fluoride do not have states capable of significant hybridization with the solvent; in terms of Figure 2.1B, every occupied state is localized in one potential well or the other. Test calculations with a full core hole showed that the presence or absence of the excited electron has little effect on the energy at which we predict ICD occurs.

Hydrogen bond donation does not, therefore, appear to be a necessary condition for ICD; rather, efficient transfer of energy requires spatial overlap of the states of the excited and acceptor species. In this physical picture, core-excited water and fluoride fall into gaps in the electronic density of states of the solvent. In contrast, both (B) three- and (C) four-coordinate hydroxide ions, when core-excited, have some states that overlap in energy (and also spatially, as shown below) with those of neighboring water molecules. Energy can thus be transferred efficiently from the ion to an acceptor water molecule, and ICD will take

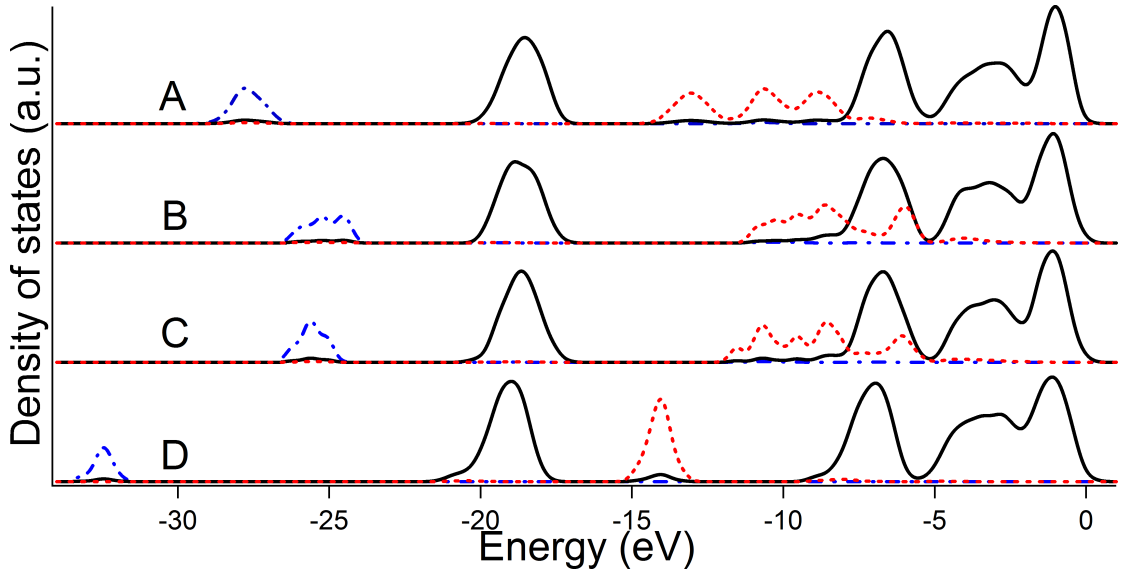

Figure 2.2: The average calculated total DOS (black) of a solution together with the s-type pDOS (dot-dashed blue) and p-type pDOS (dotted red) of core-excited molecules for (A) pure water and (B) three-coordinate hydroxide, (C) four-coordinate hydroxide, and (D) fluoride solutes, averaged over ten snapshots each. Both types of pDOS in (A), (B), and (C) have been scaled to one-third the integrated intensity of the DOS; in (D), the scaling is set to one-sixth. Note that the DOS for the solution does not strongly overlap with the pDOS of the core-excited water or fluoride. Both forms of hydroxide display a feature with strong overlap at approximately -6 eV binding energy, independent of hydrogen bond donation. The features from -8 eV to -17 eV are assigned to the excited species itself, as are the features below -24 eV binding energy.

place.

These findings are summarized in Figure 2.3 for several representative doubly-occupied states. The excited states of the fluoride solution and of neat water are localized on the initial core-excited atoms, whereas both three- and four-coordinate hydroxide states are substantially delocalized into the surrounding solvent. That this delocalization could occur can be seen (in this region of transition energy) as the overlap of the total DOS for the solution and the p-type pDOS of the solute. The overlaps in Panels B and C of Figure 2.2 indicate that the p state of hydroxide is insensitive to hydrogen bond donation; PES must, therefore, be similarly insensitive. This basic insight, coupled with the XCH technique, allows for generally applicable, computationally inexpensive prediction of ICD in condensed phases. Although we do not calculate the PES spectrum explicitly, as has been done in other studies [62], we stress that we have performed accurate simulations of bulk properties of disordered media and sampled over many configurations, which would be infeasible using

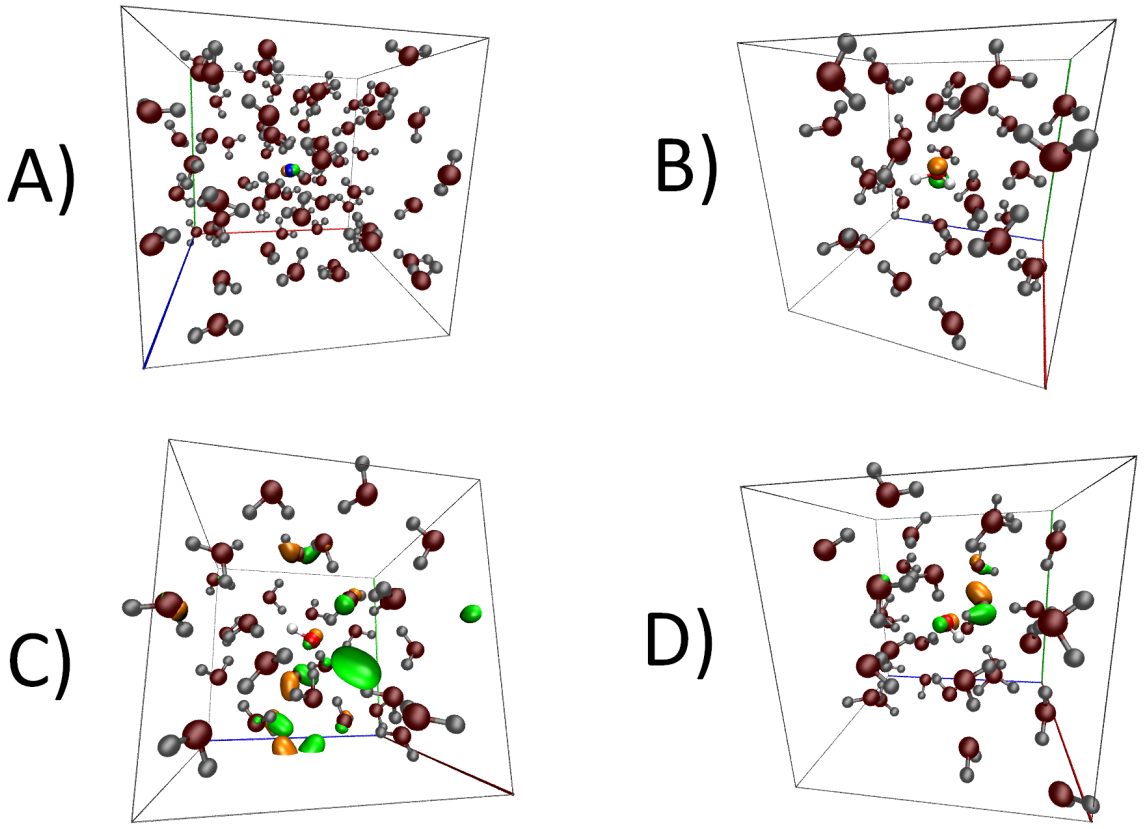

Figure 2.3: 50% density isosurfaces of a single p-state of core-excited (A) fluoride, (B) water, (C) 3-coordinated hydroxide, and (D) 4-coordinated hydroxide. Note the extensive delocalization over neighboring water molecules donating hydrogen bonds in Panels C and D. Similar delocalization is not observed for fluoride or water, as is supported by the pDOS data in Figure 2.2. The states are located at -14, -9, -6, and -6 eV, respectively, as referenced to Figure 2.2.

those more rigorous methods.

Sharp features in the spectra of Aziz et al. were attributable to ICD only because photo-excited hydroxide undergoes ICD largely by way of a single valence state, as indicated by our calculations. That is why sharp peaks were obtained: Transfer will occur primarily in a narrow range of energy (largely within 1 eV of the ≈ -6 eV binding energy). If this band were more diffuse in energy, the resulting PES from ICD would be "blurred out" correspondingly. With that blurring effect in mind, we can use similar arguments to the above to assign previously unexplained peaks in the spectra of materials such as silica to ICD [63,64].

In order for state mixing to occur at all, the core-excited species' valence state(s) must, to some extent, correspond energetically to those of any neighbors. The valence energy will be strongly influenced by the identity of the specific atom excited, principally through the effective nuclear charge. For example, core-excited states of fluoride will typically have valence states shifted lower in energy than those of oxygen, which will be lower than those of nitrogen or carbon. Another factor is local electrostatics: as compared to hydroxide, a water molecule includes an additional Coulomb potential from a second proton, interaction with which will lower the ground-state valence energies. Additional calculations show, for instance, that states associated with core-excited nitrogen in protonated glycine, a simple amino acid, will not mix with water, while those in the deprotonated anionic species permit mixing due to a smaller downward shift in energy [64]. Cytosine also exhibits significant mixing, implying that core-level ICD could be useful in radiooncology, particularly when carbon and nitrogen atoms are excited at their corresponding K-edges, rather than from valence states, as has been discussed previously [36,37]. As in the case of silica, sharp peaks would not be expected in the PES of these systems; the energetic overlap of the valence pDOS with the solvent spans a much broader energy range than in hydroxide.

2.6 Implications for hydroxide solvation

Previous studies in the Saykally group interpreted NEXAFS spectra of hydroxide solutions to support the hypercoordinated solvation model [65]. Figure 2.4 provides a comparison between experimental and theoretical calculations of core-level spectra for water and hydroxide solutions at the oxygen K-edge. The experimental oxygen K-edge data are taken from the literature [65]; the systems studied were pure water and 4.0 M and 6.0 M potassium hydroxide (KOH) solutions. As the hydroxide concentration increases, the intensity changes in the following ways: It grows at low energy ($\approx$ 532 eV) and, to a lesser extent, in the pre-edge ($\approx$ 535 eV). At the same time, the main edge ($\approx$ 538 eV) decreases in intensity, and the post-edge ($\approx$ 542 eV) is essentially unchanged. The experimental spectra are compared with a variety of theoretical calculations: The calculated spectrum of a 1.7 M solution of three-coordinated hydroxide is shown together with the spectral contribution from the hydroxide ion only (magnified for emphasis) and the spectrum of neat water. These spectra are similar to those shown for four-coordinate hydroxide.

In agreement with previous work [65], we can ascribe the low-energy feature before the pre-edge of the liquid to hydroxide. This assignment is supported by comparison with the strong contribution to the absorption solely from the hydroxide ion. Our calculations do not, however, support the contention from the same work that NEXAFS is able to differentiate between three- and four-coordinate hydroxide, for the following reasons: Even in 6.0 M hydroxide solution, there are approximately nine times as many water molecules as

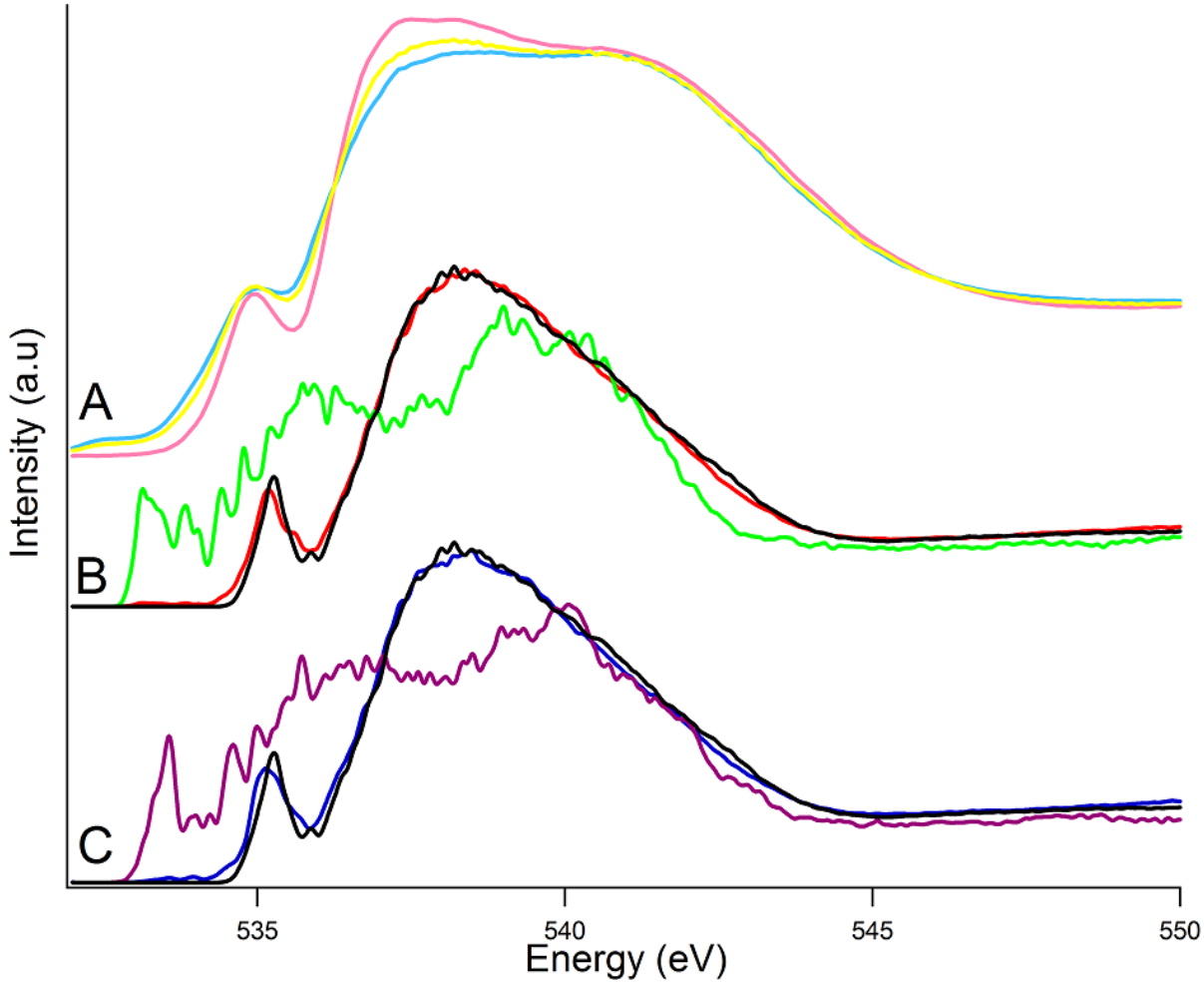

Figure 2.4: Measured and simulated core-level spectra of hydroxide solutions at the oxygen K-edge. Panel A shows the experimental spectra for water (pink), 4.0 M KOH solution (light blue) and 6.0 M KOH solution (yellow) drawn from the literature (see text). Panel B shows the calculated absorption spectrum of a 1.7 M solution of hydroxide when the OH^- is three-coordinated. The overall solution spectrum is shown (red) together with the absorption due solely to hydroxide (green) and to water (black). Panel C shows the calculated absorption spectrum of a 1.7 M solution of hypercoordinated hydroxide. The overall solution spectrum is shown (dark blue) together with the absorption due solely to hydroxide (purple) and to water (black). Simulated spectra were broadened with a 0.2 eV FWHM Gaussian.

hydroxide ions. Based on a spectroscopic sum rule, each oxygen atom must yield an identical integrated intensity [52]. While hydroxide certainly perturbs adjacent water molecules, the effect is not large enough to produce observable differences between three-coordinated and four-coordinated solvation shells. In fact, the main-edge and post-edge features of the $OH^-(H_2O)_4$ and $OH^-(H_2O)_3$ spectra are nearly identical. The pre-edges are more sensitive to the coordination, but not markedly so. And, even if it were possible to isolate the hydroxide spectrum from the background for the solvating waters — which is not currently experimentally possible and would require significant ingenuity, in any case — one would still obtain largely similar spectra for $OH^-(H_2O)_4$ and $OH^-(H2O)_3$.

Having analyzed the relevant X-ray absorption and PES data, we turn our attention to the other data available regarding the solvation structure of hydroxide. At time of writing, the most convincing piece of evidence against the proton-hole model remains the fact that it predicts the diffusion constant to be six times larger than its experimental value [27]. This result is fairly robust to higher-order corrections, such as those from tunneling effects. But there are a variety of other sources of evidence.

There have been numerous neutron- and X-ray scattering studies of hydroxide solutions [66–70]. The data indicate a gradual evolution from four- to three-coordinate hydration as the concentration of hydroxide is increased from 2.0 M to near the solubility limit (> 12.0 M). This observation is consistent with common-sense expectations: There are fewer waters per hydroxide in the solution as the concentration increases, and thus the average coordination of hydroxide must decrease. One weakness in the scattering data is that they are overfitted, which is exacerbated when the molecule of interest does not contrast markedly in its scattering properties from the background solvent. In this case, hydroxide scatters similarly to water. It has also been shown recently that the scattering data for neat water are consistent with a structure containing anywhere from 2.0 to 3.5 hydrogen-bonded neighbors [71]. It is thus difficult to make a strong conclusion as to hydroxide solvation structure.

Fourier-transform infrared attenuated total reflection spectra have been reported for dilute HDO in D_2O [72, 73]. In these experiments, a careful subtraction scheme was used to isolate the spectral contribution due to hydroxide. It was determined that the resulting spectra could only be replicated computationally if hydroxide donates a hydrogen bond. The model used, however, involved calculating the IR spectra of several small aqueous clusters of hydroxide (containing fewer than eight water molecules). To the extent that the bulk liquid is unlikely to be modeled successfully by optimized cluster structures, the specific origins of any given spectral feature will be ambiguous; for neat water, 32 water molecules were necessary for convergence [74]. It has further been shown that assigning spectral features of a bulk liquid to individual stretches is difficult at best [75]. The most clear-cut means of interpreting the spectrum of aqueous hydroxide may be to simulate both solvation models atomistically and to draw conclusions based on analysis of the resulting

trajectory data [76].

Recent evidence favoring a hypercoordinated model of hydroxide has also been obtained from two-dimensional infrared spectroscopy [77]. While there is adequate agreement between theory and experiment, a large fraction of the signal arises from the surrounding bulk water. Furthermore, only a relatively small spectral window was probed.

2.7 Concluding remarks and future work

Our contribution to the ongoing discussion regarding hydroxide solvation is to emphasize that X-ray photoelectron spectroscopy is incapable of distinguishing the hypercoordinated and proton-hole models of hydroxide solvation, at least insofar as any such distinction would be predicated on hydrogen-bond-selective ICD. We also note that the hydroxide signal in NEXAFS will be weak compared to that of the surrounding solution, owing to a sum rule that requires each oxygen to contribute an equal integrated intensity to the PES spectrum [52]. More sensitive methods will be required for an unambiguous determination of the solvation structure of hydroxide.

We are in the happy position, however, of having arrived at more than a pair of negative results. Our findings suggest a diagnostic criterion for the possibility of enhanced ICD between core-excited molecules and their neighbors — overlap between their densities of states — while the XCH method provides a convenient route toward computing these DOSs and, thus, making theoretical predictions. Preliminary calculations suggest, for example, that core-excited bismuth in aqueous solution with citrate and urea will selectively transfer energy to the citrate via ICD [64]. Because theoretical ICD rates are known to vary over many orders of magnitude, depending on the expression used [35] — and, therefore, we cannot know a priori whether the predicted enhancement will be reflected in a significant excess of damaged or destroyed citrate over reasonable experimental timescales — we are arranging to perform just such an experiment at the Advanced Photon Source of Argonne National Laboratory.

If our prediction is borne out, this work could be seen as a major breakthrough in the fundamentals of radiooncology. Present-day X-ray therapies are commonly based around exposure to high-energy (megaelectronvolt) rays that provide a continuous and reliable transfer of energy [78, 79]; there is generally little targeting, except to the extent that the patient's body can be reoriented with respect to the beam. Brachytherapy (surgical insertion of radioactive "seeds" into cancerous tissue) and therapy with hadron beams (which exhibit a tunable Bragg peak in penetration depth), by contrast, are fundamentally localized treatments [78]. The most advanced X-ray therapies now in use — three-dimensional conformal radiotherapy and its direct successor, intensity-modulated radiotherapy — do

allow for localization of the radiation to the region of the tumor (as do similar hadron beam techniques) [80]. They require, however, that many computed tomography scans be compiled into a three-dimensional image of the affected region, which information is used to design the treatment field; these preliminary scans deliver a large amount of unlocalized radiation (equivalent to over a hundred standard chest X-rays, or an order of magnitude more than a year's background exposure) [81].

The state-mixing criterion established here would allow for rational design of a new kind of targeted chemical/X-ray treatment protocol: A heavy metal would be administered in the form of a complex with a small molecule that is selectively taken up by the cancerous tissue. This approach has precedent in radioisotope therapy, such as the use of hormone-complexed lutetium-177 in treatment of endocrine tumors [82]. (It would also be possible, depending on the toxicity of the metal in question and its salts, to administer it directly by injection of a solution, whether subcutaneously, intramuscularly, or into an organ or bone. Any of these scenarios would allow for coarse, short-term localization of the X-ray substrate to the direct vicinity of the tumor.) Core excitations in heavy metals occur at characteristic wavelengths, such that irradiation of the tissue with a tuned X-ray source would help to further localize the radiation dose and energy transfer, thereby increasing damage to the cancer [83–86]. There would be a concomitant reduction in damage to healthy tissue, owing to its transparency to the greater portion of the secondary electrons emitted [78]. And because the DOS of the excited complex will depend sensitively on the nature of the core excitation and the valence electronic structure of the complexed molecule, one could potentially select for energy transfer to specific targets (such as DNA or other critical cell structures). The ability to build *molecular* localization of the radiation dose into the treatment is the most novel element of our proposal.

Chapter 3

Nuclear quantum effects in the structure of the N_2 NEXAFS spectrum

3.1 Introduction[1]

Throughout the previous chapter, nuclei were treated as frozen in some predetermined configuration. Such a treatment is much more the rule than the exception in theoretical calculations of X-ray spectra; the configuration chosen is generally the global minimum on the potential energy surface, as determined by electronic structure calculation. When there are geometrically-distinct, isolable conformers of a given molecule — or, as was seen in the case of aqueous solutions, when environmental effects may be important — additional configurations may be used as well. But there is a growing recognition, based on theoretical efforts toward reproducing experimental spectra, that one must account for the effects of nuclear motion, at least in a statistical sense; after all, even classical nuclei will explore the Born-Oppenheimer potential energy surface at finite temperature. Indeed, there is evidence to suggest that vibrations of even very heavy atoms, such as the aluminum in corundum (α-Al_2O_3) and the titanium in rutile (TiO_2) [87, 88], can have a measurable effect in the structure of X-ray spectra.

Prior to the present study, spectra obtained using XCH have incorporated nuclear motion by averaging over configurations sampled from either classical molecular dynamics or from path integral molecular dynamics (PIMD; see Chapter 4 or Reference [89] for more details) [41, 42]. One of the more striking successes of this approach is in capturing the

[1]Much of the material in this chapter has been reprinted, with permission, from S. Fatehi, C. P. Schwartz, R. J. Saykally, and D. Prendergast, J. Chem. Phys. **132**, 094302 (2010) [57]. Copyright 2010, American Institute of Physics.

shoulder in the spectrum of *sym*-triazine — it is dark until classically-accessible configurations are sampled, and it remains within statistical error bars until PIMD is used [42]. Here we will take these insights to their logical conclusion for a venerable model system [90], nitrogen gas (N_2), by accounting exactly for nuclear vibrational and rotational quantization and including the effect of nuclear spin statistics. We will further examine the effect of finite temperature on the spectrum.

In calculating gas-phase NEXAFS spectra, a discrete set of transition energies and associated intensities is generated; this "stick spectrum" can then be broadened to match experiment. Broadening is attributed to a combination of lifetime effects — energetic smearing of the molecular states due to the energy-time uncertainty principle — and experimental sources such as finite monochromator width, pressure broadening, and Doppler broadening [52]. There appears to be no consensus in the literature as to how much broadening to apply to a spectrum once calculated, though common sense suggests that the lifetime broadening be determined either on the basis of additional theory or from an experimental measurement. Fitting of the nitrogen spectrum to a Voigt lineshape — a convolution of the Lorentzian and Gaussian profiles associated with lifetime and instrument broadening (see Appendix B) — has determined there to be approximately 110–130 meV FWHM (full width at half-maximum) Lorentzian broadening, with an experiment-dependent amount of Gaussian broadening; a short review of the literature in this regard is provided in Reference [91]. This range of values is corroborated, for example, by semiempirical electronic structure methods, which predict the N_2 Auger lifetime to be 120 meV [92]. Fitting to a recent high-resolution experiment led to an estimate of the lifetime broadening of 115 meV [93]; we will use this value as our baseline.

Because our treatment of nuclear quantization is exact, we will make an independent estimate of the lifetime by adjusting our broadening to better match the experiment. In reaching that point, we will examine a hierarchy of treatments of nuclear motion and their associated model spectroscopies, starting with purely classical nuclear motion and classical transitions between the ground and excited-state potential-energy curves and ending with an exact treatment (within the Born-Oppenheimer and Franck-Condon approximations) of transitions between rovibrational states on the quantized electronic curves.

There is a substantial body of work regarding the calculation of Franck-Condon factors for small molecules undergoing NEXAFS excitation [94–105], though none of these studies has accounted for rotations. The most common approach has been to calculate the minimum ground state energy, the equilibrium energy and position of the excited state, and the associated Hessians (since it is assumed that excited-state motion is characterized by the vibrational normal modes). A linear-coupling approximation is then made, and the Franck-Condon factors may be calculated explicitly, modeled phenomenologically, or assumed to adhere to a Poisson distribution. Previous studies indicate that this choice yields

only minor differences in the results [98].

The molecules studied by the cited authors — such as formaldehyde [97, 98], acetic acid [104], and acrylonitrile [105] — are relatively complex compared to N_2 and, therefore, represent a greater technical challenge for prediction of the spectrum. At the same time, because of the large number of modes present in these systems, there is typically less detailed structure in the spectrum over a given range of energy. Even so, and in spite of the comparative rigor of such treatments, the spectra are captured semiquantitatively, with obvious disparities (in both peak location and height) in those regions of the spectrum where fine structure is most prominent. (Agreement with less-detailed spectral features is, in any case, more difficult to judge.) We will see that it is possible to predict the spectrum comparably well with respect to these fine spectral details using the XCH approach, albeit for a far simpler system. The nitrogen molecule should, in fact, make for a more stringent test along these lines, as its entire first X-ray transition can be construed as consisting of "fine structure."

3.2 Density functional theory calculations

For the purposes of computing transition amplitudes and the excited-state energy, we applied the XCH method (as described previously). To reduce spurious interactions between nitrogen images, large box sizes of $(15\ \text{Å})^3$ were used. The energies thus obtained were aligned using the energy at the minimum as a reference; alignment to the ionization potential was not performed here, since we ultimately shift the location of the first peak in the spectrum to match experiment.

The initial state (before excitation at the nitrogen K-edge) was fixed to the $1s$ atomic eigenstate of nitrogen; the corresponding molecular state is the ground state, $X^1\Sigma_g^+$. After excitation, the electron configuration of the core-excited atom is chosen to be $1s^1 2s^2 2p^4$; when incorporated into the N_2 molecule, this configuration corresponds to a degenerate pair of dipole-active molecular excited states with term symbol $^1\Pi_u$ (as well as a spin-forbidden state with term symbol $^3\Sigma_u^-$). The lowest-energy core-excited state is the only one relevant for the first transition in the N_2 NEXAFS spectrum, which may be characterized as $1s \rightarrow$ LUMO [93].

3.3 Model spectroscopies for three classes of transition

Over 800 nitrogen transitions were calculated at separation distances sampled from a path integral molecular dynamics simulation (for more on which, see Chapter 4 and Reference

[89]), with special attention paid to configurations lying in the ground-state potential well. Variations in the transition probability were monitored and observed to remain within 1% of the value at equilibrium separation. This result indicates that the transition dipole moment is insensitive to the internuclear spacing as well, and, therefore, Herzberg-Teller effects may be neglected; any errors thus introduced would not be of leading order, in any case (as explained in Subsection 3.3.3). Having established that we are safely within the Franck-Condon regime, we must take a moment to discuss the spectral models that we will use at each level of our treatment.

3.3.1 Models for classical-to-classical transitions

Figure 3.1 depicts schematically the types of transition considered. Panel A represents a vertical excitation at bond length R from the bottom of the ground state potential $V_g(R)$ to the bottom of the excited state potential $V_x(R)$. This type of transition may be termed "classical," in the sense that we treat all such excitations as allowed with equal (unit) probability; the structure of a spectrum based on these transitions is determined by the (canonical) classical radial density of the ground state. ("Density" and "radial density" will be used throughout this chapter and will always denote the nuclear radial probability distribution.) We treat the spectrum as a set of intensities continuous in the transition energy and determined solely by the relation

$$I(E;\beta) \propto \int_0^\infty \mathrm{d}R\, \rho_{\mathrm{CL}}(R;\beta)\delta\left(E - \Delta E_{\mathrm{CL}}\right) \tag{3.1}$$

where $\Delta E_{\mathrm{CL}}(R) = V_x(R) - V_g(R)$ is the transition energy, $\rho_{\mathrm{CL}}(R;\beta) = \frac{1}{Q}e^{-\beta V_g(R)}$ is the radial density with associated canonical partition function $Q = \int \mathrm{d}R\, e^{-\beta V_g(R)}$, and the semicolon indicates that the temperature dependence (included through the inverse thermal energy $\beta = \frac{1}{k_B T}$) enters only parametrically.

In previous work [42], another model has been used that incorporates the quantum mechanical density (as described in the next subsection) but leaves the transition energy in classical form:

$$I(E;\beta) \propto \int_0^\infty \mathrm{d}R\, \rho(R;\beta)\delta\left(E - \Delta E_{\mathrm{CL}}\right) \tag{3.2}$$

Although this model is inconsistent from a physical point of view, so too is any mixture of quantum and classical energetics. We address it here for the sake of underlining the relation between our work and its antecedents, and also because it is readily calculable even for large systems and, therefore, of pragmatic interest.

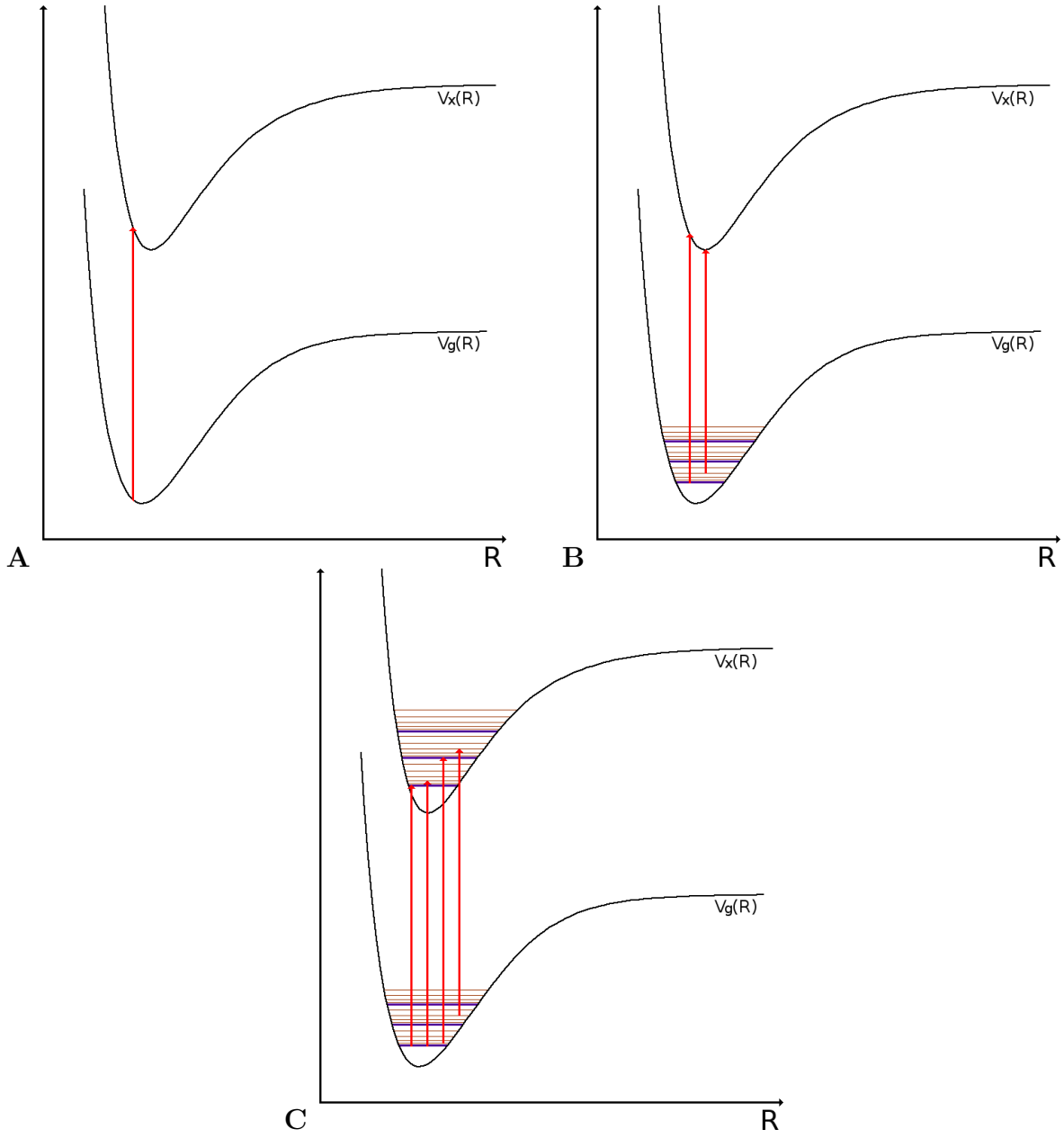

Figure 3.1: A schematic depiction of the three classes of transitions associated with our spectral models. Panel A shows one possible purely classical transition; Panel B shows two possible transitions from a quantized ground to a classical excited state; and Panel C shows four possible transitions from a quantized ground state to a quantized excited state. Transitions are shown as red arrows; the classical energies follow the black Born-Oppenheimer potential curves; and vibrational and rotational states are shown in dark blue and brown, respectively. See Subsection 3.3.1 for details.

3.3.2 Models for quantum-to-classical transitions

The second class of transition, depicted in Panel B of Figure 3.1, is distinguished from the first by (vibrational or rovibrational) quantization of the ground state; here the transition is from a state $|vJ\rangle$ on the ground state potential energy curve to a classical excited state. ($\Delta E(R)$ for this type of excitation will therefore be smaller than for the analogous classical transition, if R is in the classically-allowed region; in the classically-forbidden region, where $V_g(R) > E_{vJ}$, $\Delta E(R)$ will be larger.)

This scheme can be understood to imply two very different spectral models. In the first model, which corresponds to the convergent (infinite-bead) limit of PIMD, transitions occur according to the fully-averaged density $\rho(R;\beta)$, but with the same averaged energy $\langle E_{vJ}\rangle$ everywhere in R. Because the excited state remains classical, all such transitions are still allowed, and our model for the spectrum remains formally the same:

$$I(E;\beta) \propto \int_0^\infty \mathrm{d}R\, \rho(R;\beta)\delta\left(E - \Delta E(R)\right) \tag{3.3}$$

The density is now quantum mechanical: $\rho(R;\beta) = \frac{1}{Z}\sum_{vJ} g_N(J)e^{-\beta E_{vJ}}|\psi_{vJ}(R)|^2$, where $\psi_{vJ}(R)$ is the radial wavefunction for state $|vJ\rangle$, $Z = \sum_{vJ} g_N(J)e^{-\beta E_{vJ}}$ is the quantum canonical partition function, $g_N(J)$ is the rotational degeneracy (which we will address in more detail directly below), and the transition energy depends on the thermal average of the quantized energies, $\langle E_{vJ}\rangle = \frac{1}{Z}\sum_{vJ} g_N(J)e^{-\beta E_{vJ}}E_{vJ}$, as $\Delta E(R) = V_x(R) - \langle E_{vJ}\rangle$.

The rotational degeneracy $g_N(J)$ is distinguished from the usual degeneracy factor $g(J) = 2J + 1$ in that it also accounts for the nuclear spin statistics of the N_2 molecule: The ^{14}N nucleus is a boson with spin $I = 1$, and as a result the total wavefunction must be symmetric with respect to exchange of the nuclei. To impose this condition is equivalent to requiring that antisymmetric nuclear spin states be paired with symmetric (even J) rotational states — and vice versa for symmetric nuclear spin states and antisymmetric (odd J) rotational states [106]. There are a total of 9 symmetrized combinations of the two nuclear spins, leading to a 2 : 1 ratio of symmetric to antisymmetric spin states. Thus, for every three molecules of N_2, two will be *ortho*nitrogen (supporting only even J) and one will be *para*nitrogen (supporting only odd J). The combined rotational/nuclear-spin degeneracy must then be

$$g_N(J) = \left\{ \begin{array}{ll} 2(2J+1), & J \text{ even} \\ \\ 2J+1, & J \text{ odd} \end{array} \right\} \tag{3.4}$$

With that slight change in the usual scheme of things established, we return to the second model spectroscopy for mixed transitions, which model is more physical in conception: We picture an ensemble of N_2 molecules, each of which is in a *specific* state $|vJ\rangle$ (with associated

energy E_{vJ}) and can make transitions consistent with the state density $\rho_{vJ}(R) = |\psi_{vJ}(R)|^2$. For each member of the ensemble, we therefore have

$$I_{vJ}(E) \propto \int_0^\infty \mathrm{d}R\, \rho_{vJ}(R)\delta\left(E - \Delta E_{vJ}(R)\right) \tag{3.5}$$

where $\Delta E_{vJ}(R) = V_x(R) - E_{vJ}$. Since the ground rovibrational states will be populated per the Boltzmann distribution, the predicted spectrum is the thermal average

$$I(E;\beta) \propto \frac{1}{Z}\sum_{vJ} g_N(J) e^{-\beta E_{vJ}} I_{vJ}(E) \tag{3.6}$$

These mixed quantum-classical spectral models are certainly similar — in the 0 K limit, in fact, they will give the same spectrum — but they are not identical, as we will see.

3.3.3 The Franck-Condon principle and the Herzberg-Teller effect

Once we have quantized nuclear motion on both the ground- and excited-state surfaces, we are in safer territory, physically and theoretically speaking. Within the Born-Oppenheimer approximation, the dipole transition amplitudes may be written as

$$M_{ivJ\to fv'J'}(R) = \langle v'J'|\langle f|\hat{\mu}(r;R)|i\rangle|vJ\rangle = \langle v'J'|\mu_{i\to f}(R)|vJ\rangle \tag{3.7}$$

where i and f label the initial and final electronic states, v and v' label vibrational states, J and J' label rotational states, and $\mu(r;R)$ is the total electric dipole moment operator (which is understood to depend on the nuclear coordinate R only parametrically). The second equality defines the electronic transition dipole moment for a given choice of nuclear separation.

If we expand the transition dipole moment around R_0 — the global minimum of the potential energy surface, say — we obtain

$$M_{ivJ\to fv'J'}(R) \approx \langle v'J'|\mu_{i\to f}(r;R_0) + \left.\frac{\partial \mu_{i\to f}}{\partial R}\right|_{R=R_0}(R-R_0) + \ldots|vJ\rangle \tag{3.8}$$

such that truncating the expansion and collecting terms yields

$$M_{ivJ\to fv'J'}(R) \approx \mu_{i\to f}(r;R_0)\langle v'J'|vJ\rangle + \left.\frac{\partial \mu_{i\to f}}{\partial R}\right|_{R=R_0}\langle v'J'|(R-R_0)|vJ\rangle \tag{3.9}$$

The first term in Equation 3.9 is a statement of the Franck-Condon principle, namely, that transitions from $|i\rangle$ to $|f\rangle$ originating in the neighborhood of R_0 will have amplitude directly proportional to the rovibrational overlap integral $\langle v'J'|vJ\rangle$. If the transition dipole

moment is constant (or nearly so), the Franck-Condon principle holds; when the transition dipole moment varies appreciably in the region around R_0, however, the second term will be non-negligible, and the transition amplitudes will exhibit the so-called Herzberg-Teller effect [106, 107]. Since we have already established that XCH transition amplitudes for nitrogen do not vary significantly in the potential well, vibrational overlaps will determine our transition intensities through their square moduli, the Franck-Condon factors [108]; the specific value of the transition dipole moment will be subsumed into and superceded by scaling of an overall constant to match the intensity of the experiment (given in arbitrary units).

3.3.4 The Franck-Condon model for fully quantum transitions

The third class of transition, shown in Panel C of Figure 3.1, is simply that of Franck-Condon transitions between (ro)vibrational states on the ground potential energy curve and (ro)vibrational states on the excited state potential energy curve. The probability of transition at given R is no longer uniform, and the density is therefore an inappropriate quantity for use in determining the spectrum. We instead model the spectrum as deriving from all symmetry-allowed ground-to-excited-state transitions $|vJ\rangle \rightarrow |v'J'\rangle$.

We assume that both the ground and excited state fall under Hund's case (a) for coupling between the spin and orbital angular momenta, which consists of weak coupling of electronic and nuclear motions and strong coupling of the spin and orbital motion to the internuclear axis [106]. The ground state $X^1\Sigma_g^+$ has angular momentum around the internuclear axis $\Omega = |\Lambda + \Sigma| = 0$, where Λ is the maximum projection of the orbital angular momentum (corresponding to the Greek letter in the term symbol for the state) and Σ is the appropriate projection of the spin angular momentum. The excited state $^1\Pi_u$ has $\Omega = 1$, fulfilling the $\Delta\Omega = 0, \pm 1$ selection rule for the electronic transition; further, all rotational transitions with $\Delta J = 0, \pm 1$ are allowed. (This latter rule always holds, of course, but the $\Delta J = 0$ case is forbidden for $\Delta\Omega = 0$.) Note also that, since J is bounded from below by Ω, there is *no* $J = 0$ rotational state on the excited electronic surface [106].

These transitions are treated as occurring in proportions set by the relative thermal population of the state $|vJ\rangle$ with respect to the ground state $|00\rangle$, i.e., with probability $P_{vJ}(\beta) = \frac{1}{Z} g_N(J) e^{-\beta \Delta E_{v0J0}}$, where $\Delta E_{v'vJ'J} = E_{v'J'} - E_{vJ}$. These considerations yield the standard spectral model

$$I(\Delta E; \beta) \propto \sum_{v'vJ'J} \int_{-\infty}^{\infty} \mathrm{d}\Delta E \, \delta(\Delta E - \Delta E_{v'vJ'J}) \delta(|J' - J| \leq 1) \left|\langle v'J'|vJ\rangle\right|^2 P_{vJ}(\beta) \quad (3.10)$$

where the first Dirac delta restricts ΔE to those values supported by the ground and excited state energies, the second Dirac delta enforces the rotational selection rule, and

$\langle v'J'|vJ\rangle = \int \mathrm{d}R\, \phi^*_{v'J'}(R)\psi_{vJ}(R)$ is the vibrational overlap for the transition. Hereafter, v' and J' will be used to refer to quantum numbers for states on the excited potential energy curve and v and J to those for states on the ground potential energy curve.

3.4 Computing the spectra

3.4.1 The ground- and excited-state potentials and fits

Our initial calculations of the nitrogen X-ray absorptions were for values of R centered in the ground-state potential well; owing to the small (≈ 0.05 Å) displacement of its minimum, the same was true for the excited-state potential. In order to capture nuclear quantum effects, however, the geometry of the potential away from the minimum may be important; for example, anharmonicity at larger values of R will affect the nuclear vibrational frequencies.

We avoided sampling the electronic structure energies on an infeasibly dense grid in the radial coordinate by adding a small number of points at an even spacing of 0.1 Å. These points span the entire range of physically-relevant bond separations, from well into the repulsive barrier region (0.1 Å) to near the dissociation threshold (4.7 Å for the ground state and 3.4 Å for the excited state). The complete sets of points were then used to develop a 14-Gaussian fitting function of form $V(R) = \sum_i a_i e^{-(\frac{R-c_i}{b_i})^2} + V_e$ for each curve, where V_e is the energy at well minimum and $\{a_i, b_i, c_i\}$ are the fit parameters. (Refer to Appendix A for more details.)

The resulting ground- and excited-state potential fits are shown in Figures 3.2 and 3.3, respectively; they are paired for the purpose of comparison with potentials obtained by fitting to experimental data (see [109, 110] and also Appendix A). Although our potential fits are in good agreement with the empirical curves in the well region, the dissociation energies are several electronvolts too large, indicating the over-binding commonly observed in DFT [111]. The multi-Gaussian functional form does not allow for reliable prediction of the electronic energy outside of the fitting regions, but this is not an important failing; the states of interest to us here are deep within the well, at energies no higher than 0.435 eV for the ground and 404 eV for the excited state (vide infra for discussion of the physical relevance of these energies).

3.4.2 The classical density

The classical radial density for the (rotationless) ground state at 300 K was determined analytically. It is very nearly Gaussian, with slight enhancement for values of R greater than the most-probable bond separation and slight diminishment for smaller values of R.

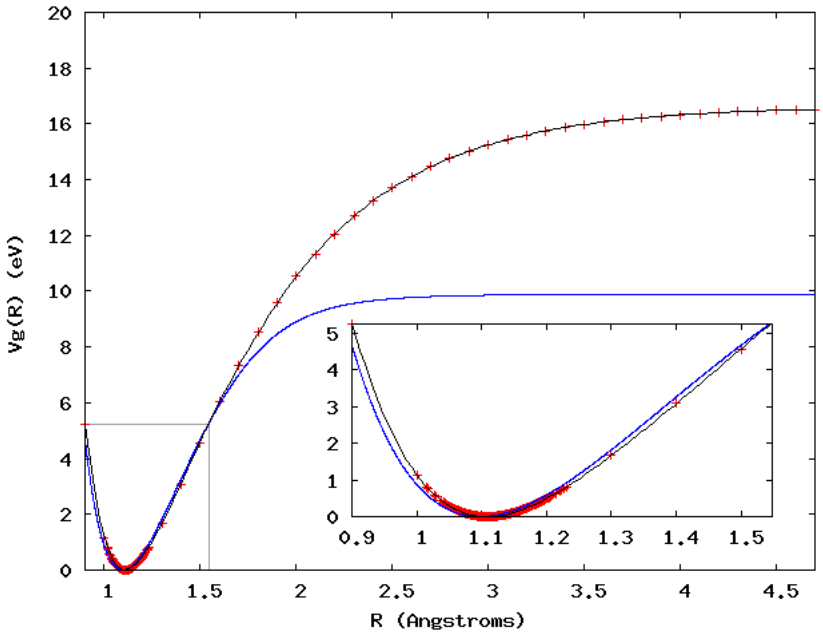

Figure 3.2: The electronic structure energies for the ground state in electronvolts (red points) plotted with the 14-Gaussian fit (black) to the full region depicted. The inset between 0.9 and 1.6 Å shows the quality of the fit for the bottom of the ground-state well; rovibrational state $|0, 34\rangle$ is deep within the well (0.435 eV). The blue curve at lower dissociation energy is the empirical MLR_4(6,8) potential (see text for details).

The reason for the uneven distortion with respect to a Gaussian is simply that the shape of the potential allows for more frequent visits to the large-R region than to the small-R region at 300 K. To determine the classical canonical density at 0 K is trivial; the particle is at a standstill, sitting at the bottom of the potential well. As such, the density is a delta function centered at the ground state equilibrium position.

3.4.3 The Colbert-Miller discrete variable representation

The Colbert-Miller (sinc-function) discrete variable representation (DVR) was used to compute the quantum densities; because the energies and wavefunctions thus obtained are crucial to our results, we briefly review it here [112]:

We begin by forming a grid representation of the nuclear Hamiltonian of the system, $\hat{H} = \frac{\hat{p}^2}{2\mu} + V(\hat{R})$, with μ the reduced mass. In this case, the grid falls in the coordinate range $(0, \infty)$. Because the potential $V(\hat{R})$ is a function only of the position operator, its matrix representation in the basis of grid points $\{R_i\}$ is trivial, $\mathbf{V}_{ij} = \delta_{ij} V(R_i)$, and

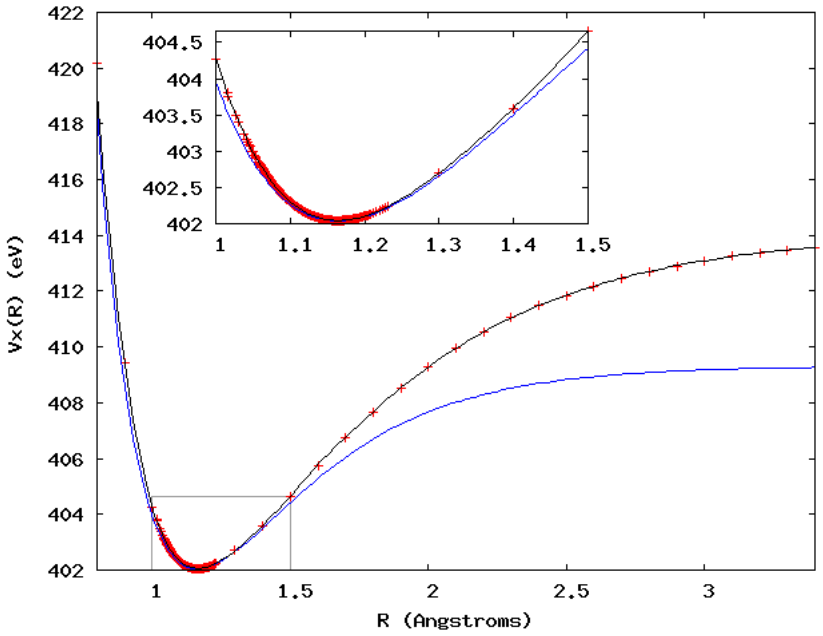

Figure 3.3: The electronic structure energies for the excited state in electronvolts (red points) plotted with the 14-Gaussian fit (black) to the full region depicted. The inset between 1 and 1.5 Å shows the quality of the fit for the bottom of the excited-state well; rovibrational state $|6, 34\rangle$ lies at an energy of 403.8 eV. The blue curve at lower dissociation energy is an empirically-parametrized Morse potential (see text for details).

the challenge lies in determining the representation of the kinetic energy operator. Colbert and Miller show that there is a specific representation that is independent of any choice of basis functions for the grid,

$$\mathbf{T}_{ij} = \frac{\hbar^2}{2m\Delta R^2} \left\{ \begin{array}{ll} [\frac{\pi^2}{3} - \frac{1}{2i^2}], & i = j \\ (-1)^{i-j}[\frac{2}{(i-j)^2} - \frac{2}{(i+j)^2}], & i \neq j \end{array} \right\} \tag{3.11}$$

where ΔR is the grid spacing and $R_i = i\Delta R$ for $i \in \{1, \ldots, \infty\}$. They also show that the wavefunction associated with each grid point may be written as

$$\langle R|R_i\rangle = \frac{\sin[\frac{\pi(R-R_i)}{\Delta R}]}{\pi(R - R_i)} \tag{3.12}$$

Consequently, the eigenvectors obtained from the diagonalization of the Hamiltonian matrix $\mathbf{H} = \mathbf{T} + \mathbf{V}$ may be expressed as a linear combination of the grid wavefunctions, $|\psi_j\rangle = \sum_i c_{ji}|R_i\rangle$, that is smooth and evaluable for all R, in close correspondence with the

analytical theory.

Three parameters were varied in bringing the calculations to convergence: the grid spacing ΔR, the maximum grid value of the position $R_{\max} = i_{\max}\Delta R$ (with $i_{\max}$ also setting the number of approximate eigenvalues and eigenvectors obtained), and a cut-off energy V_c. The latter allows for a simple form of adaptive grid, in which no grid points are placed where $V(R_i) > V_c$. For detailed discussion of the convergent parameters, please refer to Appendix A.

The parameters used determine grids of 213 and 203 grid points for the rotationless ground and excited states respectively; only a few points are lost to the cut-off as J increases. Our ground-state calculations were validated by comparison of the DVR energies to those given by an empirical Dunham expansion due to Le Roy et al. [110]; they were found to be in excellent — although, as expected, not exact — agreement.

3.4.4 The quantum densities

Once the DVR for the ground state was converged, obtaining the canonical density was a simple matter. A single DVR calculation accounts for contributions to the density from all $|vJ\rangle$, with J fixed and included as part of an additional centrifugal potential $\frac{\hbar^2 J(J+1)}{2\mu R^2}$; we needed to perform only as many calculations as values of J we wished to include in the average. As such, we set a cut-off in the rotational quantum number, J_c. The condition imposed was that the relative population in $|0J_c\rangle$ be of order 10^{-5} or smaller compared to that in $|0J_{\max}\rangle$, where $J_{\max}$ is that J for which the population factor $P_{0J}(\beta)$ is largest. For $T = 300$ K, we found the appropriate choices to be $J_{\max} = 8$ and $J_c = 34$. At $T = 0$ K, of course, $J_{\max}$ and J_c are both rigorously 0; however, nuclear spin selection rules prevent conversion of *para*nitrogen to *ortho*nitrogen under typical laboratory conditions [106]. As a result, there will be a $2:1$ ratio of molecules in $J = 0$ and $J = 1$, respectively, directly after a quench from room temperature.

With the canonical densities $\rho_{0J}(R;\beta)$ in hand, we constructed the total density $\rho(R;\beta)$ by taking a weighted average with respect to the populations of the $|0J\rangle$. (This is a very minor approximation at 300 K, since even the largest relative contribution from the $|1J\rangle$ states is 7 times smaller than that for $|0J_c\rangle$. At 0 K, it is no approximation at all.) That is,

$$\rho(R;\beta) \approx \frac{Z}{Z_c}\sum_{J=0}^{J_c} P_{0J}(\beta)\rho_{0J}(R;\beta) \tag{3.13}$$

where the partition function ratio ensures a normalized average and $Z_c = \sum_{J=0}^{J_c} g_N(J)e^{-\beta E_{0J}}$ is the appropriately restricted partition function.

As was true in the classical case, the quantum density is very nearly Gaussian; the distinction is that it is significantly broader due to tunneling into the classically-forbidden regions on either side of the well. Because there is little change in the density between states with low values of J, the two distinct 0 K scenarios are essentially indistinguishable at this level of approximation.

3.4.5 Classical and quantum-classical spectral calculations

For the class of transitions shown in Figure 3.1A, densities dictate the intensity of the X-ray absorption for specified values of R. The associated transition energies are simply the energy differences between the fitted ground- and excited-state potentials. The spectra thus obtained were binned in the transition energy (to the nearest millielectronvolt) for convenience in plotting and (more importantly) so that spectral degeneracy would be properly reflected.

Upon quantizing the ground state, transitions to the classical excited state are made almost exclusively from $v = 0$, with rotational levels populated commensurate with the temperature. The resulting minimum transition energy, which includes contributions from the zero-point energy of the ground state, is lower than for the analogous classical transition. These spectra were also binned to the nearest millielectronvolt.

3.4.6 Franck-Condon spectral calculations

The Franck-Condon spectral calculations were carried out for the same set of states $|vJ\rangle$ as in the ground-state density calculations. Based on the number of peaks in the experimental spectrum, we chose to include those states on the fitted excited-state potential with $v' \in \{0, \ldots, 6\}$; the range of rotational quantum number chosen was $J' \in \{1, \ldots, 34\}$, determined by choosing the excited-state rotational cut-off value J'_c to be that for which $E_{0J'_c}$ first appreciably exceeds E_{10}. This criterion was used in part for convenience and in part to ensure that a reasonable spread of transition energies would be covered by our calculation. Franck-Condon factors $|\langle v'J'|vJ\rangle|^2$ were then computed numerically from the DVR wavefunctions and scaled by the population factor $P_{vJ}(\beta)$. The spectrum was constructed by combining the results of these calculations and applying an additional scale factor such that the height of the first peak in the computed spectrum matches that from the experiment; this latter scale factor may be interpreted as incorporating the modulus of the electronic transition dipole moment, which we have not calculated explicitly. The experiment yields results in arbitrary units, in any case; the absolute cross section is not measured and not available for comparison.

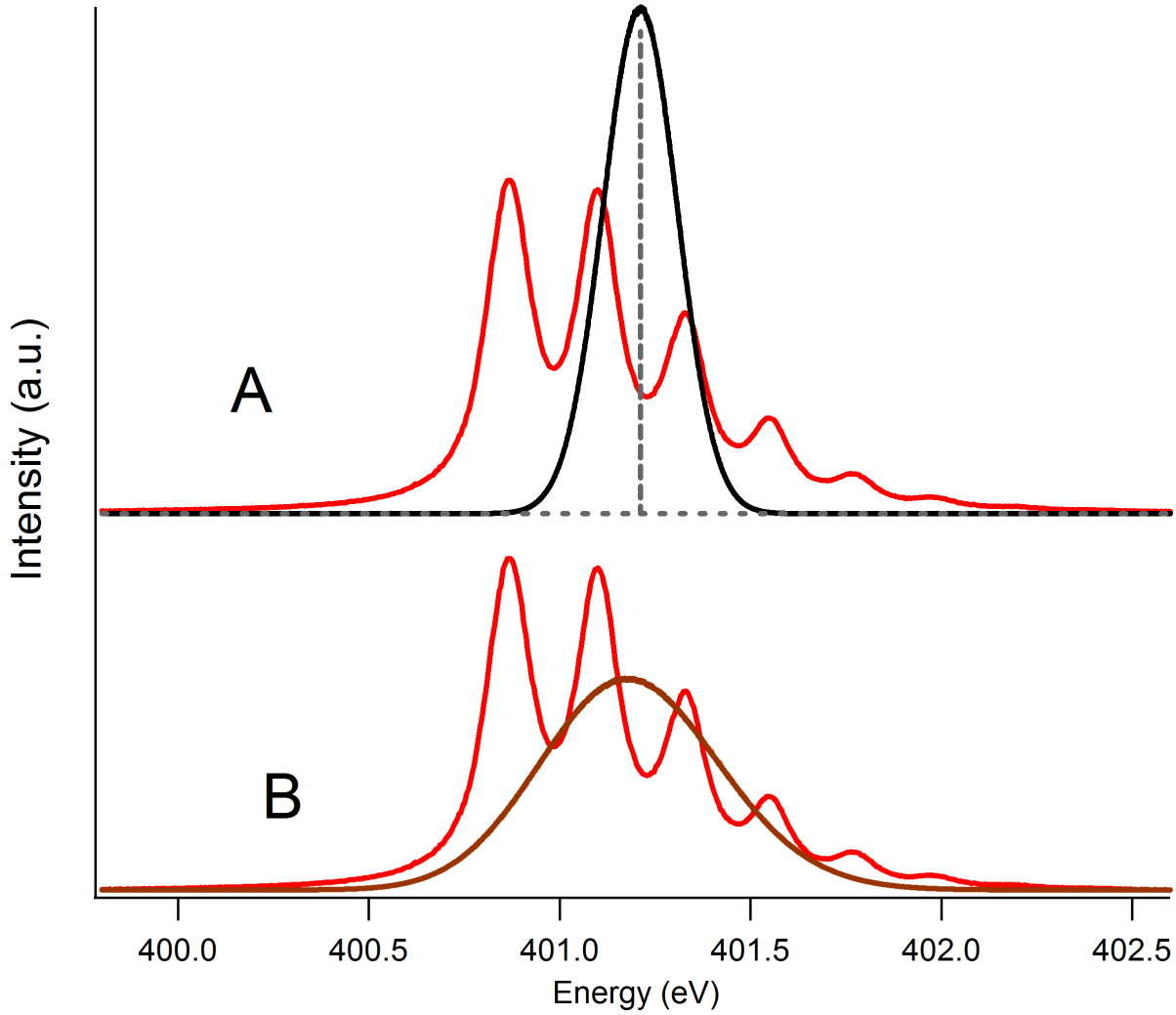

Figure 3.4: Panel A shows the experimental spectrum (red) and the spectra generated by transitions between classical curves, using the classical density, at 300 K (black) and 0 K (grey dashes). Note that the spectrum is too narrow, featureless, and has an onset too high in energy. Panel B makes the same comparison for the spectra generated by transitions between classical curves but using the quantum densities (brown). The 0 K spectrum in Panel B is completely overlapped by the 300 K spectrum.

3.5 Results and discussion

Figure 3.4 is a direct comparison to experiment of our results for the spectra arising from purely classical transitions; we have shifted all of our spectra, irrespective of the model used

to obtain them, to align energetically with the experimental spectrum of Yates et al. [93] In Panel A, the classical density is used, and, much as one would expect, the result is a near-Gaussian spectrum lacking any non-trivial structure. (In the 0 K limit, the spectrum is essentially a delta function, though not of infinite intensity.) We discuss this simplest model here in order to help establish what relevant features of the spectrum become apparent at which level of approximation.

When the quantum densities are used instead, as in Panel B of Figure 3.4, the absorption profile broadens substantially, and the (now comparatively small) maximum shifts by 42 meV. Of greater interest is that the spectrum obtained using this model is almost completely temperature-invariant; because only the lowest vibrational level is appreciably populated, and because the densities of the various rotational modes are very nearly identical, the overall ground state density — and, thus, the spectrum — does not change significantly between 300 K and 0 K. (This near-complete insensitivity to lowered temperature holds for all of our quantized spectra; we address the question of higher temperatures in the context of our conclusions.) We see, then, that tunneling spreads the density over a wider range of R, as it must, but no model neglecting the quantum energetics will contain any additional *structure*. Unsurprisingly, one must (at the very least) quantize the ground state.

The results of the ground-state quantization and subsequent application of the spectral model of Equation 3.3 (which, we recall, requires information equivalent to that obtained in the convergent limit of a PIMD calculation) are shown in Figure 3.5. The spectrum calculated at 0 K displays a single peak with infinitely sharp onset followed by a comparatively broad decay. The speed of the onset is due to the fact that all transitions now originate either from a single averaged state ≈ 2 cm^{-1} above the true ground state (after a quench from room temperature) or from the ground state alone (at absolute thermal equilibrium); to add insult to injury in this respect, the small displacement of the electronic potential minima (≈ 0.05 Å) will result in many transitions to the relatively flat bottom of the excited-state well. At 300 K, the averaged state will have somewhat higher energy (as stressed by the offset between our two spectra in Figure 3.5), but the transitions continue to originate almost exclusively from the well bottom, as is consistent with the average density.

Results from the ensemble-average spectral model of Equation 3.5 are shown in Figure 3.6. The spectrum calculated at 0 K is exactly the same as that in Figure 3.5; we shift its onset to match that of the 300 K spectrum, for purposes of a comparison to be made momentarily. At 300 K, we see a substantially weaker onset — were we to plot the two model spectra at the same integrated intensity, the 0 K model would be ≈ 6.5 times taller! The peculiarly ragged features before the onset are the source of this change; they correspond to transitions from the higher-J states, which are now spaced by up to 15 meV (and by substantially more from the onset, which is associated with the lowest several values of J). Transitions from these states are further emphasized (for even J) by nuclear spin

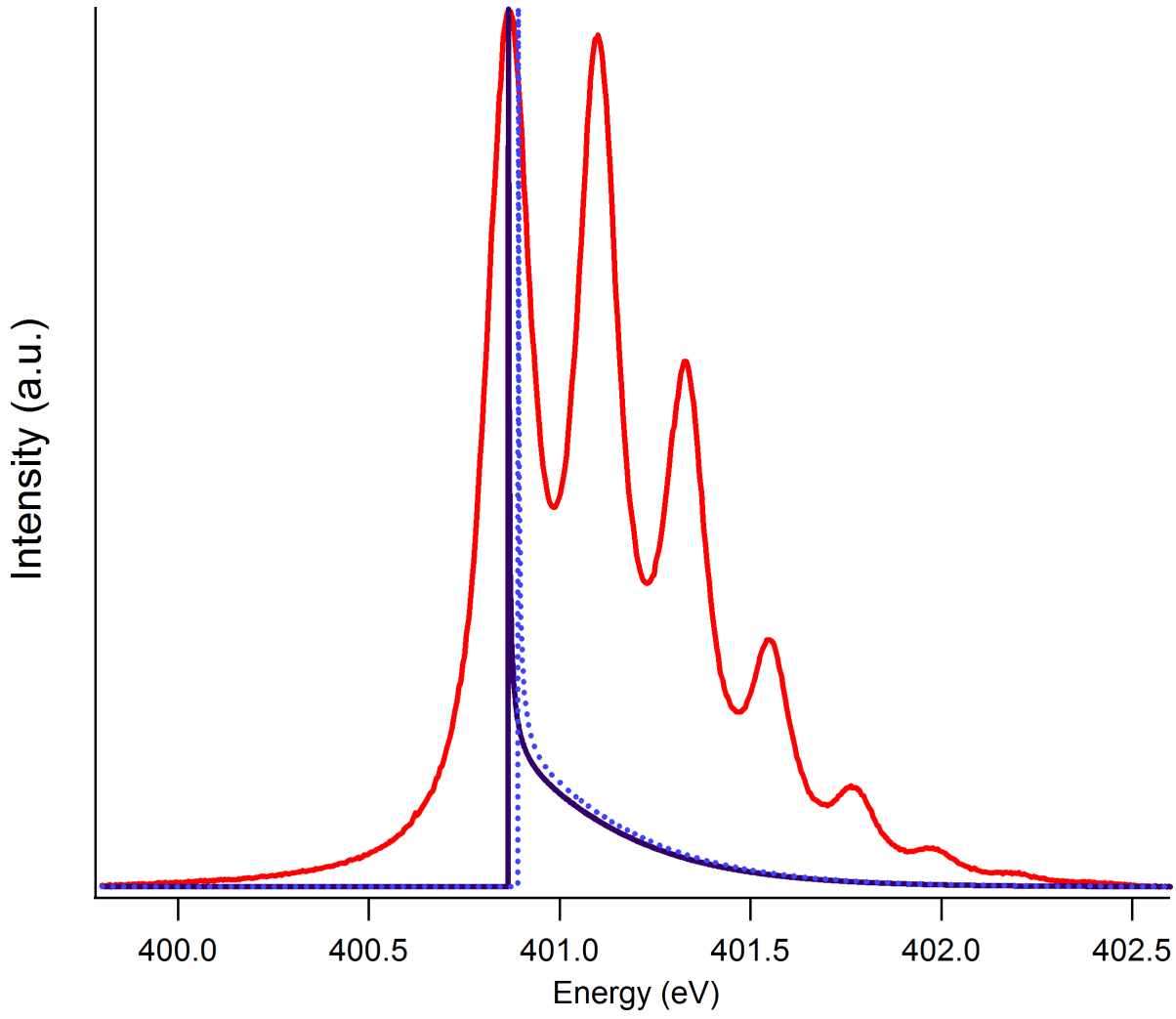

Figure 3.5: Comparison of the experimental spectrum (red) and the spectra generated by transitions from an averaged ground state to the classical excited state (per the model of Equation 3.3) at 300 K (dark blue) and 0 K (blue dots).

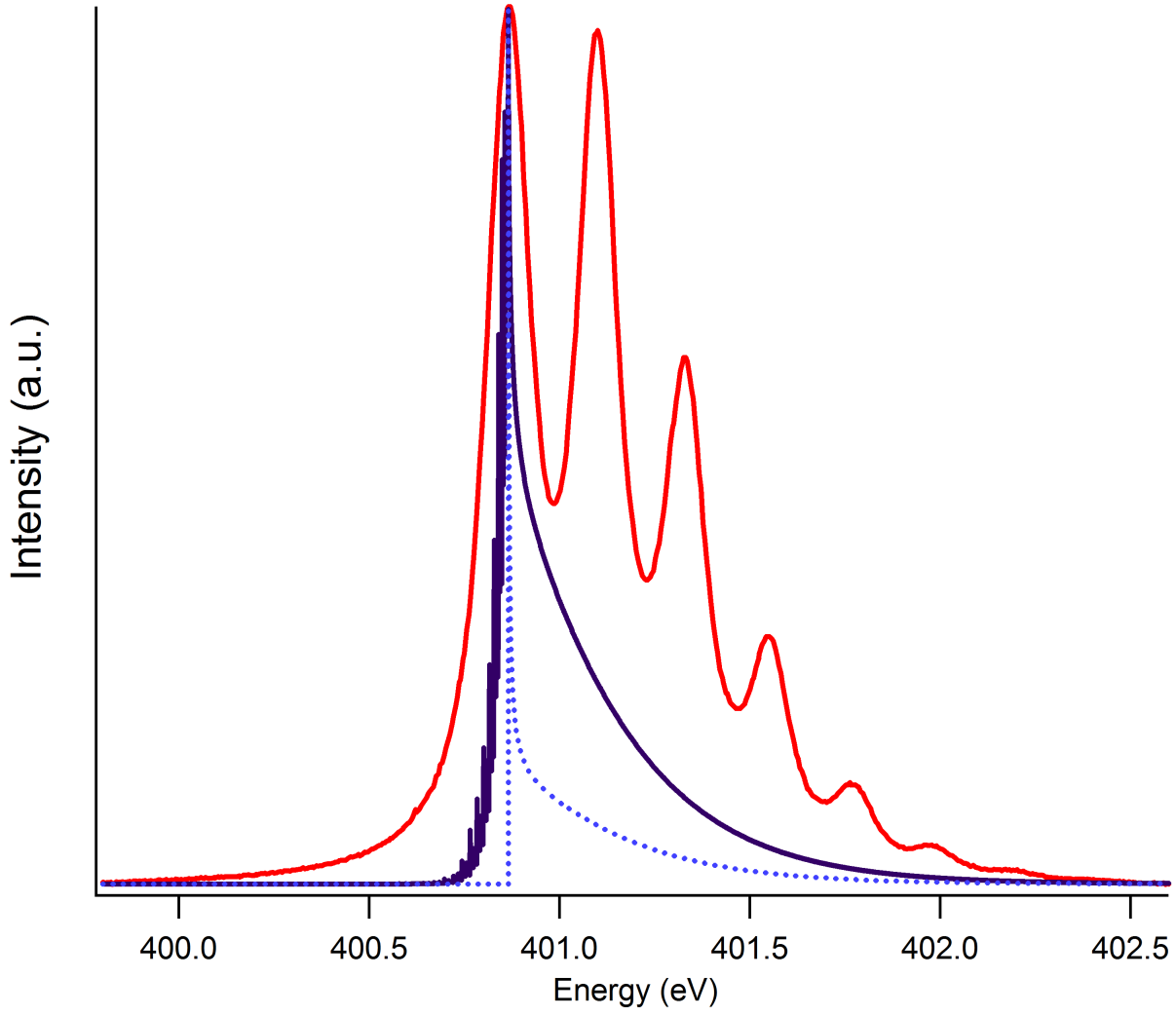

Figure 3.6: Comparison of the experimental spectrum (red) and the ensemble-averaged spectra generated by transitions from individual quantized ground states to the classical excited state (per the model of Equation 3.5 at 300 K (dark blue) and 0 K (blue dots).

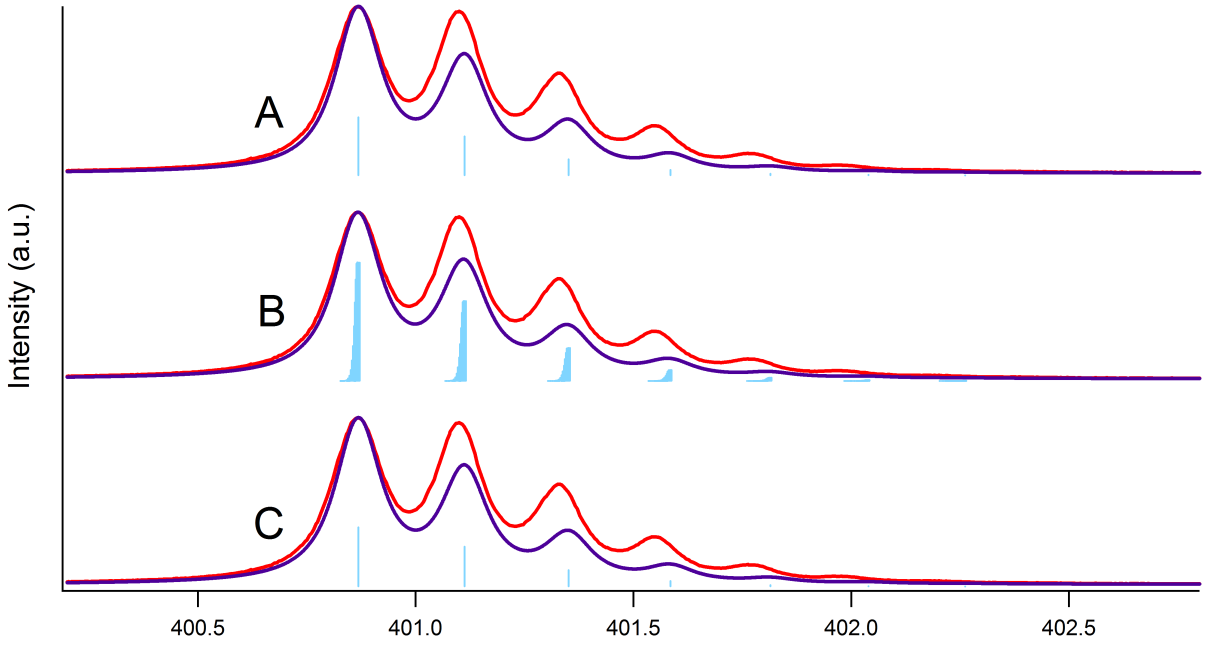

Figure 3.7: Panel A shows the experimental spectrum (red) and the spectrum generated by purely vibrational transitions from the ground to the excited state (light blue impulses) broadened with a Voigt lineshape (dark blue). The 0 K vibrational spectrum is indistinguishable from that for 300 K. Panel B makes the same comparison for rovibrational transitions at 300 K, Panel C for rovibrational transitions at 0 K. In all cases, the Voigt lineshape is the convolution of a 115 meV FWHM Lorentzian and a 38.4 meV FWHM Gaussian.

statistics. Each such "ragged peak" is associated with a spectrum similar in form to that for the system at 0 K — a sharp onset with a higher-energy tail — and intensity is thus removed from the blue-shifted regions in transition energy. The cumulative effect is the observed weaker onset and slower decay of the spectrum as a whole.

As we have seen, quantization of the ground state results in a sharp Franck-Condon-like peak. It is clear, however, that an accurate representation of the Franck-Condon structure of the experimental spectrum requires that the excited state be quantized as well.

We begin by quantizing both states only vibrationally, yielding the stick spectrum shown in light blue in Figure 3.7A. (There is essentially no difference between a 0 K and a 300 K spectrum in this picture owing to the minimal change in thermal population for $v = 1$.) Because the pure vibrational transitions (to a good approximation) set the positions of the peaks, this model is effectively that used in fitting experimental spectra.

We broaden this stick spectrum in the following way: Using the widths Yates et al. determined experimentally — 115 meV FWHM Lorentzian and 38.4 meV FWHM Gaussian broadening [93] — we replace each peak by a Voigt lineshape centered at the same transition energy and of the same maximum intensity. The individual profiles are summed on a 1 meV grid, and the first peak in the resulting curve is scaled to match the experiment, yielding the dark blue spectrum in Figure 3.7A. (Note that we adopt the Gaussian broadening reported by Yates et al. as a reasonable, if small, estimate of the instrumental error for *all* of our spectra; it cannot be determined a priori.) Owing to the shifting and scaling just mentioned, the location and height of the first peak cannot be used to judge the quality of the spectrum; its width is a respectable match to the experiment. As v' increases, however, our peaks are displaced progressively higher in transition energy from their experimental locations, and their heights decay much too quickly.

Although rotational transitions cannot be resolved spectroscopically, we thought it worthwhile to estimate the associated contribution to the broadening of the spectrum. Results of the rovibrational Franck-Condon spectral calculation are shown at 300 K in Figure 3.7B and at 0 K in Figure 3.7C, with stick spectra in light blue as before. When the spectra are broadened by the same Voigt lineshapes as before, the dark blue lines are obtained. Comparison of the stick spectra in Panels 3.7B and 3.7C indicates that rotational quantization leads directly to a very modest intrinsic "broadening" of the spectrum, in the sense of formation of closely-clustered groups of peaks associated with a single vibrational transition. The magnitude of this rotational effect at room temperature is, however, practically negligible, and we must add broadening to achieve a better fit to the data. Some experimentation leads to an estimate of 121 meV lifetime broadening, in general agreement with the values from many previous experimental studies [91] and the Auger lifetime estimate [92], and relatively close to the 115 meV width reported from the high-resolution experiment of Yates et al. [93]. We must stress, however, that we have arrived at this result by constructing the spectrum literally "from the ground state up," while the experimental broadening figures are determined purely by fitting. As such, we find the agreement to be a striking confirmation of the robustness of our approach.

We are not aware of any experimental studies of the N_2 NEXAFS spectrum at low temperature; given the negligible narrowing effect due to quenching of higher rovibrational states as the temperature is decreased, we think it unlikely that any will be performed soon. High-temperature experiments might be of interest, however: As contributions from $v > 0$ become non-negligible, shoulders will appear that are of spacing identical to that observed in the ground state spectrum but with an additional energy redshift of ΔE_{v0}. A simple population analysis suggests that $v = 1$ will first make a contribution of 10% or more at ≈ 1500 K.

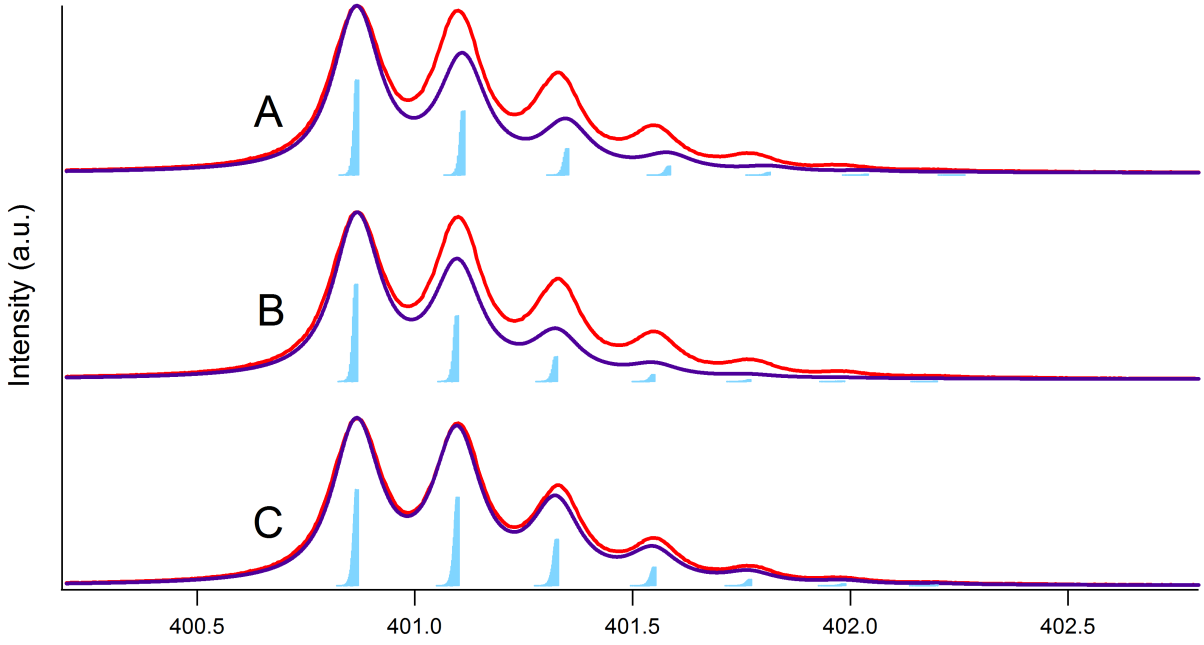

Figure 3.8: Panel A shows the experimental spectrum (red) and the spectrum generated by rovibrational transitions from the ground to the excited state (light blue impulses), as defined by our Gaussian fits, and broadened with a Voigt lineshape (dark blue) at 300 K. Panel B makes the same comparison, except that the excited-state potential is replaced by the empirical Morse curve; Panel C further replaces the DFT ground state with the $\mathrm{MLR}_4(6,8)$ potential.

The simplest explanation of the peak-location and -height discrepancy we observe is that the DFT ground- and excited-state potential geometries are different from those of the real physical states involved in the X-ray absorption process. Specifically, as mentioned previously, we would expect that our over-binding potential curves overestimate zero-point energy and the vibrational level spacing. The blue line in Figure 3.2 is the $\mathrm{MLR}_4(6,8)$ ground-state potential developed by Le Roy et al. from fitting to experimental data for vibrational levels up to $v = 19$ [110]; it compares favorably to configuration-interaction results obtained by Gdanitz [113]. Comparison to our ground-state fits shows that the well is of the correct width but displaced to higher R by 0.01 Å. An analogous comparison may be made for the excited state: The blue line in Figure 3.3 is the Morse potential derived from spectroscopic constants for nitrogen reported by Chen et al. (see Appendix A and also [109] for more details); our fitted curve is not meaningfully displaced from its empirical counterpart, but it is too narrow.

The results presented in Figure 3.8 address the question of how much improvement will be

visible in the spectrum when a better-quality ground- or excited-state potential curve is used. *Some* improvement is to be expected, since an empirical potential must necessarily incorporate "the right answer," in some sense. Panel 3.8A reproduces the spectrum from Panel 3.7B, with both states those determined by our DFT calculations and subsequent fitting. Panel 3.8B substitutes the fitted Morse potential [109] for the excited state curve, resulting in a marked improvement in the peaks' locations; Panel 3.8C involves the additional replacement of the ground-state potential by $\mathrm{MLR}_4(6,8)$ [110], which leads to a dramatic improvement in peak heights. In other words, our constrained DFT approach does a reasonably good job in predicting the fine structure in the N_2 spectrum, but there is room for improvement. It is possible that we could do better simply by adding points to the mesh of energies and adding Gaussians to the functional form we used in constructing our fit — thereby capturing ever more subtle details of the curve, its gradient, and its curvature. To achieve significant improvement, however, we most likely must use higher-level theory.

Another possible, though minor, source of the discrepancy between our peaks' locations and heights and those observed experimentally is that we have neglected Λ-splitting of the $\pm$ components of the $^1\Pi_u$ term with increasing J [106]. Although this effect will be on the order of fractions of a wavenumber for low values of J, it could be significant for the higher values included, growing as large as tens of wavenumbers (or larger). If the effect were strong enough for high J, contributions from *ortho*nitrogen would disappear (as the rotational selection rule would prevent it from coupling to the symmetry-allowed $^1\Pi_u^+$ state). Even assuming that the $^1\Pi_u^-$ term were still near enough to degenerate with $^1\Pi_u^+$ that we could ignore its being symmetry-forbidden, we would have to add the J-dependent splitting (or combination defect) by hand, drawing values from an appropriate experiment [106]. Thus, while it is possible that Λ-splitting might contribute, it is difficult to say what the effect of including it might be.

3.6 Concluding remarks and future work

In this chapter, we have shown that the NEXAFS spectrum can be predicted semiquantitatively using a combination of constrained density functional theory and exact methods for quantization of the nuclear motions. In the process, we have explored a hierarchy of models for the spectrum and established which of its salient features appear at what level of approximation. Specifically, a featureless (essentially Gaussian) spectrum is obtained at the purely classical level; a sharp onset is found when the ground state has been vibrationally quantized; and the full Franck-Condon structure is recovered on quantization of the excited state. We have also addressed the possibility of non-trivial temperature dependence in the spectrum: Low-temperature experiments will most likely be unrewarding, but there may be some interest in high-temperature work. Finally, we have shown that it

is possible to improve the predicted spectrum by using constrained DFT in combination with more accurate potentials — the *most* accurate, quite naturally, being one fitted to experimental observations.

3.6.1 A straightforward extension

The research discussed in this chapter has been presented several times since its publication. I was asked on more than one such occasion whether we had tried to construct spectra using the Franck-Condon model and potential curves from higher-level wavefunction theory, and whether those spectra are in substantially closer agreement with experiment. The spectrum in Panel 3.8C likely represents something close to an upper limit on the quality of results obtainable from work along these lines, since it is based on empirical potentials; even so, we are pursuing a definitive answer.

In collaboration with K. V. Lawler, we are developing a ground-state potential energy curve for N_2 at the CCSD(T) level and in the aug-cc-pVXZ basis (X $\in$ {T, Q}, with subsequent TQ extrapolation; all calculations performed using Q-Chem [114]). We are taking special care to ensure that we obtain the proper septet-spin reference at dissociation, i.e., a pair of quartet nitrogen atoms. The excited state curve presents more of a challenge, since we have not yet identified an off-the-shelf approach that preserves the spirit of the constrained DFT calculation — namely, straightforward determination of single-point energies for molecules with excited-state electron configurations. We may be obliged to modify a publicly-available electronic structure code for the purpose; or we may abandon this approach by analogy altogether and adopt, for example, the admirably well-documented method of Duflot [99, 103, 104].

3.6.2 Larger challenges

Not all future work in this area, of course, is intended to fill in relatively minor factual gaps; far from it! We are interested, for example, in expanding the XCH method to X-ray emission processes and in moving away from PBE and toward more modern functionals. Of particular interest to me, however, is the challenge of accounting for nuclear quantization in larger and/or more complex systems than N_2. Given that rotations seem unlikely ever to contribute measurably to the spectrum under typical experimental conditions, we will omit them in future work.

Homonuclear, closed-shell diatomics of all types are likely to be amenable to treatment along the lines discussed here, as their physics will not be complicated significantly by radical character, conical intersections, etc. Heteronuclear and/or open-shell diatomics (such as NO) will pose more of a challenge, for the following reasons: Heteronuclear diatomics will have two distinct core-to-LUMO absorption bands that must be treated separately; these

bands arise from constrained-DFT excited states that dissociate to different ion pairs. (Of course, if we are not interested in the X-ray absorption associated with one or the other atom, this is no problem and presents no additional work.) Correlation effects in open-shell diatomics may be incompletely or incorrectly captured, degrading or completely compromising the quality of the DFT states.

In addition to the proliferation of distinct absorption bands and the correlation effects just mentioned, conical intersections may begin to play a role for polyatomics [115]. Such features of the potential energy surface are important to real-time dynamics, and they may not be properly localized by our constrained DFT method. That said, they may be of little or no consequence if they are sufficiently far from the global minimum — but there may be degenerate or near-degenerate minima, as well.

Let us assume, for the sake of argument, that the above issues are immaterial or can be avoided for a given polyatomic molecule. It is relatively straightforward to obtain the normal modes of vibration and their frequencies from an electronic structure calculation; if these modes have sufficiently large force constants and are weakly coupled, it may be reasonable to quantize the nuclear motion analytically on a multi-dimensional surface composed of harmonic oscillators or of frequency-matched Morse oscillators. The latter might work especially well, since the so-called "diagonal anharmonicity" of a single mode with increasing v can be many times larger than the intermode coupling [116]; it would, however, introduce additional parameters in need of optimization into the method. Barring such substantial simplifications, it would be necessary to map the potential energy surface in displacements along the normal coordinates, such that the associated grid scales exponentially with the number of modes. Of course, if large-amplitude displacements are a factor, efforts in this direction may be moot; normal modes are determined in a harmonic framework that will not meaningfully capture anharmonic vibrations.

Some of the problems discussed above could be mitigated with the help of recently-published methods for localization of modes; these methods are analogous to orbital localization schemes commonly in use among electronic-structure theorists [117]. The modes nearest the core-excited atom would form a good "first-guess" set for use in mapping the potential energy surface; and since fewer local than normal modes may be physically relevant, it is conceivable that the size of the grid would grow slower than exponentially with the number of atoms. The remaining modes could be treated as harmonic or Morse oscillators, with the total vibrational wavefunction for the molecule a simple direct product of the analytical ones and those obtained from the DVR.

A heroic application of these ideas would be to a truly complex system, e.g., a liquid or a crystal. Liquids present the same challenges as large polyatomics, with precious few opportunities for simplification (apart from the introduction of periodic boundary condi-

tions with box sizes on the order of the correlation length). Crystals, especially atomic crystals such as diamond, may be more reasonable targets; we would expect to have to simulate a relatively small number of unit cells within the periodic box, and vibrations around the lattice sites should be fairly stiff. Deeper properties of crystalline systems, such as site symmetry [118], might also allow for some simplifications. Such applications remain, however, well beyond the horizon.

Chapter 4

Toward a derivation of ring polymer molecular dynamics

4.1 Introduction[1]

Onsager's regression hypothesis has been paraphrased by Chandler as follows [22]: "Relaxation of macroscopic non-equilibrium disturbances is governed by the same laws as the regression of spontaneous microscopic fluctuations in an equilibrium system." One of its consequences is the connection between various equilibrium properties — transport coefficients, most notably [119] — and correlation functions, expressions of the form

$$C_{AB}(t) = \langle A(0)B(t)\rangle = \frac{1}{Q}\int_{-\infty}^{\infty} \mathrm{d}\mathbf{p}_0\,\mathrm{d}\mathbf{x}_0\,\rho(\mathbf{p}_0,\mathbf{x}_0)A(\mathbf{p}_0,\mathbf{x}_0)B(\mathbf{p}_t,\mathbf{x}_t)$$

with $\rho(\mathbf{p},\mathbf{x})$ the density in the full phase space of the system for the desired (typically canonical) ensemble, Q the associated partition function, $\mathbf{p}_t$ and $\mathbf{x}_t$ the classically-evolved phase space coordinates, and A and B arbitrary measurable quantities. When normalized by its maximum, the correlation function describes the extent to which two measurements separated by the interval t can be said to be independent, with $C_{AB}(t) = \pm 1$ therefore implying maximal correspondence (or anti-correspondence) between them. If $C_{AB}(t)$ saturates to zero after an initial induction period, during which time it may nevertheless *accidentally* pass through the origin, the quantities A and B are understood to become totally independent (or "uncorrelated").

These classical relationships can be imported wholesale into quantum mechanics by way of the correspondence principle. For example, the isotropic self-diffusion constant D for a 3D

[1] The work in this chapter is an elaboration and extension of three sets of notes co-authored with Tom Miller.

system may be written

$$D = \frac{1}{3}\int_0^\infty \mathrm{d}t\, C_{\mathbf{v}\cdot\mathbf{v}}(t)$$

where $C_{\mathbf{v}\cdot\mathbf{v}}(t)$ is the average (over the N constituents of the system) of the velocity autocorrelation function,

$$C_{\mathbf{v}\cdot\mathbf{v}}(t) = \frac{1}{Z}\frac{1}{N}\sum_{n=1}^{N} \mathrm{Tr}\left[e^{-\beta H}\frac{\mathbf{p}_n}{m}\cdot\left(e^{\frac{it}{\hbar}H}\frac{\mathbf{p}_n}{m}e^{-\frac{it}{\hbar}H}\right)\right]$$

and Z is the quantum canonical partition function,

$$Z = \mathrm{Tr}\left[e^{-\beta H}\right] \tag{4.1}$$

The quantity within the trace may be interpreted quite naturally within the Heisenberg picture as a thermally-weighted product of the canonical "velocity" operator $\frac{\mathbf{p}_k}{m}$ with itself at a later time. The trace performs the average, and division by the partition function ensures normalization. In this sense, $C_{\mathbf{v}\cdot\mathbf{v}}(t)$ is precisely equivalent to its classical counterpart.

Any arbitrary correlation function of local (i.e., only position-dependent) operators may be written as the above description implies, namely,

$$C_{AB}(t) = \frac{1}{Z}\mathrm{Tr}\left[e^{-\beta H}Ae^{\frac{it}{\hbar}H}Be^{-\frac{it}{\hbar}H}\right] \tag{4.2}$$

The close connection between such quantum-mechanical expressions and their classical counterparts means that much of their mathematical structure and intuitive content is clear. Applications for large systems remain challenging, however, primarily due to the computational cost of exact real-time propagation. A common response to this challenge has been to perform purely classical simulations and then to "patch up" the results with one of several approximate quantum correction factors [120–123]. Another option is to use semiclassical theory, with classical molecular dynamics simulations as input [16, 124].

The approach to be discussed in the present chapter — ring polymer molecular dynamics, or RPMD [17] — does not fall neatly into either category. It does not consist of a multiplicative patch to be applied to a classical result; nor is it the product of controlled approximations to an exact expression. Rather, RPMD is founded on a calculated (and ultimately successful) bet on a heuristic extension of certain useful results in quantum statistical mechanics.

4.2 The classical isomorphism

Let us return to Equation 4.1. Because the trace is invariant with respect to a change in basis, we may choose to evaluate it using position eigenstates $\{|x_0\rangle\}$:

$$Z = \int_{-\infty}^{\infty} \mathrm{d}x_0 \langle x_0 | e^{-\beta H} | x_0 \rangle$$

Splitting the canonical density operator into N pieces and inserting $N-1$ resolutions of the identity in position, we obtain

$$\begin{aligned} Z_N &= \int_{-\infty}^{\infty} \mathrm{d}\mathbf{x} \langle x_0 | e^{-\beta_N H} | x_{N-1} \rangle \dots \langle x_n | e^{-\beta_N H} | x_{n-1} \rangle \dots \langle x_1 | e^{-\beta_N H} | x_0 \rangle \\ &= \int_{-\infty}^{\infty} \mathrm{d}\mathbf{x} \prod_{n=1}^{N} \Omega_n(\beta) \end{aligned}$$

where we have set $\beta_N = \frac{\beta}{N}$, adopted the convention $x_N = x_0$, and defined the high-temperature density matrix elements

$$\Omega_n(\beta_N) = \langle x_n | e^{-\beta_N H} | x_{n-1} \rangle \tag{4.3}$$

These matrix elements are related to short-time transition amplitudes of the time-evolution operator by the Wick rotation, $-i\hbar\beta \leftrightarrow t$ [125]. We may therefore make the appropriate substitution in the well-known path-integral result [126]

$$\Omega_n(t) = \sqrt{\frac{m}{2\pi\hbar i t}} \exp\left[\frac{im}{2\hbar t}(x_n - x_{n-1})^2 - \frac{it}{\hbar}\frac{V(x_n) + V(x_{n-1})}{2}\right] \tag{4.4}$$

and arrive at

$$Z_N = \left(\frac{m}{2\pi\hbar^2\beta_N}\right)^{\frac{N-1}{2}} \int_{-\infty}^{\infty} \mathrm{d}\mathbf{x} \exp\left[\sum_{n=1}^{N}\left(-\frac{m}{2\hbar^2\beta_N}(x_n - x_{n-1})^2 - \beta_N V(x_n)\right)\right] \tag{4.5}$$

Z_N approaches the exact partition function Z as $\mathrm{O}(N^{-3})$ owing to the Trotter approximation made in evaluating the $\Omega_n(t)$ [127]. In other words,

$$Z = \lim_{N\to\infty} Z_N$$

Let's rearrange Equation 4.5 slightly:

$$\begin{aligned} Z_N &= \left(\frac{m}{2\pi\hbar^2\beta_N}\right)^{\frac{N-1}{2}} \int_{-\infty}^{\infty} \mathrm{d}\mathbf{x} \exp\left[-\beta_N \sum_{n=1}^{N}\left(\frac{m}{2\hbar^2\beta_N^2}(x_n - x_{n-1})^2 + V(x_n)\right)\right] \\ &= \left(\frac{m}{2\pi\hbar^2\beta_N}\right)^{\frac{N-1}{2}} \int_{-\infty}^{\infty} \mathrm{d}\mathbf{x} \exp\left[-\beta_N \sum_{n=1}^{N}\left(\frac{m\omega_N^2}{2}(x_n - x_{n-1})^2 + V(x_n)\right)\right] \end{aligned} \tag{4.6}$$

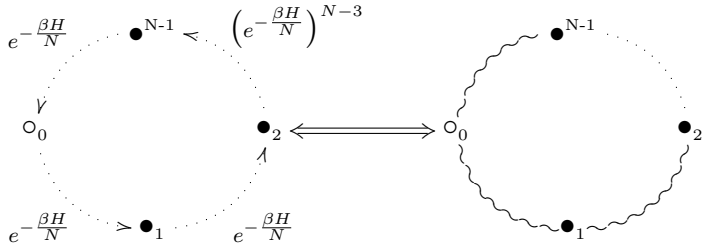

Figure 4.1: The classical isomorphism between the quantum canonical partition function and the configurational partition function for a classical ring polymer, diagrammed for a single realization of bead coordinates $\mathbf{x} = \{x_1, x_2, \ldots, x_N\}$. The visual convention used is explained in Section 4.3.

We now see that the quantum partition function Z at temperature β is the $N \to \infty$ limit of the *classical configurational* partition function at higher temperature β_N for a set of particles connected by harmonic springs with frequency $\omega_N = \frac{1}{\hbar\beta_N}$. These particles are colloquially termed "beads," and the composite classical object is called the "ring polymer." The relationship between these two partition functions and the associated objects is the "classical isomorphism."

4.3 Aside: a note on diagrams

Figure 4.1 summarizes what we have learned so far. It is necessary, therefore, to explain the conventions used in diagramming various expressions throughout this chapter.

- The starting point — in the sense of being represented by the rightmost ket in a given expression — is the open circle ($\circ$). Indices will be omitted from here on.
- Dotted lines indicate that intervening points have been omitted. Wavy lines indicate harmonic springs.
- Solid arrows represent evolution in real time, while dotted arrows represent evolution in purely imaginary time (i.e., thermal averaging). Wavy arrows represent evolution in complex time.
- Double-headed arrows imply evaluation of an operator; unless otherwise specified, the evaluation takes place at *real* time $t = 0$.

I must stress that the diagrams presented here are not meant to depict spatial relationships between beads; indeed, some of the points in the diagrams may coincide in space.

4.4 The classical isomorphism, continued

Inasmuch as the partition function generates all other thermodynamic quantities [22], the prospect of computing it through purely classical simulation is attractive. One means to this end is Monte Carlo sampling. Another — that adopted by Parrinello and Rahman in their seminal work on the F center in molten NaCl [128] — is to perform path integral molecular dynamics (PIMD).

The idea is simple: One may take Equation 4.6 and insert $N-1$ additional resolutions of the identity, this time in momentum:

$$\begin{aligned} Z_N &= \left(\frac{m}{2\pi\hbar^2\beta_N}\right)^{\frac{N-1}{2}} \int_{-\infty}^{\infty} \mathrm{d}\mathbf{p}\,\mathrm{d}\mathbf{x} \exp\left[-\beta_N \sum_{n=1}^{N}\left(\frac{p_n^2}{2m_n} + \frac{m\omega_N^2}{2}(x_n - x_{n-1})^2 + V(x_n)\right)\right] \\ &= \left(\frac{m}{2\pi\hbar^2\beta_N}\right)^{\frac{N-1}{2}} \int_{-\infty}^{\infty} \mathrm{d}\mathbf{p}\,\mathrm{d}\mathbf{x} \exp\left[-\beta_N H_N(\mathbf{p},\mathbf{x})\right] \end{aligned} \tag{4.7}$$

The fictitious masses $\{m_n\}$ associated with the momenta are arbitrary, since unphysical; different choices will lead to somewhat different behavior of the method once implemented, but should not *in principle* change the results. Setting $m_n = m$ for all of the beads — the mass choice used in RPMD — the resulting classical equations of motion are

$$\begin{aligned} \dot{p}_n &= -m\omega_N^2(2x_n - x_{n-1} - x_{n+1}) - \left.\frac{\partial V}{\partial x_n}\right|_{x_n} \\ \dot{x}_n &= \frac{p_n}{m} \end{aligned} \tag{4.8}$$

These equations may be propagated using any combination of Hamiltonian integrator and thermostat [14, 89, 129–135]. Convergence may be tested simply by increasing the number of beads in the simulation, and there is a variety of estimators for the energy and other thermodynamic quantities [136, 137]. Strategies have also been developed to counter the stiffening of the ring polymer ($\omega_N \propto N$) and concomitant nonergodicity as N grows [131, 138, 139]. I believe it fair to say that the machinery of PIMD is both well-developed and well-understood.

In practice, the partition function is poorly converged, and thermodynamic averages of observable quantities — typically, but not always, local operators $A = A(\hat{x})$ — are more agreeable targets of computation. Since a cyclic permutation of bead labels $\{n\}$ should make no difference in the physics of the original quantum system, such quantities are evaluated as

$$\langle A \rangle_N = \frac{1}{Z_N}\frac{1}{(2\pi\hbar)^N} \int_{-\infty}^{\infty} \mathrm{d}\mathbf{p}\,\mathrm{d}\mathbf{x}\, A_N(\mathbf{x}) \exp\left[-\beta_N H_N(\mathbf{p},\mathbf{x})\right] \tag{4.9}$$

where we have defined the bead-averaged measurement

$$A_N(\mathbf{x}) = \frac{1}{N}\sum_{n=1}^{N} A(x_n)$$

All one must do to compute $\langle A\rangle_N$ is to run one or more molecular dynamics trajectories using Equations 4.8: At a given simulation time step $\tau \propto \Delta\tau$, the ring-polymer configuration $\mathbf{x}(\tau)$ and associated measurement $A_N(\mathbf{x}(\tau))$ corresponds to a sample from the quantum distribution. The MD time average of the measurement function will converge to $\langle A\rangle_N$ for sufficiently long runs, and the error in the result may be determined based on estimates of the correlation time for the simulation [140,141] and/or by computing the variance between simulations [142].

4.5 Correlation functions through PIMD?

Equation 4.9 can be related quite straightforwardly to the zero-time correlation function $C_{AB}(0) = \langle AB\rangle$ — the correlation between equilibrium fluctuations of operators A and B. One simply replaces A by the local operator product AB and computes $(AB)_N(\mathbf{x})$ over the course of the molecular dynamics simulation.

In the absence of such hard-won knowledge, we might instead have guessed that the operators are evaluated separately, but as averages over the ring polymer. Such a situation is a clear extension of the classical picture, where observables can always be measured strictly independently and arbitrarily accurately (though, naturally, the measured values might *not* be independent). We would then postulate the following form for $C_{AB}(0)$:

$$\langle AB\rangle_N = \frac{1}{Z_N}\frac{1}{(2\pi\hbar)^N}\int_{-\infty}^{\infty} \mathrm{d}\mathbf{p}\,\mathrm{d}\mathbf{x}\, A_N(\mathbf{x})B_N(\mathbf{x})\exp\left[-\beta_N H_N(\mathbf{p},\mathbf{x})\right] \tag{4.10}$$

This expression is not, in fact, wrong; rather, it corresponds to the zero-time version of a different type of correlation function than the standard one we have discussed until now. (We will show this fact explicitly as part of our work in Section 4.10.) The correlation function in question is the Kubo-transformed correlation function [143],

$$\widetilde{C}_{AB}(t) = \frac{1}{Z}\frac{1}{\beta}\int_0^{\beta} \mathrm{d}\lambda \mathrm{Tr}\left[e^{-(\beta-\lambda)H}Ae^{-\lambda H}e^{\frac{it}{\hbar}H}Be^{-\frac{it}{\hbar}H}\right] \tag{4.11}$$

which is related to $C_{AB}(t)$ through its Fourier transform; the constant of proportionality between these correlation functions when Fourier-transformed is, in fact, the commonly-used harmonic correction factor [17]. The essence of the Kubo transformation is that it accounts for all of the many ways that the system can interact with the external bath

over the time period t, and it includes the standard form ($\lambda = 0$) and another useful version, the symmetrized correlation function ($\lambda = \frac{\beta}{2}$), as terms in the average. Although these different forms of the correlation function contain the same information, I find the Kubo-transformed version's explicit inclusion of all two-term splittings of the system-bath interaction very appealing.

The Kubo-transformed correlation function shares a number of properties with its classical counterparts: It is real, even, and time-reversal symmetric, satisfying detailed balance [17]. (The standard form, on the other hand, is only guaranteed to be time-reversible.) In light of the close correspondence between Kubo-transformed and classical correlation functions, the question therefore arises: Can we use an expression of this type to calculate *dynamical* rather than *equilibrium* quantities?

4.6 Ring polymer molecular dynamics

4.6.1 The method

The answer to the question just posed is: "Why not?" To the extent that the time-dependent version of Equation 4.10

$$\langle A(0)B(t)\rangle_N = \frac{1}{Z_N}\frac{1}{(2\pi\hbar)^N}\int_{-\infty}^{\infty} \mathrm{d}\mathbf{p}\,\mathrm{d}\mathbf{x}\, A_N(\mathbf{x})B_N(\mathbf{x}(t))\exp\left[-\beta_N H_N(\mathbf{p},\mathbf{x})\right] \tag{4.12}$$

is simply the classical correlation function when $N = 1$, the introduction of additional beads (and, thus, additional information about the quantum statistics of the system) can only improve the result. Equation 4.12 is at the heart of ring polymer molecular dynamics.

Of course, there are better reasons to use RPMD than to pull the scientific equivalent of a shrug. Equation 4.12 has been shown to be exact for all values of t if the potential $V(x) = \frac{m\omega^2}{2}x^2$ is harmonic — assuming either A or B is linear in the position operator $\hat{x}$ [17]. And the RPMD value of the position autocorrelation function $\widetilde{C}_{xx}(t) = \frac{1}{\beta m\omega^2}\cos\omega t$ — which is related to the infrared absorption spectrum [22] — is not only exact for the harmonic potential, it is exact even in the classical limit, as shown in Figure 4.2 on the next page. The situation is somewhat less rosy for nonlinear operators and anharmonic potentials — see Figures 4.3 and 4.4 farther below — but is nevertheless a substantial improvement (especially at short times, since $C_{AB} = 0$ is guaranteed to be correct) over the classical result.

One final piece of evidence for the promise of RPMD is that the mass choice $\{m_n\} = m$ is (in a certain, limited sense) the unique "best" choice for short-time accuracy of the Kubo-transformed correlation function. This statement holds true for linear functions of $\hat{x}$ or $\hat{p}$;

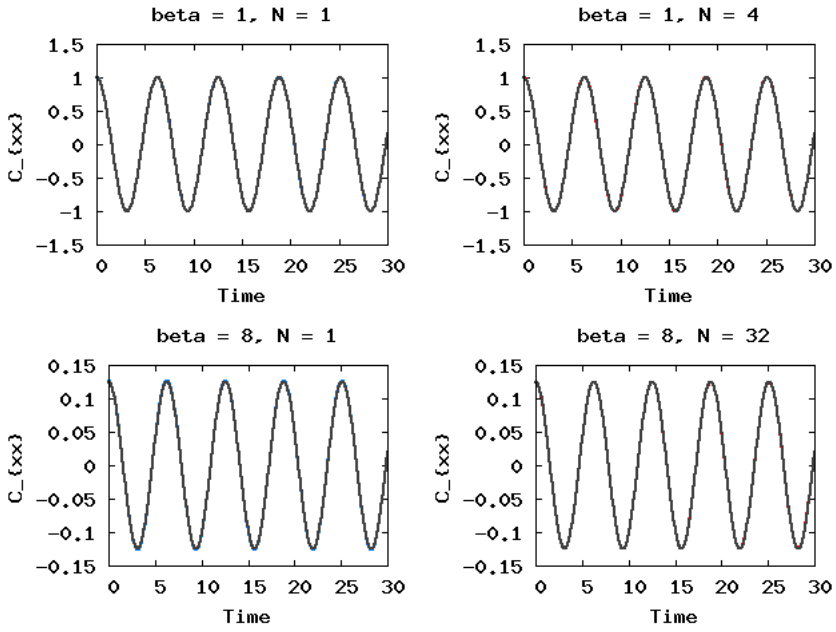

Figure 4.2: RPMD yields the exact position autocorrelation function $C_{xx}(t)$ for all values of N and t for the harmonic oscillator — at least, within statistical error. The (blue) classical and (red) RPMD curves are essentially completely obscured by the exact result, shown in black.

the associated error scales as $\mathrm{O}(t^8)$ for $\widetilde{C}_{xx}(t)$ and $\mathrm{O}(t^6)$ for $\widetilde{C}_{vv}(t)$ [144]. To be more precise, RPMD is the best method at short times of the class defined by all possible choices of masses $\{m_n\}$ in Equation 4.12; this family of methods includes partially-adiabatic centroid molecular dynamics (PA-CMD), the errors in which scale better by t^2 [145,146]. Although this improvement in scaling is desirable at times longer than $t = 1$ (in whatever units are natural to the system of interest, such as the thermal time $\hbar\beta$), it results in worse answers when $t < 1$. (More information on the relative merits of RPMD and CMD is provided in the next section.)

As RPMD's parameterization for short-time accuracy might suggest, the method performs best for small values of t. Any and all improvements made over classical mechanics are based on a proper treatment of quantum statistical effects; real-time quantum coherences do not enter into the picture at *any* value of t, and RPMD will be less accurate the more important they become. The same is true, at least in principle, for exchange effects — consider liquid helium in the superfluid regime — but this omission has not been significant in the very-low-temperature applications done to date (namely, studies of liquid *para*hydrogen and of quantum diffusion in ice) [147–151].

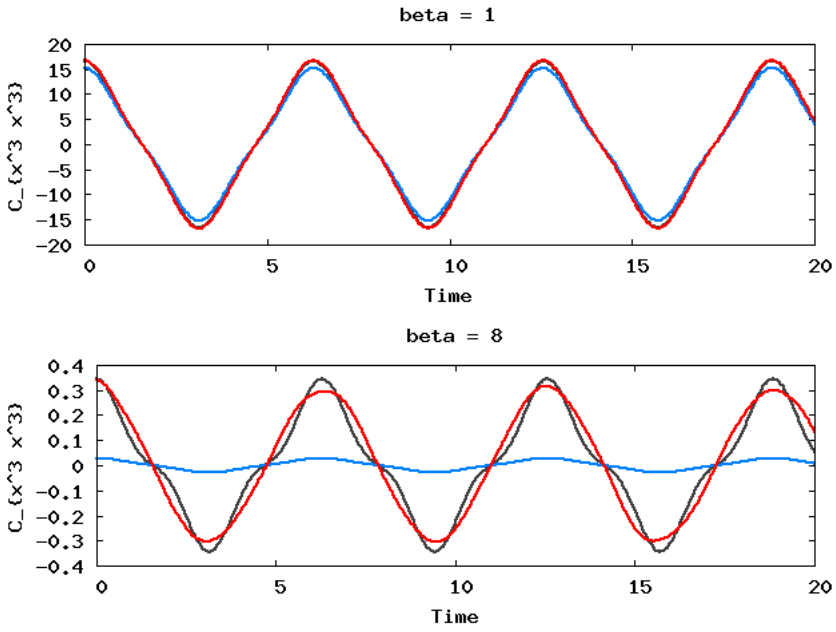

Figure 4.3: RPMD outperforms classical molecular dynamics simulation for the x^3 autocorrelation function, as it should. In each panel, the black curve is the analytical result; the red curve is the RPMD result ($N = 4$ in the upper and $N = 32$ in the lower panel); and the blue curve is the classical result.

4.6.2 Details of model calculations

RPMD is clearly closely related to its direct progenitor, PIMD — not least in that the means of implementing the two methods are exactly the same. The principal difference is that the classical dynamics of the ring polymer on the extended surface (comprising the physical potential $V(x)$ and the harmonic interbead forces) are taken seriously within RPMD as an approximation to the quantum particle's motion. The practical consequences of this interpretive leap are twofold: First, time-translation symmetry (i.e., insensitivity of the physics to the origin of t) allows for many values of $C_{AB}(t = \text{small})$ to be extracted from a single simulation. Second, any given trajectory simulation must at the *very least* be as long as the longest time for which we wish to calculate $C_{AB}(t)$.

The model calculations presented in Figures 4.2, 4.3, and 4.4 were very simple to perform. The potentials used were $V(x) = \frac{1}{2}x^2$ for the harmonic and $V(x) = \frac{1}{4}x^4$ for the quartic potential calculations, such that $m = \omega = 1$. The calculations were performed at two choices of temperature, corresponding to $\beta = 1, 8$.

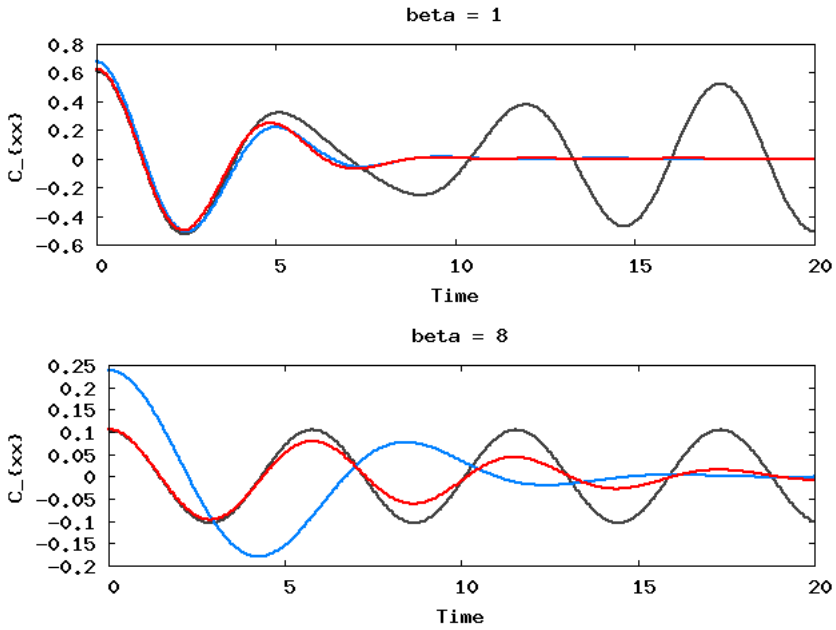

Figure 4.4: RPMD makes more modest improvements over classical molecular dynamics in the case of the the position autocorrelation function for a strong quartic oscillator. The black curve in each panel is the exact result as computed using the Colbert-Miller DVR; the red curve is the RPMD result ($N = 4$ in the upper and $N = 32$ in the lower panel); and the blue curve is the classical result.

Rather than implementing a specific thermostatting method for these calculations, I used a less-efficient but convenient sampling approach: The bead positions were initially distributed symmetrically around the origin with coordinate $x_n = \cos \frac{2\pi n}{N}$; the momenta were drawn from the Maxwell-Boltzmann distribution at β_N. An NVE (microcanonical) molecular dynamics simulation of length $t = t_{\max}$ was run using the reversible reference-system propagator algorithm [130], with the bead forces evaluated and the system propagated over N substeps per harmonic potential step. The momenta were then reassigned — this procedure repeating until the desired number of trajectories had been completed. Each trajectory used in the calculations presented here was of length $t = 150$, with the timestep chosen to be $\Delta t = 0.5$.

Bead-averaged values of the relevant operators (e.g., $A_N(\mathbf{x})$) were recorded at each timestep, and the value of the correlation function at a given time was determined as follows: Within a single trajectory, the average was computed of all pairs of values $A_N(\mathbf{x}(\tau))$ and $A_N(\mathbf{x}(\tau'))$ with $\tau' - \tau = t$. These trajectory-averaged values were then themselves averaged in order to obtain the final value of $C_{AA}(t)$. Convergence was tested by increasing the number of tra-

jectories (no fewer than 5×10^4 for any given method) and by comparison with the results given by Craig and Manolopoulos [17]; exact results were computed either analytically (in Figures 4.2 and 4.3) or (in Figure 4.4) by using the Colbert-Miller DVR described in Chapter 3. The only notable change to the procedure outlined there results from the expanded coordinate range $(-\infty, \infty)$; the second term in each line of Equation 3.11 disappears, and i can extend over the entire range of integers $\{0, \pm 1, \pm 2, \dots\}$ [112].

4.7 Applications to realistic systems

Since its introduction, RPMD has been applied fruitfully to a variety of realistic systems, some large enough to allow for a rigorous treatment of finite-size effects [147, 148, 152]. Variant methods have been developed as well, and for different purposes. One version combines the basic method with maximum-entropy analytic continuation (MEAC) techniques in order to improve the predicted correlation functions [153]; another introduces a contraction scheme that allows varying numbers of beads for each quantum particle [154]. This latter variation is especially useful when some atoms are much heavier than other and, therefore, much less likely to display meaningful quantum effects. Ring contraction reduces the computational overhead of the method in such cases.

Applications include:

- Self-diffusion [147,148,155] and inelastic neutron scattering [149] in liquid *para*hydrogen and *ortho*deuterium. Although extremely low temperatures are involved — in the tens of Kelvin — RPMD's omission of exchange effects is of little consequence for the final results, as confirmed by good agreement with experiment and by quantum Monte Carlo simulations [150].

- Self-diffusion [152, 155] in and infrared spectroscopy [156] of water. RPMD confirms enhancement (compared to the classical liquid) of the diffusion constant and orientational relaxation; see the end of this section for more on the computed spectrum.

- Reaction rates in model problems [157, 158] and in bimolecular systems, specifically the prototypical proton exchange (H + H_2), abstraction (F + H_2),and heavy-light-heavy (Cl + HCl) reactions [159]. RPMD rates compare favorably with those calculated exactly using scattering theory.

- Proton transfer between phenol and trimethylamine in liquid chloromethane [160]. RPMD fares poorly compared to various flavors of quantum transition state theory in this case, yielding a rate smaller by an order of magnitude.

- Proton and muonium diffusion in water and hexagonal ice [151]. The results are in accord with experiment, even at a temperature for which the diffusion process is wholly quantum mechanical (8 K).

- Injection and trapping of a solvated electron in liquid helium and water [161, 162]. RPMD is in general agreement with other mixed quantum-classical methods, and it performs especially well in the high-density regime.

The primary competitor of RPMD at present is centroid molecular dynamics (CMD), a method based (as the name suggests) on the dynamics of the ring-polymer centroid [18, 19, 163, 164]. The partially-adiabatic version (PA-CMD) [145, 146] is equivalent to RPMD, apart from a different choice of fictitious masses, $\{m_n\}$ [144]. As that relationship might imply, neither method is, in general, clearly better-suited to a given application than the other, even granting CMD the advantage in longer-time accuracy. One exception to this rule of thumb is for prediction of the infrared spectrum: The vibrational modes of the ring polymer tend to contaminate the relevant range of energies within RPMD, while PA-CMD shifts these motions out of the spectral window [156]. The cost of a spectrum free of such contamination is the concomitant redshifting of *all* motions by CMD [165, 166].

4.8 The foundational problem

The evidence presented above certainly supports the usefulness and relative accuracy of RPMD, but there is still no derivation of the method — at least, in the sense of a clear set of steps leading from an exact quantum-mechanical expression to Equation 4.12. There has, however, been some progress toward understanding the connections between RPMD and other dynamical methods; for example, RPMD rate theory in the deep-tunneling regime corresponds to a finite-difference approximation to paths predicted by semiclassical instanton theory [167].

The sticking point in any derivation of RPMD — attempted or otherwise — will be the emergence of real-time dynamics on the extended potential surface. That such dynamics should be a fair approximation to the exact dynamics is especially puzzling, and it is the one characteristic of the method that is most in need of explanation. The work that follows is, in essence, an attempt to seek out the source of this striking correspondence.

Section 4.9 presents several formally-equivalent discretized versions of the Kubo-transformed correlation function; each provides a somewhat different starting point for a possible derivation of RPMD. Section 4.10 continues, in the same spirit, with a careful exploration of what happens when one of these expressions is evaluated and approximated further, according to the logic of some as-yet unpublished work by Prof. W. H. Miller [168]. When we have learned as much as we can from this "forward" approach, we shift gears entirely; Section 4.11 consists of an attempt to "reverse-engineer" RPMD, starting with a set of Dirac delta functions encoding classical dynamics on the extended surface.

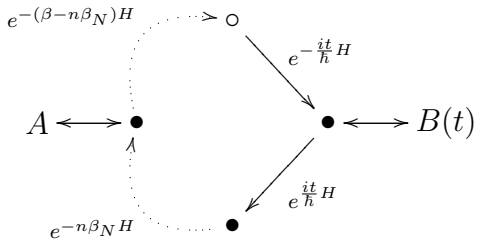

Figure 4.5: Diagram for a single realization (i.e., n) of Equation 4.13.

4.9 Suggestive forms of $\widetilde{C}_{AB}(t)$

We will begin by rewriting Equation 4.11, which introduced the Kubo-transformed correlation function in its pristine quantum mechanical state:

$$\widetilde{C}_{AB}(t) = \frac{1}{Z}\frac{1}{\beta}\int_0^\beta \mathrm{d}\lambda \,\mathrm{Tr}\left[e^{-(\beta-\lambda)H}Ae^{-\lambda H}e^{\frac{it}{\hbar}H}Be^{-\frac{it}{\hbar}H}\right]$$

Rather than working directly with this form, we discretize the integral over λ, thereby making explicit the bead structure generated by the density operators. The specific discretization method used is the trapezoid rule,

$$\int_a^b \mathrm{d}x\, f(x) \approx \lim_{N\to\infty}\frac{b-a}{N}\left[\frac{f(a)+f(b)}{2}+\sum_{n=1}^{N-1} f(a+n\frac{b-a}{N}\right]$$

which introduces an error of $\mathrm{O}(N^{-2})$ [169]. Making the appropriate identifications and discretizing Z as well, we obtain the following discretized expression (diagrammed in Figure 4.5):

$$\begin{aligned}\widetilde{C}_{AB}(t) \;\approx\; \lim_{N\to\infty}\frac{1}{Z_N}\frac{1}{N}\Bigg\{&\frac{1}{2}\mathrm{Tr}\left[e^{-\beta H}Ae^{\frac{it}{\hbar}H}Be^{-\frac{it}{\hbar}H}\right]\\ &+\sum_{n=1}^{N-1}\mathrm{Tr}\left[e^{-(\beta-n\beta_N)H}Ae^{-n\beta_N H}e^{\frac{it}{\hbar}H}Be^{-\frac{it}{\hbar}H}\right]\\ &+\frac{1}{2}\mathrm{Tr}\left[Ae^{-\beta H}e^{\frac{it}{\hbar}H}Be^{-\frac{it}{\hbar}H}\right]\Bigg\}\end{aligned} \tag{4.13}$$

Since the trace is invariant to cyclic permutations of its contents, this sum has a very appealing structure: When N is odd, each term with index $n < \frac{N}{2}$ will have a partner of index $N-n$ that is its Hermitian conjugate. If N is even, one unique term indexed by $n = \frac{N}{2}$ will not have a distinct counterpart — rather, it will be its own conjugate. This

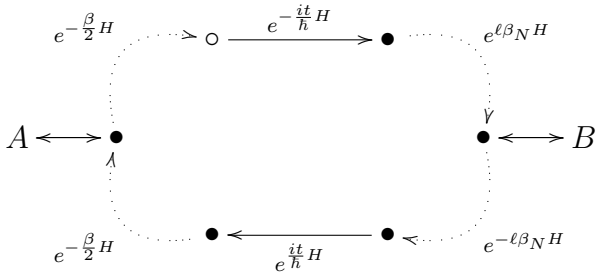

Figure 4.6: Diagram for a single realization (i.e., ℓ) of Equation 4.14.

special term is the symmetrized version of the correlation function.

Equation 4.13 will be the focus of Section 4.10 because it is relatively easy to manipulate, but there are other versions of the correlation function that are more exotic and which allow different opportunities for approximation. To find the first of these (diagrammed in Figure 4.6), we make a change of index from n to $\ell = n - \frac{N}{2}$, then commute some of the exponentials:

$$\begin{aligned}\widetilde{C}_{AB}(t) \;\approx\; \lim_{N\to\infty} \frac{1}{Z_N}\frac{1}{N}\Bigg\{ & \frac{1}{2}\mathrm{Tr}\left[e^{-\frac{\beta}{2}H}Ae^{-\frac{\beta}{2}H}e^{\frac{it}{\hbar}H}e^{\frac{\beta}{2}H}Be^{-\frac{\beta}{2}H}e^{-\frac{it}{\hbar}H}\right] \\ & + \sum_{\ell=1-\frac{N}{2}}^{\frac{N}{2}-1} \mathrm{Tr}\left[e^{-\frac{\beta}{2}H}Ae^{-\frac{\beta}{2}H}e^{\frac{it}{\hbar}H}e^{-\ell\beta_N H}Be^{\ell\beta_N H}e^{-\frac{it}{\hbar}H}\right] \\ & + \frac{1}{2}\mathrm{Tr}\left[e^{-\frac{\beta}{2}H}Ae^{-\frac{\beta}{2}H}e^{\frac{it}{\hbar}H}e^{-\frac{\beta}{2}H}Be^{\frac{\beta}{2}H}e^{-\frac{it}{\hbar}H}\right]\Bigg\} \end{aligned} \tag{4.14}$$

Interest in this form of the correlation function lies in the resemblance of the operator sum (where we have temporarily double-counted surface terms for the sake of concision)

$$\sum_{\ell=-\frac{N}{2}}^{\frac{N}{2}} e^{-\ell\beta_N H}Be^{\ell\beta_N H}$$

to a similarity transformation or a discrete Fourier transform. Inasmuch as Equation 4.14 indicates the real-time propagation of this composite "object" rather than of a single point, there may be value in pursuing this expression. Our past work with this particular cast of the correlation function was hobbled by an inconsistent treatment of the Wick rotation, and I have not yet had the opportunity to revisit it.

There is one other form of the correlation function that I wish to present here; it is obtained

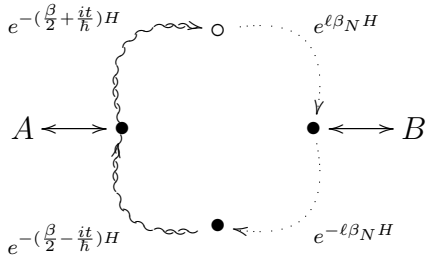

Figure 4.7: Diagram for a single realization (i.e., ℓ) of Equation 4.15.

from Equation 4.14 by combining the time-evolution operators with the ℓ-independent components of the thermalization (as diagrammed in Figure 4.7):

$$\begin{aligned}\widetilde{C}_{AB}(t) \;\approx\; \lim_{N\to\infty} \frac{1}{Z_N}\frac{1}{N}\Bigg\{ & \frac{1}{2}\mathrm{Tr}\left[e^{-\left(\frac{\beta}{2}+\frac{it}{\hbar}\right)H} A e^{-\left(\frac{\beta}{2}-\frac{it}{\hbar}\right)H} e^{\frac{\beta}{2}H} B e^{-\frac{\beta}{2}H}\right] \\ & + \sum_{\ell=1-\frac{N}{2}}^{\frac{N}{2}-1} \mathrm{Tr}\left[e^{-\left(\frac{\beta}{2}+\frac{it}{\hbar}\right)H} A e^{-\left(\frac{\beta}{2}-\frac{it}{\hbar}\right)H} e^{-\ell\beta_N H} B e^{\ell\beta_N H}\right] \\ & + \frac{1}{2}\mathrm{Tr}\left[e^{-\left(\frac{\beta}{2}+\frac{it}{\hbar}\right)H} A e^{-\left(\frac{\beta}{2}-\frac{it}{\hbar}\right)H} e^{-\frac{\beta}{2}H} B e^{\frac{\beta}{2}H}\right]\Bigg\} \end{aligned} \tag{4.15}$$

As Wick demonstrated [125], there is nothing to prevent us from using analytically-continued versions of the time-evolution and density operators. We may, therefore, also consider *complex* (as opposed to purely real or imaginary) time evolution. To imagine such a process is gratifying, since beads will (in a sense) be spawned, moved, and (potentially) merged or removed by the action of a single operator. It remains to be seen whether this expression will bear any sweeter fruit than the others.

4.10 Deriving toward RPMD

4.10.1 Preliminaries

With the stage set and our options explored, we return to the discretized version of the Kubo-transformed correlation function (Equation 4.13):

$$\begin{aligned}\widetilde{C}_{AB}(t) \approx \lim_{N\to\infty} \frac{1}{Z_N}\frac{1}{N}\Bigg\{ &\frac{1}{2}\mathrm{Tr}\left[e^{-\beta H}Ae^{\frac{it}{\hbar}H}Be^{-\frac{it}{\hbar}H}\right] \\ &+ \sum_{n=1}^{N-1}\mathrm{Tr}\left[e^{-(\beta-n\beta_N)H}Ae^{-n\beta_N H}e^{\frac{it}{\hbar}H}Be^{-\frac{it}{\hbar}H}\right] \\ &+ \frac{1}{2}\mathrm{Tr}\left[Ae^{-\beta H}e^{\frac{it}{\hbar}H}Be^{-\frac{it}{\hbar}H}\right]\Bigg\}\end{aligned}$$

We begin by writing the trace explicitly in the position basis and inserting a resolution of the identity between the thermalized operator A and the time-evolved operator B:

$$\begin{aligned}\widetilde{C}_{AB}(t) \approx \lim_{N\to\infty} \frac{1}{Z_N}\frac{1}{N}\Bigg\{ &\frac{1}{2}\int_{-\infty}^{\infty}\mathrm{d}x_0\,\mathrm{d}x_N\,\langle x_N|e^{-\beta H}A|x_0\rangle\langle x_0|e^{\frac{it}{\hbar}H}Be^{-\frac{it}{\hbar}H}|x_N\rangle \\ &+ \sum_{n=1}^{N-1}\int_{-\infty}^{\infty}\mathrm{d}x_0\,\mathrm{d}x_N\,\langle x_N|e^{-(\beta-n\beta_N)H}Ae^{-n\beta_N H}|x_0\rangle \\ &\qquad\qquad \times\langle x_0|e^{\frac{it}{\hbar}H}Be^{-\frac{it}{\hbar}H}|x_N\rangle \\ &+ \frac{1}{2}\int_{-\infty}^{\infty}\mathrm{d}x_0\,\mathrm{d}x_N\,\langle x_N|Ae^{-\beta H}|x_0\rangle\langle x_0|e^{\frac{it}{\hbar}H}Be^{-\frac{it}{\hbar}H}|x_N\rangle\Bigg\}\end{aligned}$$

We now have a set of nonlocal operators $A_N(n)$ which may (excepting the $n = 0$ and $n = N$ boundary terms) be written as

$$A_N(n) = \left(\prod_{\ell=n+1}^{N} e^{-\beta_N H}\right) A \left(\prod_{\ell=1}^{n} e^{-\beta_N H}\right)$$

The gist of this expression is that we must insert $n-1$ resolutions of the identity on the right-hand side, $N-n-1$ on the left-hand side, and 1 more on either side of A to obtain a proper path-integral expression. Recalling our definition of the high-temperature density matrix elements in Equation 4.3,

$$\Omega_n(\beta_N) = \langle x_n|e^{-\beta_N H}|x_{n-1}\rangle$$

we insert the necessary resolutions of the identity and obtain

$$\begin{aligned}\widetilde{C}_{AB}(t) \;\approx\; \lim_{N\to\infty} \frac{1}{Z_N}\frac{1}{N}\Bigg\{ &\frac{1}{2}\int_{-\infty}^{\infty} \mathrm{d}x_0 \left[\prod_{n=1}^{N}\int_{-\infty}^{\infty} \mathrm{d}x_N\, \Omega_n(\beta_N)\right] A(x_0)\langle x_0|e^{\frac{it}{\hbar}H}Be^{-\frac{it}{\hbar}H}|x_N\rangle \\ &+ \sum_{n=1}^{N-1}\int_{-\infty}^{\infty} \mathrm{d}x_0 \left[\prod_{n=1}^{N}\int_{-\infty}^{\infty} \mathrm{d}x_N\, \Omega_n(\beta_N)\right] A(x_n)\langle x_0|e^{\frac{it}{\hbar}H}Be^{-\frac{it}{\hbar}H}|x_N\rangle \\ &+ \frac{1}{2}\int_{-\infty}^{\infty} \mathrm{d}x_0 \left[\prod_{n=1}^{N}\int_{-\infty}^{\infty} \mathrm{d}x_N\, \Omega_n(\beta_N)\right] A(x_N)\langle x_0|e^{\frac{it}{\hbar}H}Be^{-\frac{it}{\hbar}H}|x_N\rangle \Bigg\}\end{aligned}$$

This expression collapses quite nicely to yield the substantially more compact formula

$$\begin{aligned}\widetilde{C}_{AB}(t) \;\approx\; \lim_{N\to\infty} \frac{1}{Z_N}\frac{1}{N}\int_{-\infty}^{\infty} \mathrm{d}x_0 &\left[\prod_{n=1}^{N}\int_{-\infty}^{\infty} \mathrm{d}x_n\, \Omega_n(\beta_N)\right]\left[\frac{A(x_0)+A(x_N)}{2} + \sum_{n=1}^{N-1} A(x_n)\right] \\ &\times \langle x_0|e^{\frac{it}{\hbar}H}Be^{-\frac{it}{\hbar}H}|x_N\rangle\end{aligned}$$

Using the Wick-rotated form of the short-time propagator matrix element given in Equation 4.4, we arrive at the following intermediate result, which remains exact to within the quadratic trapezoid-rule discretization error:

$$\begin{aligned}\widetilde{C}_{AB}(t) \;\approx\; &\lim_{N\to\infty} \frac{1}{Z_N}\frac{1}{N}\left(\frac{m}{2\pi\hbar^2\beta_N}\right)^{\frac{N}{2}}\left[\prod_{n=0}^{N}\int_{-\infty}^{\infty}\mathrm{d}x_n\right] \\ &\times \exp\Bigg\{ -\frac{m}{2\hbar^2\beta_N}\sum_{n=1}^{N}(x_n - x_{n-1})^2 \\ &\qquad -\beta_N\left[\frac{V(x_0)+V(x_N)}{2} + \sum_{n=1}^{N-1} V(x_n)\right]\Bigg\} \\ &\times \left[\frac{A(x_0)+A(x_N)}{2} + \sum_{n=1}^{N-1} A(x_n)\right]\langle x_0|e^{\frac{it}{\hbar}H}Be^{-\frac{it}{\hbar}H}|x_N\rangle \qquad (4.16)\end{aligned}$$

Everything we have done so far is standard imaginary-time path integration, and the real-time dynamics remain exact as well (since we have made no approximations involving the time-evolution operators). If we were now to take the limit $t \to 0$, the locality of B would require that $x_0 = x_N$, forming the ring polymer and yielding Equation 4.10, the equilibrium quantity $\langle AB\rangle_N$, as was promised several pages ago.

4.10.2 A brief overview of the linear approximation

It seems wise to pause here and outline the major remaining steps in our attempt to wring RPMD from quantum mechanics. The logic to be applied was inspired by and drawn from

Prof. W. H. Miller's notes of July 2005 [168], but it is materially the same as that used to obtain the classical Wigner model (or linearized semiclassical initial value representation, LSC-IVR) from the IVR expression for the correlation function [170]. The distinction lies in the fact that the linearization is applied to the path integral expression for the propagator rather than to its corresponding IVR.

The specific procedure may be summarized as follows:

1. The forward and reverse time-evolution operators in Equation 4.16 will be written as path integrals with the same number of time slices, T, corresponding to $T-1$ inserted resolutions of the identity. The resulting path (with a single "bead" or time-sliced replica of the system chosen) will begin at x_N, move through a sequence of points x_s^- forward in time, resulting in the measurement of $B(x_t)$, and then move backward in time through a second sequence of points x_s^+ ending in x_0. The corresponding diagram is

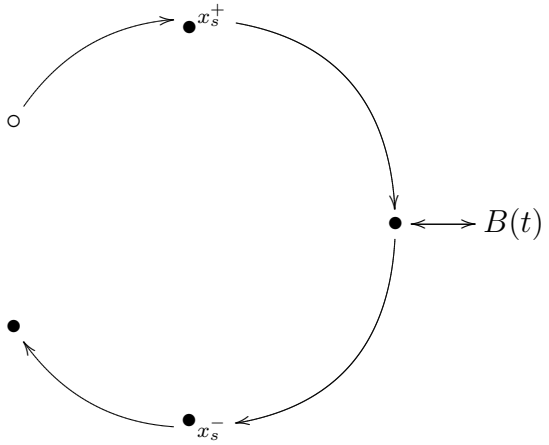

2. We adopt sum and difference variables for the two paths,

$$\begin{aligned} \bar{x}_s &= \frac{x_s^+ + x_s^-}{2} \\ \Delta x_s &= x_s^+ - x_s^- \end{aligned} \tag{4.17}$$

noting that the following relationships hold at the endpoints:

$$\begin{aligned} \bar{x}_0 &= \frac{x_0 + x_N}{2} \\ \bar{x}_t &= x_t \\ \Delta x_0 &= x_0 - x_N \\ \Delta x_t &= 0 \end{aligned}$$

It is clear when presented visually that this substitution covers the same area in coordinate space, such that we may make the replacement $\int \mathrm{d}x_s^- \int \mathrm{d}x_s^+ \to \int \mathrm{d}\bar{x}_s \int \mathrm{d}\Delta x_s$:

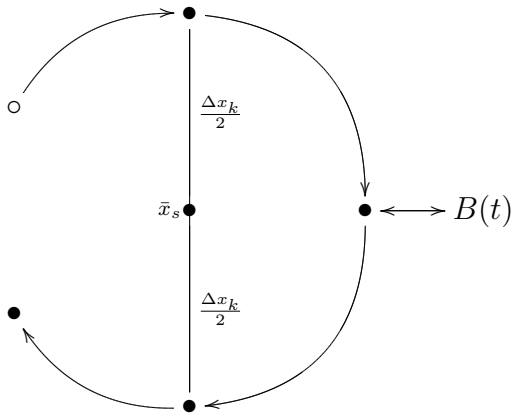

3. The previous two steps are exact to within discretization error. The approximate element enters by way of the fact that we Taylor-expand the potential around the sum variable $\bar{x}_s$ and truncate to first order, thereby assuming that the forward and reverse paths are close together — perhaps infinitesimally so. The resulting potential sums and differences are

$$\begin{aligned} V\left(\bar{x}_s + \frac{\Delta x}{2}\right) - V\left(\bar{x}_s - \frac{\Delta x}{2}\right) &\approx V'(\bar{x}_s)\Delta x_s + \mathrm{O}(\Delta x_s^3) \\ V\left(\bar{x}_s + \frac{\Delta x}{2}\right) + V\left(\bar{x}_s - \frac{\Delta x}{2}\right) &\approx 2V(\bar{x}_s) + \mathrm{O}(\Delta x_s^2) \end{aligned} \tag{4.18}$$

4. As we will soon see, it then becomes possible to integrate over the set of difference variables $\{\Delta x_s\}$. The result is a set of delta functions requiring the average path between $\bar{x}_0$ and x_t be a classical trajectory.

$$\circ^{\bar{x}_0} \xleftarrow[\text{formed by } \{\bar{x}_s\}]{\text{classical path}} \bullet^{x_t} \longleftrightarrow B(t)$$

4.10.3 Applying the linear approximation

The logic of the approximation having been established, we will proceed to apply it in detail. The first step is to insert a resolution of the identity in x_t,

$$\int_{-\infty}^{\infty} \mathrm{d}x_t \langle x_0 | e^{\frac{it}{\hbar}H} | x_t \rangle B(x_t) \langle x_t | e^{-\frac{it}{\hbar}H} | x_N \rangle$$

We want to insert $T-1$ resolutions of the identity into each matrix element. Defining the timestep of the time-slicing procedure to be $\Delta t = \frac{t}{T}$ and slightly modifying the matrix

elements from Equation 4.3 to read

$$\Omega_{s^{\mp}}(\Delta t) = \left\{ \begin{array}{l} \langle x_s^- | e^{-\frac{i\Delta t}{\hbar}H} | x_{s-1}^- \rangle \\ \\ \langle x_{s-1}^+ | e^{\frac{i\Delta t}{\hbar}H} | x_s^+ \rangle \end{array} \right\}$$

we obtain

$$\lim_{T\to\infty} \int_{-\infty}^{\infty} \mathrm{d}x_t \, B(x_t) \left[\prod_{s=1}^{T-1} \int_{-\infty}^{\infty} \mathrm{d}x_s^- \int_{-\infty}^{\infty} \mathrm{d}x_s^+ \right] \left[\prod_{s=1}^{T} \Omega_{s^+}(\Delta t) \Omega_{s^-}(\Delta t) \right]$$

After substituting in the short-time matrix elements, we find the following path integral expression (which, we should recall, is still exact in the limit of infinite time slices):

$$\begin{aligned} \langle x_0 | e^{\frac{it}{\hbar}H} B e^{-\frac{it}{\hbar}H} | x_N \rangle &= \lim_{T\to\infty} \left(\frac{m}{2\pi\hbar\Delta t} \right)^T \int_{-\infty}^{\infty} \mathrm{d}x_t \, B(x_t) \left[\prod_{s=1}^{T-1} \int_{-\infty}^{\infty} \mathrm{d}x_s^- \int_{-\infty}^{\infty} \mathrm{d}x_s^+ \right] \\ &\quad \times \exp \left\{ -\frac{im}{2\hbar\Delta t} \sum_{s=1}^{T} \left[(x_{s-1}^+ - x_s^+)^2 - (x_s^- - x_{s-1}^-)^2 \right] \right. \\ &\quad \left. + \frac{i\Delta t}{\hbar} \left[\frac{V(x_0) - V(x_L)}{2} + \sum_{s=1}^{T-1} \left(V(x_s^+) + V(x_s^-) \right) \right] \right\} \end{aligned}$$

Now we make the change to sum and difference variables, noting that the integrals over x_0 and x_N are not present in this portion of our expression and must be accounted for later. We also perform the potential expansions as given in Equation 4.18 and apply the following useful identity:

$$\begin{aligned} \sum_{s=1}^{T} \left[(x_{s-1}^+ - x_s^+)^2 - (x_s^- - x_{s-1}^-)^2 \right] &= \sum_{s=1}^{T} 2(\bar{x}_s - \bar{x}_{s-1})(\Delta x_s - \Delta x_{s-1}) \\ &= -2 \left[\sum_{s=1}^{T-1} (\bar{x}_{s+1} - 2\bar{x}_s + \bar{x}_{s-1}) \Delta x_s + (\bar{x}_1 - \bar{x}_0) \Delta x_0 \right] \end{aligned}$$

We then collect terms in the difference variables $\{\Delta x_s\}$. When the dust clears, we obtain the (perhaps?) simpler expression

$$\begin{aligned} \langle x_0 | e^{\frac{it}{\hbar}H} B e^{-\frac{it}{\hbar}H} | x_N \rangle &\approx \lim_{T\to\infty} \left(\frac{m}{2\pi\hbar\Delta t} \right)^T \int_{-\infty}^{\infty} \mathrm{d}x_t \, B(x_t) \left[\prod_{s=1}^{T-1} \int_{-\infty}^{\infty} \mathrm{d}\bar{x}_s \int_{-\infty}^{\infty} \mathrm{d}\Delta x_s \right] \\ &\quad \times \left[\prod_{s=1}^{T-1} \exp \left\{ \frac{i\Delta t}{\hbar} \left[\frac{m}{\Delta t^2} (\bar{x}_{s+1} - 2\bar{x}_s + \bar{x}_{s-1}) + V'(\bar{x}_s) \right] \Delta x_s \right\} \right] \\ &\quad \times \exp \left\{ \left[\frac{im}{\hbar\Delta t} (\bar{x}_1 - \bar{x}_0) + \frac{i\Delta t}{\hbar} \frac{V'(\bar{x}_0)}{2} \right] \Delta x_0 \right\} \end{aligned} \tag{4.19}$$

The integrals over $\{\Delta x_s\}$ may be evaluated using the combined Fourier and delta-function identity

$$\int \mathrm{d}x e^{-2\pi i c k x} = \frac{1}{|c|}\delta(k)$$

to give the product

$$\left(\frac{2\pi\hbar}{\Delta t}\right)^{T-1} \prod_{s=1}^{T-1} \delta\left[-\frac{m}{\Delta t^2}(\bar{x}_{s+1} - 2\bar{x}_s + \bar{x}_{s-1}) - V'(\bar{x}_s)\right]$$

In the continuous limit ($T \to \infty$, such that $\Delta t \to 0$), the term inside the delta function is equivalent to the requirement that the equation

$$-V'(\bar{x}(s\Delta t)) = m\ddot{\bar{x}}(s\Delta t)$$

be satisfied — in other words, the trajectory described by the $\{\bar{x}_s\}$ must be that satisfying Newton's equations of motion for classical mechanics. Or, to be more precise, the trajectory must be a classical trajectory at every moment in time but $t = 0$, whose behavior we will address in the next section. Rather than carry the delta functions around with us, we will write the entire collection as $\delta\left[\mathrm{CM}(1, T-1)\right]$.

Now we will recombine Equation 4.19 with Equation 4.16. In doing so, we note the effect of the change of variables,

$$\begin{aligned}
\int_{-\infty}^{\infty}\mathrm{d}x_0\int_{-\infty}^{\infty}\mathrm{d}x_N &\to \int_{-\infty}^{\infty}\mathrm{d}\bar{x}_0\int_{-\infty}^{\infty}\mathrm{d}\Delta x_0 \\
(x_N - x_{N-1})^2 + (x_1 - x_0)^2 &\approx (\bar{x}_0 - x_{N-1})^2 + (x_1 - \bar{x}_0)^2 - (x_1 - x_{N-1})\Delta x_0 \\
V(x_0) + V(x_N) &\approx 2V(\bar{x}_0) \\
A(x_0) + A(x_N) &\approx 2A(\bar{x}_0)
\end{aligned}$$

Error in all of the latter three equations will be of $\mathrm{O}(\Delta x_0^2)$, unless A is linear in $\hat{x}$; in that case, the last equation is exact. Also of interest is the fact that the second equation closes the imaginary-time path integral, bringing the endpoints x_0 and x_N together at their average, $\bar{x}_0$.

Combining the above results with Equations 4.19 and 4.16, we arrive at the following

expression for the linearized Kubo-transformed correlation function:

$$\begin{aligned}
\widetilde{C}_{AB}(t) \;\approx\; & \lim_{N,T\to\infty} \frac{1}{Z_N}\left(\frac{m}{2\pi\hbar^2\beta_N}\right)^{\frac{N}{2}}\left(\frac{m}{\Delta t^2}\right)^{T-1}\left(\frac{m}{2\pi\hbar\Delta t}\right) \\
& \times\left[\prod_{n=1}^{N}\int_{-\infty}^{\infty}\mathrm{d}x_n\right]\exp\left\{-\beta_N\sum_{n=1}^{N}\left[\frac{m\omega_N^2}{2}(x_n-x_{n-1})^2+V(x_n)\right]\right\} \\
& \times\left[\frac{1}{N}\sum_{n=1}^{N}A(x_n)\right]\int_{-\infty}^{\infty}\mathrm{d}x_t\,B(x_t)\left[\prod_{s=1}^{T-1}\int_{-\infty}^{\infty}\mathrm{d}\bar{x}_s\delta\left[\mathrm{CM}(1,T-1)\right]\right] \\
& \times\int_{-\infty}^{\infty}\mathrm{d}\Delta x_0\exp\left\{\left[\frac{im}{\hbar\Delta t}(\bar{x}_1-\bar{x}_0)+\frac{i\Delta t}{\hbar}\frac{V'(\bar{x}_0)}{2}+\frac{m}{2\hbar^2\beta_N}(x_1-x_{N-1})\right]\Delta x_0\right\}
\end{aligned}$$

All that remains to be done is the integral over Δx_0. Choosing the constant in the Fourier and delta-function identities to be the same as for the other time slices, we obtain

$$\begin{aligned}
\widetilde{C}_{AB}(t) \;\approx\; & \lim_{N,T\to\infty} \frac{1}{Z_N}\left(\frac{m}{2\pi\hbar^2\beta_N}\right)^{\frac{N}{2}}\left(\frac{m}{\Delta t^2}\right)^{T} \\
& \times\left[\prod_{n=1}^{N}\int_{-\infty}^{\infty}\mathrm{d}x_n\right]\exp\left\{-\beta_N\sum_{n=1}^{N}\left[\frac{m\omega_N^2}{2}(x_n-x_{n-1})^2+V(x_n)\right]\right\} \\
& \times\left[\frac{1}{N}\sum_{n=1}^{N}A(x_n)\right]\int_{-\infty}^{\infty}\mathrm{d}x_t\,B(x_t)\left[\prod_{s=1}^{T-1}\int_{-\infty}^{\infty}\mathrm{d}\bar{x}_s\delta\left[\mathrm{CM}(1,T-1)\right]\right] \\
& \times\delta\left[\frac{m}{\Delta t^2}(\bar{x}_1-\bar{x}_0)+\frac{V'(\bar{x}_0)}{2}-\frac{im}{2\Delta t\hbar\beta_N}(x_1-x_{N-1})\right]
\end{aligned} \tag{4.20}$$

The equation of motion for the first time step then becomes

$$\begin{aligned}
-V'(\bar{x}_0) &= \frac{2m}{\Delta t^2}(\bar{x}_1-\bar{x}_0)-i\frac{m}{\Delta t\hbar\beta_N}(x_1-x_{N-1}) \\
&= \frac{2m}{\Delta t^2}(\bar{x}_1-\bar{x}_0)-i\frac{m}{\Delta t\hbar\beta_N}(x_1-\bar{x}_0)-i\frac{m}{\Delta t\hbar\beta_N}(\bar{x}_0-x_{N-1})
\end{aligned}$$

Classical mechanics still rules the day, but with a twist: The imaginary terms represent competing "hysteretic damping forces" which dissipate energy more (less) strongly as the arrangement of x_1 and x_{N-1} becomes less (more) symmetrical around $\bar{x}_0$ and as the overall spread of the three beads increases (decreases) [171]. In essence, the more strained the geometry of the ring polymer in the neighborhood of $\bar{x}_0$, the less likely B will be measured to be significantly different from its value there — simply because it will lose more energy in the first step of the dynamics.

Interestingly enough, now that the imaginary-time ring polymer has closed, there is no reason to favor one bead over another as the initial point of the real-time dynamics. In other words, our final expression should really involve an averaged sum of terms with the classical trajectory originating at each x_n and with the time-evolved measurement $B(x_t(x_n))$. Each bead should be propagated independently according to the laws of classical mechanics, yet will feel the influence of its imaginary-time neighbors at $t = 0$!

4.10.4 Additional interpretation of our result

Note that we have been a little sloppy with respect to notation toward the end of this last subsection: For the purpose of the sums over $\{n\}$, we have replaced x_0 and x_N with the single variable $\bar{x}_0$ and invoked the resulting cyclic condition $n + N = n$. This identification allows us to make the relationship between the imaginary-time portion of the present expression and Equation 4.12 quite explicit, as below, by adding the appropriate resolutions of the identity in the fictitious momenta:

$$\begin{aligned}
\widetilde{C}_{AB}(t) &\approx \lim_{N\to\infty}\left(\frac{m}{2\pi\hbar^2\beta_N}\right)^{\frac{N}{2}}\frac{1}{Z_N}\int_{-\infty}^{\infty}\mathrm{d}\mathbf{x}\,A_N(\mathbf{x})\exp\left[-\beta_N V_N(\mathbf{x})\right] \\
&\quad \times(\text{terms associated with real-time dynamics}) \\
&\approx \lim_{N\to\infty}\left(\frac{1}{2\pi\hbar}\right)^{N}\frac{1}{Z_N}\int_{-\infty}^{\infty}\mathrm{d}\mathbf{p}\,\mathrm{d}\mathbf{x}\,A_N(\mathbf{x})\exp\left[-\beta_N H_N(\mathbf{p},\mathbf{x})\right] \\
&\quad \times(\text{terms associated with real-time dynamics})
\end{aligned}$$

In other words, if $B = 1$, we will always obtain the proper result for $\langle A\rangle_N$. That's quite reassuring!

The behavior of Equation 4.20 and subsequent expressions in the limit $t \to 0$ is more subtle: Consider our initial linearized result for the time-evolved matrix element of B, Equation 4.19. As $t \to 0$, any term with $\frac{1}{\Delta t}$ in the denominator will dominate the associated exponential of Δx_s and, thus, we may neglect the others in obtaining our delta functions. The leading constant will cancel, and the complete set of delta functions will reduce to the requirement that $\{\bar{x}_s\} = \bar{x}_0$. Because of the usual argument regarding cyclic relabelings, $B(x_t) \to B_N(\mathbf{x})$ and we recover the exact zero-time Kubo-transformed correlation function of Equation 4.10. Such is *not* true once we have arrived at Equation 4.20; although the collapse of the trajectory to a single point $\bar{x}_0$ does occur, a constant term proportional to Δt^{T-1} persists in the prefactor. The proper way to remove this behavior was suggested by Charulatha Venkataraman [172], namely, that we use a different version of the canonical partition function for this expression. We replace Z (and, by extension, Z_N) with the path-integrated, time-linearized version of the formally equivalent partition function

$$Z = \mathrm{Tr}\left[e^{-\beta H}e^{\frac{it}{\hbar}H}e^{-\frac{it}{\hbar}H}\right]$$

The behavior of this modified expression in the zero-time limit balances the pathology in the prefactor of Equation 4.20 such that we obtain the correct result for $\langle AB \rangle_N$ as well.

4.10.5 An interesting neighborhood

There is one final point of interest. Consider the set of imaginary-time beads $\{x_n^\circ\}$ that maximizes the exponential prefactor in Equation 4.20. If $V(x)$ is bounded from below, the argument of the exponential can be drawn from the range $(-\infty, 0]$ such that the exponential itself varies from $(0, 1]$. The maximum condition is therefore

$$\sum_{n=1}^{N} V(x_n^\circ) = \sum_{n=1}^{N} -\frac{m\omega_N^2}{2}(x_n^\circ - x_{n-1}^\circ)^2$$

describing the beads as sitting on a degenerate set of parabolic barriers with displacements chosen to *just* balance the physical potential. The resulting (real) force on any individual bead x_n at $t = 0$ will therefore be

$$-V'(x_n^\circ) = -m\omega_N^2 \left(x_{n+1}^\circ - 2x_n^\circ + x_{n-1}^\circ\right) \tag{4.21}$$

Note that this force, like the hysteretic damping observed previously, will be minimized by symmetrically-displaced beads!

Now imagine another complete set of phase points $\{x_n\}$ that are collectively "close" to the $\{x_n^\circ\}$ in the sense that

$$x_n = x_n^\circ + \Delta_n$$

with $\{\Delta_n\}$ small enough displacements in the natural units of the system that

$$V(x_n) \approx V(x_n^\circ) + V'(x_n^\circ)\Delta_n + V''(x_n^\circ)\Delta_n^2 + \mathrm{O}(\Delta_n^3)$$

can be considered a reasonable approximation. Referring back to Equation 4.21, we see that the force on such neighboring points at $t = 0$ will be

$$-V'(x_n) \approx -V'(x_n^\circ) - 2m\omega_N^2\Delta_n$$

That is, the force may be written as a direct contribution from the physical potential, plus a linear contribution from the ring polymer. If we assume that the sampling method used to generate imaginary-time bead positions is good enough that we are always in the vicinity of a maximal ring-polymer configuration $\{x_n^\circ\}$, the equations of motion will *always* be of this type. To the extent that this is true — which I hope to investigate in the future — the RPMD equations of motion succeed inasmuch as they supply approximately the correct harmonic wobble.

4.10.6 Tantalizing hints but no clear success

Although we have successfully worked up a mathematical sweat, we have not arrived at an equation that is equivalent to RPMD. It is interesting to note, however, that we have obtained one member of a class of methods that perform the imaginary-time path integration and evaluation of $A_N(\mathbf{x})$ exactly, then evaluate a matrix element of the Heisenberg-picture time-evolved operator $B(t)$. Any means of handling the time-evolution could be put into action — from the classical approach given here to any of the family of IVR methods to convergent numerical propagation of a quantum wavepacket. All such approaches would yield exact statistics and approximate dynamics, like RPMD, but some could perform better for longer times (though almost certainly not at a lower computational cost).

4.11 Reverse-engineering RPMD — or something like it

The laborious — but conceptually straightforward — arguments just concluded provide some hints as to why RPMD might be a reasonable approximation to the real dynamics of the system. They do not, however, constitute a derivation, and the origin of the extended dynamics remains rather mysterious. Thus, we chose to make another attempt from a different point of view. Prof. Miller's logic retains its guiding influence, but we begin by *postulating* the dynamics we seek in the form of an appropriate set of delta functions. We then "work backwards" by inferring pairs of terms that could, through linearization, yield the appropriate results at each step of the derivation. This construction — or, in a poetically loose sense, reconstruction — is of merit insofar as the structural assumptions made in positing the delta functions are sensible.

4.11.1 A brief re-review of the linear approximation

Prof. Miller begins in his notes [168] with the "Boltzmannator" form of the time correlation function between local operators A and B,

$$C_{AB}(t) = \mathrm{Tr}\left[Ae^{-(\frac{\beta}{2}-\frac{it}{\hbar})H}Be^{-(\frac{\beta}{2}+\frac{it}{\hbar})H}\right] \tag{4.22}$$

Because we were able to write the Kubo-transformed correlation function in a similar form in Section 4.9, albeit with a thermalized, nonlocal version of B, we will attempt to work backwards toward an expression of this type. As such, we will briefly review the effect of linearization on Equation 4.22 so as to ground our inferences more clearly.

Applying the linear approximation to this expression yields

$$\begin{aligned} C_{AB}(t) &= \left(\frac{mN}{2\pi\hbar\sqrt{(\frac{\beta\hbar}{2})^2+t^2}}\right)^N \int_{-\infty}^{\infty} \mathrm{d}x_0 A(x_0) \int_{-\infty}^{\infty} \mathrm{d}x_N B(x_N) \left[\prod_{k=1}^{N-1} \int_{-\infty}^{\infty} \mathrm{d}\bar{x}_k \int_{-\infty}^{\infty} \mathrm{d}\Delta x_k\right] \\ &\times \exp\left\{-\frac{\beta m N}{2\left((\frac{\beta\hbar}{2})^2+t^2\right)} \sum_{k=1}^{N} (\bar{x}_k - \bar{x}_{k-1})^2 - \frac{\beta}{N}\left[\frac{V(x_0)+V(x_N)}{2} + \sum_{k=1}^{N-1} V(\bar{x}_k)\right]\right\} \\ &\times \exp\left\{-\frac{it}{\hbar N} \sum_{k=1}^{N} \Delta x_k \left[V'(\bar{x}_k) + \frac{mN^2}{(\frac{\beta\hbar}{2})^2+t^2}(\bar{x}_{k+1}+\bar{x}_{k-1}-2\bar{x}_k)\right]\right\} \end{aligned}$$

We apply the Fourier and delta-function identities as before, set $\Delta t = \frac{\sqrt{(\frac{\beta\hbar}{2})^2+t^2}}{N}$, and drop the overbars. In doing so, we obtain the product of delta functions

$$\left(\frac{2\pi\hbar N}{t}\right)^{N-1} \prod_{k=1}^{N-1} \delta\left[V'(x_k) + \frac{m}{\Delta t^2}(x_{k+1} - 2x_k + x_{k-1})\right]$$

which is equivalent to the now-familiar continuum-limit expression

$$\left(\frac{2\pi\hbar N}{t}\right)^{N-1} \prod_{k=1}^{N-1} \delta\left[V'(x(t_k)) + m\ddot{x}(t_k)\right]$$

4.11.2 The dynamical constraints

Recall that the extended Hamiltonian of RPMD is

$$H_N(\mathbf{p},\mathbf{x}) = \sum_{n=1}^{N} \frac{p_n^2}{2m} + \frac{m\omega_N^2}{2} \sum_{n=1}^{N} (x_n - x_{n-1})^2 + \sum_{n=1}^{N} V(x_n)$$

where N is the number of beads in the ring and $x_0 = x_N$. In casting the dynamics contained in this Hamiltonian as a set of delta functions, we must require that each bead in the ring move classically in response to the force from the external potential and its neighbors. For a given bead x_{sn}, where s is a time index and n labels different beads in the ring, the resulting delta function is

$$\delta\left[\frac{m}{\Delta t^2}(x_{s+1,n} - 2x_{sn} + x_{s-1,n}) + V'(x_{sn}) - m\omega_N^2(x_{s,n+1} - 2x_{sn} + x_{s,n-1})\right]$$

Before we proceed any further, we need to consider some niceties of indexing. As before, the largest value of s will be T, while the largest value of n will be N. In order to preserve the ring structure, we will require that $x_{s,0} = x_{s,N}$ for any value of s.

We must also consider the "edges" — those beads which mark the beginning and ending of the real-time trajectory. Since the ring structure is present at all times (i.e., over the entire range of s), there is some ambiguity as to where in the ring the operators A and B should be evaluated. Indeed, there is no reason a priori to find *any* choice of $A(x_{0,n_A})$ and $B(x_{T,n_B})$ objectionable. We must therefore assume that the operator expression we seek will correspond to an average over N^2 very similar terms arising from these choices. In practice, the actual number of terms to be manipulated could be reduced by collapsing those with the same value of the "interbead distance" $|n_A - n_B|$ into a single term multiplied by an appropriate degeneracy factor, determined by the size of the ring N and consistent with the invariance of our expressions under a cyclic relabeling. For the present purpose, we will not work with all of these terms generally; instead, we will look at the specific case where A and B are evaluated at $x_{0,N}$ and $x_{T,N}$, respectively. Such a limited treatment will allow us to obtain the basic form common to *all* of the N^2 terms. We can then make intuitive arguments as to what the general result should be.

We must take note of one final property of the edges: they are "determined," in the sense of being integrated over, *outside* of the scope of our constraints. That is, they represent specific points that appear only because of terminal matrix elements, and so (in this case) $\Delta x_{0,N} = \Delta x_{T,N} = 0$.

The result of all of these considerations is a set of delta functions,

$$\prod_{s=1}^{T-1}\prod_{n=1}^{N-1}\frac{1}{|C|}\delta\left[\frac{m}{\Delta t^2}(x_{s+1,n}-2x_{sn}+x_{s-1,n})+V'(x_{sn})-m\omega_N^2(x_{s,n+1}-2x_{sn}+x_{s,n-1})\right]$$

where C and Δt will be identified below.

We now determine the integrals from which these delta functions might have originated. We apply the Fourier identity, and then we insert $C = \frac{t}{2\pi\hbar T}$ and $\Delta t = \frac{\sqrt{\left(\frac{\beta\hbar}{2}\right)^2+t^2}}{T}$, as per Prof. Miller's work. After adding overbars, we obtain

$$\left[\prod_{s=1}^{T-1}\prod_{n=1}^{N-1}\int_{-\infty}^{\infty}\mathrm{d}\Delta x_{sn}\right]\exp\left\{-\frac{imtT}{\hbar\left((\frac{\beta\hbar}{2})^2+t^2\right)}\sum_{s=1}^{T-1}\sum_{n=1}^{N-1}(\bar{x}_{s+1,n}-2\bar{x}_{sn}+\bar{x}_{s-1,n})\Delta x_{sn}\right.$$
$$-\frac{it}{\hbar T}\sum_{s=1}^{T-1}\sum_{n=1}^{N-1}V'(\bar{x}_{sn})\Delta x_{sn}$$
$$\left.+\frac{imtN^2}{\beta^2\hbar^3T}\sum_{s=1}^{T-1}\sum_{n=1}^{N-1}(\bar{x}_{s,n+1}-2\bar{x}_{sn}+\bar{x}_{s,n-1})\Delta x_{sn}\right\}$$

We will refer to the terms in the exponential, hopefully transparently, as terms $\boxed{1}$, $\boxed{2}$, and $\boxed{3}$. Each of these terms may be associated with others that either depend only on the $\bar{x}_s$ or that are second order in the Δx_s; these "associated terms" must be inferred if we are to reconstruct a formula that can be useful in determining the operator expression corresponding to our dynamical constraints. We will call them $\boxed{1a}$, etc. The terms $\boxed{1}$ and $\boxed{1a}$, in turn, must eventually be rewritten as sums of other, more complicated terms. These original (or "parent") terms are labeled $\boxed{1o}$, etc.

4.11.3 Reconstructing $\boxed{1}$

Recall the useful identity

$$\sum_{s=1}^{T-1}(\bar{x}_{s+1,n} - 2\bar{x}_{sn} + \bar{x}_{s-1,n})\Delta x_{sn} = \sum_{s=1}^{T}(-1)(\bar{x}_{sn} - \bar{x}_{s-1,n})(\Delta x_{sn} - \Delta x_{s-1,n}) \tag{4.23}$$

This identity only holds strictly, however, when $\Delta x_{T,n} = 0$ for all values of n, which we have already postulated as true for $n = N$. This condition corresponds to requiring that the beads of the ring be positioned identically at t for each of the implied paths in Boltzmannator-type expressions. When applied to any given bead, this requirement simply implies that it is the bead on which B is evaluated; as applied to the whole set, its meaning (and the means by which it might be enforced) is somewhat more obscure. That said, we are attempting to hew as closely as possible to Prof. Miller's reasoning and so shall let the matter rest for the moment.

Applying the identity, we proceed to multiply and divide by 2 so as to make explicit the fact that $\boxed{1}$ should arise from a combination of terms from two different path integrals. We obtain

$$\boxed{1} = \frac{mT}{2\hbar}\frac{-it}{(\frac{\beta\hbar}{2})^2 + t^2}\sum_{s=1}^{T}\sum_{n=1}^{N-1}(-2)(\bar{x}_{sn} - \bar{x}_{s-1,n})(\Delta x_{sn} - \Delta x_{s-1,n})$$

By a kind of inverted completion of the square, we can infer that the terms associated with $\boxed{1}$ would be

$$\boxed{1a} = -\frac{mT}{2\hbar}\frac{(\frac{\beta\hbar}{2})}{(\frac{\beta\hbar}{2})^2 + t^2}\sum_{s=1}^{T}\sum_{n=1}^{N-1}\left[2(\bar{x}_{sn} - \bar{x}_{s-1,n})^2 + \frac{1}{2}(\Delta x_{sn} - \Delta x_{s-1,n})^2\right]$$

The parent terms of $\boxed{1}$ and $\boxed{1a}$ are, then,

$$-\frac{mT}{2\hbar}\frac{\frac{\beta\hbar}{2}-it}{(\frac{\beta\hbar}{2})^2+t^2}\sum_{s=1}^{T}\sum_{n=1}^{N-1}\Bigg[\ (\bar{x}_{sn}-\bar{x}_{s-1,n})^2+(\bar{x}_{sn}-\bar{x}_{s-1,n})(\Delta x_{sn}-\Delta x_{s-1,n}) \\ +\tfrac{1}{4}(\Delta x_{sn}-\Delta x_{s-1,n})^2\Bigg]$$

$$-\frac{mT}{2\hbar}\frac{\frac{\beta\hbar}{2}+it}{(\frac{\beta\hbar}{2})^2+t^2}\sum_{s=1}^{T}\sum_{n=1}^{N-1}\Bigg[\ (\bar{x}_{sn}-\bar{x}_{s-1,n})^2-(\bar{x}_{sn}-\bar{x}_{s-1,n})(\Delta x_{sn}-\Delta x_{s-1,n}) \\ +\tfrac{1}{4}(\Delta x_{sn}-\Delta x_{s-1,n})^2\Bigg]$$

Simplifying the constants and changing variables such that

$$x_{sn}=\bar{x}_{sn}+\frac{\Delta x_{sn}}{2}$$
$$x'_{sn}=\bar{x}_{sn}-\frac{\Delta x_{sn}}{2}$$

we thus obtain our "original term" leading to $\boxed{1}$,

$$\boxed{1o}=-\frac{mT}{2(\frac{\beta}{2}+\frac{it}{\hbar})\hbar^2}\sum_{s=1}^{T}\sum_{n=1}^{N-1}(x_{sn}-x_{s-1,n})^2-\frac{mT}{2(\frac{\beta}{2}-\frac{it}{\hbar})\hbar^2}\sum_{s=1}^{T}\sum_{n=1}^{N-1}(x'_{sn}-x'_{s-1,n})^2 \quad (4.24)$$

This is precisely the term from Prof. Miller's work which arises from the kinetic energy operator, albeit with an extra sum over n.

4.11.4 Reconstructing $\boxed{2}$

We now examine the potential term given by $\boxed{2}$. It can be rewritten as

$$\boxed{2}=-\frac{it}{\hbar T}\sum_{s=1}^{T-1}\sum_{n=1}^{N-1}2V'(\bar{x}_{sn})\frac{\Delta x_{sn}}{2}$$

This term would be the result of a first order expansion in Δx_{sn} of

$$\boxed{2}\approx-\frac{it}{\hbar T}\sum_{s=1}^{T-1}\sum_{n=1}^{N-1}\left[V(\bar{x}_{sn}+\frac{\Delta x_{sn}}{2})-V(\bar{x}_{sn}-\frac{\Delta x_{sn}}{2})\right]$$

The terms associated with the above would be

$$\boxed{2a}=-\frac{(\frac{\beta\hbar}{2})}{\hbar T}\Bigg[V(x_{0,N})+V(x_{T,N})+\sum_{s=0}^{T}\sum_{n=1}^{N-1}V(\bar{x}_{sn}+\frac{\Delta x_{sn}}{2}) \\ +\sum_{s=0}^{T}\sum_{n=1}^{N-1}V(\bar{x}_{sn}-\frac{\Delta x_{sn}}{2})\Bigg]$$

Applying our change of variables, we obtain the parent term

$$\boxed{2o} = -\frac{\frac{\beta}{2}+\frac{it}{\hbar}}{T}\left[\frac{V(x_{0,N})}{2}+\frac{V(x_{T,N})}{2}+\sum_{s=0}^{T}\sum_{n=1}^{N-1}V(x_{sn})\right] \\ -\frac{\frac{\beta}{2}-\frac{it}{\hbar}}{T}\left[\frac{V(x_{0,N})}{2}+\frac{V(x_{T,N})}{2}+\sum_{s=0}^{T}\sum_{n=1}^{N-1}V(x'_{sn})\right] \tag{4.25}$$

Just as $\boxed{1o}$ can be associated with the path integral expressions for the kinetic energy operator, $\boxed{2o}$ can be associated with the potential energy operator for each path integral, only with extra sums over n.

4.11.5 Reconstructing $\boxed{3}$

Finally, we examine $\boxed{3}$, which has no antecedent in Prof. Miller's work. Its form, however, suggests that we should rewrite it in a similar way as we did $\boxed{1}$. Since we suppose that $\bar{x}_{s,0}$ and $\bar{x}_{s,N}$ refer to the same beads, we can apply an identity very similar to Equation 4.23:

$$-\sum_{n=1}^{N-1}(\bar{x}_{s,n+1}-2\bar{x}_{sn}+\bar{x}_{s,n-1})\Delta x_{sn} = -\sum_{n=1}^{N}(\bar{x}_{sn}-\bar{x}_{s,n-1})(\Delta x_{sn}-\Delta x_{s,n-1})$$

A similar condition holds here as did with respect to Equation 4.23: It is only rigorously true when $\Delta x_{s,N}=0$ for all values of s.

After applying the identity and multiplying and dividing the result by 2, we obtain

$$\boxed{3} = -\frac{imtN^2}{2\beta^2\hbar^3T}\sum_{s=1}^{T-1}\sum_{n=1}^{N}2(\bar{x}_{sn}-\bar{x}_{s,n-1})(\Delta x_{sn}-\Delta x_{s,n-1})$$

If we follow reasoning similar to that used in reconstructing $\boxed{1}$, we see immediately that $\boxed{3}$ should come from

$$\boxed{3o} = -\frac{imtN^2}{2\beta^2\hbar^3T}\sum_{s=1}^{T-1}\sum_{n=1}^{N}(x_{sn}-x_{s,n-1})^2+\frac{imtN^2}{2\beta^2\hbar^3T}\sum_{s=1}^{T-1}\sum_{n=1}^{N}(x'_{sn}-x'_{s,n-1})^2$$

After rearranging the constant prefactors, we arrive at a rather suggestive expression:

$$\boxed{3o} = -\frac{(\frac{it}{\hbar})/T}{\beta/N}\frac{mN}{2\beta\hbar^2}\sum_{s=1}^{T-1}\sum_{n=1}^{N}(x_{sn}-x_{s,n-1})^2+\frac{(\frac{it}{\hbar})/T}{\beta/N}\frac{mN}{2\beta\hbar^2}\sum_{s=1}^{T-1}\sum_{n=1}^{N}(x'_{sn}-x'_{s,n-1})^2 \tag{4.26}$$

Each piece of Equation 4.26 is strikingly similar to the path integral for the Boltzmann operator in the case of a free particle (albeit with an extra sum over s). More interesting is the complex prefactor we have separated out — it has the flavor of a unit conversion from imaginary-time path integration with N beads to real-time path integration with T beads.

4.11.6 The "original" expression

Combining Equations 4.24, 4.25, and 4.26 and adding integrals over the operators evaluated at our chosen edge terms, we obtain the expression

$$
\begin{aligned}
&C\int_{-\infty}^{\infty}\mathrm{d}x_{0,N}A(x_{0,N})\int_{-\infty}^{\infty}\mathrm{d}x_{T,N}B(x_{T,N})\left[\prod_{s=0}^{T}\prod_{n=1}^{N}\int_{-\infty}^{\infty}\mathrm{d}x_{sn}\int_{-\infty}^{\infty}\mathrm{d}x'_{sn}\right]\\
&\times\exp\Bigg\{-\frac{mT}{2(\frac{\beta}{2}+\frac{it}{\hbar})\hbar^2}\sum_{s=1}^{T}\sum_{n=1}^{N-1}(x_{sn}-x_{s-1,n})^2-\frac{(\frac{it}{\hbar})/T}{\beta/N}\frac{mN}{2\beta\hbar^2}\sum_{s=1}^{T-1}\sum_{n=1}^{N}(x_{sn}-x_{s,n-1})^2\\
&\quad-\frac{mT}{2(\frac{\beta}{2}-\frac{it}{\hbar})\hbar^2}\sum_{s=1}^{T}\sum_{n=1}^{N-1}(x'_{sn}-x'_{s-1,n})^2+\frac{(\frac{it}{\hbar})/T}{\beta/N}\frac{mN}{2\beta\hbar^2}\sum_{s=1}^{T-1}\sum_{n=1}^{N}(x'_{sn}-x'_{s,n-1})^2\\
&\quad-\frac{\frac{\beta}{2}+\frac{it}{\hbar}}{T}\left[\frac{V(x_{0,N})+V(x_{T,N})}{2}+\sum_{s=0}^{T}\sum_{n=1}^{N-1}V(x_{sn})\right]\\
&\quad-\frac{\frac{\beta}{2}-\frac{it}{\hbar}}{T}\left[\frac{V(x_{0,N})+V(x_{T,N})}{2}+\sum_{s=0}^{T}\sum_{n=1}^{N-1}V(x'_{sn})\right]\Bigg\}
\end{aligned}
\tag{4.27}
$$

where C is an elaborate, undetermined constant.

Our particular choice of the beads on which we evaluate A and B will only affect the potential terms in Equation 4.27 — the bead couplings are indifferent to this choice. Therefore, our general result for the "original" expression would be

$$
\begin{aligned}
&C\left[\prod_{s=0}^{T}\prod_{n=1}^{N}\int_{-\infty}^{\infty}\mathrm{d}x_{sn}\int_{-\infty}^{\infty}\mathrm{d}x'_{sn}\right]\left[\sum_{n_A=1}^{N}\frac{A(x_{0,n_A})}{N}\right]\left[\sum_{n_B=1}^{N}\frac{B(x_{T,n_B})}{N}\right]\\
&\times\exp\Bigg\{-\frac{mT}{2(\frac{\beta}{2}+\frac{it}{\hbar})\hbar^2}\sum_{s=1}^{T}\sum_{n=1}^{N-1}(x_{sn}-x_{s-1,n})^2-\frac{(\frac{it}{\hbar})/T}{\beta/N}\frac{mN}{2\beta\hbar^2}\sum_{s=1}^{T-1}\sum_{n=1}^{N}(x_{sn}-x_{s,n-1})^2\\
&\quad-\frac{mT}{2(\frac{\beta}{2}-\frac{it}{\hbar})\hbar^2}\sum_{s=1}^{T}\sum_{n=1}^{N-1}(x'_{sn}-x'_{s-1,n})^2+\frac{(\frac{it}{\hbar})/T}{\beta/N}\frac{mN}{2\beta\hbar^2}\sum_{s=1}^{T-1}\sum_{n=1}^{N}(x'_{sn}-x'_{s,n-1})^2\\
&\quad-\frac{\frac{\beta}{2}+\frac{it}{\hbar}}{T}\left[\frac{V(x_{0,N})+V(x_{T,N})}{2}+\sum_{s=0}^{T}\sum_{n=1}^{N-1}V(x_{sn})\right]\\
&\quad-\frac{\frac{\beta}{2}-\frac{it}{\hbar}}{T}\left[\frac{V(x_{0,N})+V(x_{T,N})}{2}+\sum_{s=0}^{T}\sum_{n=1}^{N-1}V(x'_{sn})\right]\Bigg\}
\end{aligned}
\tag{4.28}
$$

where the primed sums indicate that we have excluded $n=n_A$ and $n=n_B$ for $s=0$ and $s=T$, respectively. Note that we have recovered the bead-averaged expressions for A and

B that appear in Equation 4.12.

In the special case that $N = 1$, we obtain from both Equation 4.27 and Equation 4.28

$$C \int_{-\infty}^{\infty} \mathrm{d}x_{0,1} A(x_{0,1}) \int_{-\infty}^{\infty} \mathrm{d}x_{T,1} B(x_{T,1}) \left[\prod_{s=1}^{T-1} \int_{-\infty}^{\infty} \mathrm{d}x_{s,1} \int_{-\infty}^{\infty} \mathrm{d}x'_{s,1} \right]$$
$$\times \exp \left\{ -\frac{mT}{2(\frac{\beta}{2} + \frac{it}{\hbar})\hbar^2} \sum_{s=1}^{T} (x_{s,1} - x_{s-1,1})^2 - \frac{\frac{\beta}{2} + \frac{it}{\hbar}}{T} \left[\frac{V(x_{0,1})}{2} + \frac{V(x_{T,1})}{2} + \sum_{s=1}^{T-1} V(x_{s,1}) \right] \right.$$
$$\left. -\frac{mT}{2(\frac{\beta}{2} - \frac{it}{\hbar})\hbar^2} \sum_{s=1}^{T} (x'_{s,1} - x'_{s-1,1})^2 - \frac{\frac{\beta}{2} - \frac{it}{\hbar}}{T} \left[\frac{V(x_{0,1})}{2} + \frac{V(x_{T,1})}{2} + \sum_{s=1}^{T-1} V(x'_{s,1}) \right] \right\}$$

where the other two terms disappear altogether because $x_{s,0} = x_{s,1}$ and $x'_{s,0} = x'_{s,1}$ for our ring. If we now drop the 1 associated with the index n from the names of our beads, we recover the path integral expression for Equation 4.22. In other words, our expression has the Boltzmannator as a special case, as must be true of any such result if it is to correspond to the Kubo-transformed time correlation function.

4.11.7 Final thoughts on reverse-engineering

In this context, our next "reverse-engineering" task is clear: we must find an operator expression that, when written as a path integral, will yield at least the basic *form* of the preceding results. Unfortunately, years of intermittent work seem to indicate that any such discovery will be lucky rather than reasoned. Were I successful in that regard, and if the consequences of our somewhat flippant treatment of the edge terms in these expressions were not too serious, we could attempt once again to linearize "forward" from scratch as in Section 4.10. Then we might obtain RPMD by way of a complete, controlled set of approximations to an exact quantum-mechanical expression. But having found only the middle of a derivation — but neither its beginning nor its end, and perhaps not even one of RPMD (or indeed of any physically-justified method at all) — we must conclude in a degree of thoughtful confusion. Put more elegantly [173]: "Whereof one cannot speak, thereof one must be silent."

4.12 Concluding remarks and future work

The single clear means of proceeding with the present work is to investigate the extent to which any given ring-polymer configuration $\{x_n\}$ can be said to fall in the vicinity of another configuration, $\{x_n^\circ\}$, that maximize the exponential. The harmonic oscillator, as usual, provides an attractive test case; Equation(s) 4.21 will correspond to a relatively simple matrix equation. Based on how thickly the family of solutions fills configurational

space, we can determine the maximum displacement Δ_n allowed for any given bead — and perhaps rewrite it in terms of the $\{x_n^\circ\}$, recovering RPMD in the process. Such a derivation of RPMD would apply only for a special case, but it would be a new and significant discovery.

Even if the strategy outlined above fails, I remain sanguine regarding the possibility of constructing a true derivation of RPMD, as opposed to the justified heuristic that prevails today. Of course, it may be that RPMD cannot be derived from *any* exact quantum mechanical expression — that it is merely an error-ridden version of PA-CMD. Not every avenue has been exhausted, however: The way forward may lie in a clever continuation of (or flash of insight related to) the work presented here; in a similar effort based on close study of the derivation of CMD and PA-CMD [18, 19, 145, 146]; in pursuing the known connections between RPMD and partially-adiabatic CMD [144,146] or the semiclassical instanton [167]; or in some entirely new direction. Until such time as these issues are settled, the method remains attractive, and examples of its use will likely continue to proliferate in the literature.

Appendix A

Nitrogen potential details

A.1 Introduction

This appendix contains the details of the multi-Gaussian potentials fitted for the nitrogen ground- and excited-state potential energy curves using the Levenberg-Marquardt algorithm (as implemented in GNUPLOT) [174, 175]. Fitting parameters are provided, as are sets of convergent DVR parameters $\{V_c, R_{\max}, \Delta R\}$ for each potential used, including the empirical curves of Le Roy et al. [110] and Chen et al. [109].

A.2 DFT potential fits

Fits were made to the functional form $V(R) = \sum_i a_i e^{-(\frac{R-c_i}{b_i})^2}$ as follows:

1. The electronic structure energies were shifted such that the minimum value was 0 eV.
2. The dissociation energy was then estimated as the value of the electronic structure energy at the largest bond length R for which the calculation converged. Since we intended to set our DVR cut-off energy V_c to this value, we removed points of higher energy from our data set.
3. An initial fit was then made by pruning the data further to a set of points nearly evenly-spaced by 0.1 Å (0.05 Å within the well), leaving 29 points for the ground-state curve (supporting a 9-Gaussian fit) and 30 points for the excited-state curve (supporting a 10-Gaussian fit). 2 additional points were pruned from the ground-state data set after it became apparent that a sensible fit could not be obtained with them included.
4. On convergence of the initial fit, the data set was expanded to include all of the points in the appropriate range of R (0.8–3.4 Å for the ground- and 0.9–4.7 Å for the excited-state curve). The parameters were then refitted.

i	$a_{g,i}$ (eV)	$b_{g,i}$ (Å)	$c_{g,i}$ (Å)	$a_{x,i}$ (eV)	$b_{x,i}$ (Å)	$c_{x,i}$ (Å)
1	3.99227	0.448362	2.17059	52.6443	23.4511	−27.0623
2	4.17561	1.91477	5.03801	53.7108	22.6556	−26.4455
3	−13.8231	0.17553	1.00897	−50.0349	0.482631	0.706272
4	3.88524	1.98647	5.17503	46.6704	28.2633	−28.9929
5	13.3891	0.237845	0.784391	110.939	1.32179	0.354615
6	3.41079	0.124627	0.989159	−58.9109	1.99613	2.98965
7	4.43654	0.420372	1.76726	78.0797	17.3901	−19.9908
8	5.57452	0.684556	3.05852	−198.775	1.04387	0.895781
9	4.00177	0.802511	3.75273	111.008	1.3218	0.354599
10	3.90151	1.96757	5.13467	32.0054	41.9304	−24.2696
11	4.1697	1.87942	4.98608	−1.54601	0.335931	2.49871
12	0.50247	0.216967	1.54366	0.239951	0.165158	1.60621
13	6.44803	0.147052	1.06541	−2.94681	0.371195	2.14623
14	5.16339	0.555829	2.54725	2.57876	0.443997	3.24694

Table A.1: Parameters $\{a_i, b_i, c_i\}$ for the multi-Gaussian DFT potential fits. Subscripts g and x denote the ground- and excited-state fits, respectively.

5. The qualitative behavior of the refitted curve was examined, and additional Gaussians were placed where it was of low quality. 14 Gaussians were eventually used for each state; the converged parameters are listed in Table A.1.

6. An overall shift was then applied to each curve such that the well-to-well energy difference matched that from the electronic structure calculations, $V_e = 402.0419551$ eV, with the minimum energy for the ground state set to zero. The ground-state shift was -0.000634973 eV, while the excited-state shift was 402.0429938584 eV.

A.3 Excited-state Morse parameters

Rather than a potential, Chen et al. report spectroscopic constants for the excited state accessed in the X-ray absorption [109], which constants are obtained by fitting to experiment. In particular, they report vibrational frequency $\omega_e = 235.2(5)$ eV, anharmonicity $\omega_e x_e = 1.9(5)$ eV, and equilibrium position $R_e = 1.164(1)$ Å, where the parentheses indicate uncertainty in the last digit.

These quantities may be used to determine parameters for a Morse potential with min-

imum V_e, $V_{\text{Morse}}(R) = V_e + D_e(1 - e^{-\alpha(R-R_e)})^2$, as follows [176]:

$$D_e = \frac{\omega_e^2}{4\omega_e x_e}$$

$$\alpha = \sqrt{\frac{8\pi^2 c\mu\omega_e x_e}{\hbar}}$$

where energies have been expressed in wavenumbers. The parameters thus determined are $D_e = 7.279$ eV and $\alpha = 2524$ Å^{-1}. (R_e may be used as reported.)

A.4 Convergent DVR parameters

For each of our fitted potentials, as well as the potentials due to Le Roy et al. [110] and Chen et al. [109], we found the convergent set of Colbert-Miller DVR parameters $\{V_c, R_{\text{max}}, \Delta R\}$ using the following procedure:

1. V_c was set to the best estimate of the dissociation energy (i.e., the asymptotic value of R) in order to capture as many physically-relevant states as possible. For the ground-state fit, we set V_c (and incorporated an explicit lowest-allowed value of R, 0.9 Å) such that no points would be placed outside of the fitting region.

2. R_{max} was set large enough to allow for as much leakage of wavefunction amplitude as required.

3. ΔR was then reduced from 0.5 Å until convergence was observed in the energies of the vibrational states, the canonical averages of the kinetic and potential energies, the canonical averages of position and momentum, and the associated uncertainties.

4. Convergence was tested by varying R_{max} and V_c. In order to obtain more accurate wavefunctions, working values of ΔR were chosen to be roughly 3 times smaller. The resulting convergent DVR parameters are listed in Table A.2.

5. Results for the empirical potentials were then double-checked. Specifically, energies for the $\text{MLR}_4(6, 8)$ potential were tested against the Dunham expansion given by Le Roy et al. [110], while the excited-state Morse energies were compared with the exact values where possible ($J = 0$) [176]. For $J \neq 0$, analytical values based on a small-vibrational-amplitude Pekeris approximation to the centrifugal barrier were used [177, 178]. Agreement was exemplary.

Potential	g/x	V_c (eV)	$R_{\max}$ (Å)	ΔR (Å)
$V_g(R)$	g	10.71369	1.5	0.003
$V_x(R)$	x	413.5795072	3.5	0.0125
MLR_4(6,8) [110]	g	9.899517695	3.5	0.0125
Exp'tal Morse [109]	x	7.279	3.0	0.01

Table A.2: Convergent parameters for use with the Colbert-Miller DVR. The column labeled "g/x" indicates whether the potential is for the ground or excited state.

Appendix B

The Voigt lineshape

B.1 Basics of the Voigt lineshape

The (centered, normalized) Voigt lineshape is defined as the convolution of a Gaussian and a Lorentzian centered around 0 [179],

$$V(x;\sigma,\gamma) = \int_{-\infty}^{\infty} \mathrm{d}x'\, G(x;\sigma) L(x-x';\gamma)$$

where we have used the normalized forms

$$G(x;\sigma) = \frac{1}{\sqrt{2\pi}\sigma} e^{-\frac{x^2}{2\sigma^2}}$$
$$L(x;\gamma) = \frac{1}{\pi}\frac{\gamma}{x^2+\gamma^2}$$

This profile may be understood, for our purposes, to reflect simultaneous broadening of a theoretical "stick" line in a given spectrum by state lifetimes (the Lorentzian) and instrument error (the Gaussian). In the absence of either broadening source — e.g., if $\sigma \to 0$ ($\gamma \to 0$) — the Voigt lineshape will reduce to the underlying Lorentzian (Gaussian).

As may be shown using the properties of the error function and any convenient table of integrals (or computational algebra software such as MATHEMATICA), the Voigt lineshape can be evaluated directly in terms of the complex error function

$$w(z) = e^{-z^2}\mathrm{erfc}\,(-iz) = e^{-z^2}\left[1 - \mathrm{erf}(-iz)\right]$$

via the expression

$$V(x;\sigma,\gamma) = \frac{1}{\sqrt{2\pi}\sigma}\mathrm{Re}\left[w\left(\frac{x+i\gamma}{\sqrt{2}\sigma}\right)\right] \tag{B.1}$$

B.2 The full width at half-maximum

The full width at half-maximum (FWHM) of the Voigt profile is given by the distance $\alpha_V = |x_+ - x_-|$ between the two points $x_\pm$ that, for a given choice of $\{\sigma, \gamma\}$, yield

$$\frac{V(x_\pm; \sigma, \gamma)}{V(0; \sigma, \gamma)} = \frac{1}{2}$$

Unfortunately, α_V is not available in closed form. It may instead be written in terms of the Gaussian and Lorentzian widths as

$$\alpha_V \approx \frac{1}{2}\left(1.0692\alpha_L + \sqrt{0.86639\alpha_L^2 + \alpha_G^2}\right) \tag{B.2}$$

with a maximum error in the approximation of 0.02% [180]. Simple algebra shows that the component widths are

$$\alpha_G = 2\sqrt{2\ln 2}\sigma$$
$$\alpha_L = 2\gamma$$

which expressions provide us with a complete correspondence between our broadening scheme (based on $\{\sigma, \gamma\}$) and that of experimentalists (based on $\{\alpha_G, \alpha_L\}$).

B.3 An approximate form

In our work, we have used the exact expression given in Equation B.1; the only modification is a shift of the center from $x = 0$ to an arbitrary point x_0. It is more common in the literature, however, to use the (unnormalized) approximate form

$$V(x; \eta, \Gamma) = \eta \frac{\frac{\Gamma}{2}^2}{(x - x_0)^2 + \frac{\Gamma}{2}^2} + (1 - \eta)\exp\left[-\frac{(x - x_0)^2}{2\left(\frac{\Gamma}{c}\right)^2}\right]$$

where Γ is a width parameter, $\eta \in [0, 1]$ and $1 - \eta$ are the Lorentzian and Gaussian fractions in the mixture, and $c = \frac{2}{\sqrt{\ln 2}}$ [52, 181]. The error in this approximation is 0.77% at the maximum (and smaller elsewhere) for the worst case encountered, where $\alpha_G = \alpha_L$ [181].

The procedure used in a Voigt-broadening analysis of an experimental absorption edge begins by assuming global values of η and Γ — namely, that each peak originates from the same state and is broadened equally by instrument error. These values and a (possibly variably-sized) set of peak locations $\{x_i\}$ are then used in a nonlinear least-squares fit of the data [174]. The key result is an approximate Voigt width, $\alpha_V \approx \Gamma$; component widths may be determined by using the graphs in Reference [181], which relate the Gaussian fraction $1 - \eta$ to α_G and $\frac{\Gamma}{\alpha_G}$ to α_L, or by applying an expression such as Equation B.2.

B.4 Implementation of the complex error function

I was unable to find a standalone implementation of the complex error function written in plain C code. The closest available routine was the CERN MATHLIB function CWERF [182], which is written in FORTRAN and implements the algorithm of Gautschi with modifications due to Kölbig [183, 184]. Since it remains unclear to me how to combine the native treatment of complex numbers in FORTRAN with the lack of any such support in C code, I opted not to write a wrapper function. I instead ported the MATHLIB routine directly and checked the results against the values of $w(z)$ given in Table 7.9 of Abramowitz & Stegun [185]. The header file, function, and test routine for my implementation are given below for free use and adaptation by the community; they are also available in digital form by inquiring with me at `gkl@alum.mit.edu`.

B.4.1 The header: `cerf.h`

```
/* This header, cerf.h, contains inclusions, definitions, function
 * prototypes, and variable declarations for the cerf function, which
 * computes the real and imaginary parts of the complex error function
 * for an arbitrary complex argument. */

#include <math.h>      /* Include standard math libraries. */
#include <stdio.h>     /* Include standard I/O libraries. */


#define C1 7.4         /* Necessary constants. */
#define C2 8.3
#define C3 0.3125
#define C4 1.6

#define C 1.12837916709551257


void cerf(double,double);     /* The function declaration. */


double p;       /* A constant to be used often, p = (2*C4)**33.
                 * Initialize it separately. */
double rew,imw; /* The real and imaginary parts of w(z). */
```

B.4.2 The function: `cerf.c`

```
/* This function, cerf.c, is a C port of the CERN MATHLIB complex
 * error function routine written by K.S. Koelbig after an algorithm
 * by Walter Gautschi. It differs from the MATHLIBG function primarily
 * in that it takes as arguments the real and imaginary part of z; in
 * the original FORTRAN code, native complex number handling was used. */

#include "cerf.h"     /* Include the cerf header. */


void cerf(double rez, double imz) {

  int n;                /* A dummy counter for use in loops. */
  double redum,imdum;   /* Dummy variables for use in complex
                         * products. */

  double mrez,mimz;     /* The modulus of re(z) and im(z). */

  /* Intermediates. */
  double rezh,imzh;
  double rer[38],imr[38];
  double ret,imt;
  double xl;
  double res,ims;


  mrez=fabs(rez);
  mimz=fabs(imz);

  if ((mimz<C1)&&(mrez<C2)) {

    rezh=mimz+C4;
    imzh=mrez;

    for (n=1;n<=37;n++) {

      rer[n]=0;
      imr[n]=0;

    }
```

```
  for (n=36;n>=1;n--) {

    ret=rezh+n*rer[n+1];
    imt=imzh-n*imr[n+1];

    rer[n]=0.5*ret/(ret*ret+imt*imt);
    imr[n]=0.5*imt/(ret*ret+imt*imt);

  }

  xl=p;
  res=0;
  ims=0;

  for (n=33;n>=1;n--) {

    xl*=C3;
    res+=xl;

    redum=res;
    imdum=ims;
    res=rer[n]*redum-imr[n]*imdum;
    ims=rer[n]*imdum+imr[n]*redum;

  }

  rew=C*res;
  imw=C*ims;

}
else {

  rezh=mimz;
  imzh=mrez;

  rer[1]=0;
  imr[1]=0;
```

```
    for (n=9;n>=1;n--) {

      ret=rezh+n*rer[1];
      imt=imzh-n*imr[1];

      rer[1]=0.5*ret/(ret*ret+imt*imt);
      imr[1]=0.5*imt/(ret*ret+imt*imt);

    }

    rew=C*rer[1];
    imw=C*imr[1];

  }

  if (mimz==0) rew=exp(-mrez*mrez);

  if (imz<0) {

    redum=rew;
    imdum=imw;

    rew=2*exp(mimz*mimz-mrez*mrez)*cos(2*mimz*mrez)-redum;
    imw=-2*exp(mimz*mimz-mrez*mrez)*sin(2*mimz*mrez)-imdum;

    if (rez>0) imw*=-1;

  }
  else {

    if (rez<0) imw*=-1;

  }

}
```

B.4.3 The test routine: test_cerf.c

```
/* This function, test_cerf, prints out the value of the complex error
 * function for a range of data reflecting that tabulated in Chapter 7
 * of Abramowitz & Stegun. */

#include "cerf.h"     /* Include the cerf header. */


int main() {

  int n;          /* A dummy counter for use in loops. */
  double x,y;     /* The real and imaginary parts of z. */

  /* First initialize p. */
  p=2*C4;
  for (n=1;n<=32;n++) p*=2*C4;

  /* Now perform the test. */
  for (x=0;x<4.0;x+=0.1) {

    for (y=0;y<=3.0;y+=0.1) {

      cerf(x,y);

      printf("%.2g %.2g %.6g %.6g\n",x,y,rew,imw);

    }

  }

}
```

Bibliography

[1] P. A. M. Dirac, Proc. R. Soc. Lond. A **123**, 714 (1929).

[2] P. Pyykkö, Chem. Rev. **88**, 563 (1988).

[3] D. J. Gorin and F. D. Toste, Nature **446**, 395 (2007).

[4] W. Vanroose, F. Martin, T. N. Rescigno, and C. W. McCurdy, Science **310**, 1787 (2005).

[5] M. Born and R. [*sic*] Oppenheimer, Ann. Phys. (Leipzig) **84**, 457 (1927).

[6] M. Born and J. R. Oppenheimer, On the Quantum Theory of Molecules, translated by S. M. Blinder and with emendations by B. Sutcliffe and W. Geppert, `http://www.ulb.ac.be/cpm/people/scientists/bsutclif/bornop.pdf`, (Online; accessed 14$^{\text{th}}$ July, 2010).

[7] A. Szabo and N. S. Ostlund, *Modern Quantum Chemistry: Introduction to Advanced Electronic Structure Theory*, Dover Publications, Inc., New York, revised and corrected edition, 1996.

[8] P. Hohenberg and W. Kohn, Phys. Rev. **136**, B864 (1964).

[9] W. Kohn and L. J. Sham, Phys. Rev. **140**, A1133 (1965).

[10] C. Eckart, Phys. Rev. **46**, 383 (1935).

[11] E. B. Wilson, Jr., J. C. Decius, and P. C. Cross, *Molecular Vibrations: The Theory of Infrared and Raman Vibrational Spectra*, Dover Publications, Inc., New York, corrected edition, 1980.

[12] J. C. Tully, Nonadiabatic Processes in Molecular Collisions, in *Dynamics of Molecular Collisions, Part B*, edited by W. H. Miller, chapter 5, page 217, Plenum Press, New York, 1976.

[13] J. R. Taylor, *Scattering Theory: The Quantum Theory of Nonrelativistic Collisions*, Dover Publications, Inc., New York, revised edition, 2006.

[14] B. J. Berne and D. Thirumalai, Annu. Rev. Phys. Chem. **37**, 401 (1986).

[15] W. H. Miller, Adv. Chem. Phys. **25**, 69 (1974).

[16] W. H. Miller, J. Phys. Chem. A **105**, 2942 (2001).

[17] I. R. Craig and D. E. Manolopoulos, J. Chem. Phys. **121**, 3368 (2004).

[18] S. Jang and G. A. Voth, J. Chem. Phys. **111**, 2357 (1999).

[19] S. Jang and G. A. Voth, J. Chem. Phys. **111**, 2371 (1999).

[20] J. Gao, Methods and Applications of Combined Quantum Mechanical and Molecular Mechanical Potentials, in *Reviews in Computational Chemistry*, edited by K. B. Lipkowitz and D. B. Boyd, volume 7, page 119, VCH Publishers, New York, 1995.

[21] D. A. Case et al., AMBER 9, 2006.

[22] D. Chandler, *Introduction to Modern Statistical Mechanics*, Oxford University Press, New York, 1987.

[23] D. Frenkel and B. Smit, *Understanding Molecular Simulation: From Algorithms to Applications*, volume 1st of *Computational Science: From Theory to Applications*, Academic Press, San Diego, CA, 2nd edition, 2002.

[24] A. Chandra, M. E. Tuckerman, and D. Marx, Phys. Rev. Lett. **99**, 145901 (2007).

[25] D. Asthagiri, L. R. Pratt, J. D. Kress, and M. A. Gomez, Proc. Natl. Acad. Sci. USA **101**, 7229 (2004).

[26] M. E. Tuckerman, D. Marx, and M. Parrinello, Nature **417**, 925 (2002).

[27] M. E. Tuckerman, A. Chandra, and D. Marx, Acc. Chem. Res. **39**, 151 (2006).

[28] E. F. Aziz, N. Ottosson, M. Faubel, I. V. Hertel, and B. Winter, Nature **455**, 89 (2008).

[29] P. Auger, J. Phys. (Paris) **6**, 205 (1925).

[30] H. Ågren, A. Cesar, and C. M. Liegener, Adv. Quantum Chem. **23**, 1 (1992).

[31] L. S. Cederbaum, J. Zobeley, and F. Tarantelli, Phys. Rev. Lett. **79**, 4778 (1997).

[32] S. Scheit, V. Averbukh, H.-D. Meyer, J. Zobeley, and L. S. Cederbaum, J. Chem. Phys. **124**, 154305 (2006).

[33] K. Gokhberg, V. Averbukh, and L. S. Cederbaum, J. Chem. Phys. **124**, 144315 (2006).

[34] P. V. Demekhin et al., J. Chem. Phys. **131**, 104303 (2009).

[35] V. Averbukh, I. B. Müller, and L. S. Cederbaum, Phys. Rev. Lett. **93**, 263002 (2004).

[36] T. Jahnke et al., Nat. Phys. **6**, 74 (2010).

[37] M. Mucke et al., Nat. Phys. **6**, 78 (2010).

[38] D. Prendergast and G. Galli, Phys. Rev. Lett. **96**, 215502 (2006).

[39] B. Hetényi, F. D. Angelis, P. Giannozzi, and R. Car, J. Chem. Phys. **120**, 8632 (2004).

[40] P. Wernet et al., Science **304**, 995 (2004).

[41] J. S. Uejio, C. P. Schwartz, R. J. Saykally, and D. Prendergast, Chem. Phys. Lett. **467**, 195 (2008).

[42] C. P. Schwartz, J. S. Uejio, R. J. Saykally, and D. Prendergast, J. Chem. Phys. **130**, 184109 (2009).

[43] J. J. Sakurai, *Modern Quantum Mechanics*, Addison-Wesley Publishing Company, Inc., New York, revised edition, 1994.

[44] G. D. Mahan, *Many Particle Physics*, Physics of Solids and Liquids, Kluwer Academic Publishers, New York, 3rd edition, 2000.

[45] J. P. Perdew, K. Burke, and M. Ernzerhof, Phys. Rev. Lett. **77**, 3865 (1996).

[46] J. P. Perdew, K. Burke, and M. Ernzerhof, Phys. Rev. Lett. **78**, 1396 (1997).

[47] P. Giannozzi et al., J. Phys. Condens. Matter **21**, 395502 (2009).

[48] E. L. Shirley, Phys. Rev. B **54**, 16464 (1996).

[49] S.-D. Mo and W. Y. Ching, Phys. Rev. B **62**, 7901 (2000).

[50] P. E. Blöchl, Phys. Rev. B **50**, 17953 (1994).

[51] A. Nilsson and L. G. Pettersson, Surf. Sci. Rep. **55**, 49 (2004).

[52] J. Stöhr, *NEXAFS Spectroscopy*, volume 25 of *Springer Series in Surface Sciences*, Springer, Heidelberg, 1992.

[53] J. J. Rehr et al., C. R. Phys. **10**, 548 (2009).

[54] V. Carravetta, O. Plashkevych, and H. Ågren, Chem. Phys. **263**, 231 (2001).

[55] U. Ekström, P. Norman, V. Carravetta, and H. Ågren, Phys. Rev. Lett. **97**, 143001 (2006).

[56] J. J. Rehr, J. A. Soininen, and E. L. Shirley, Physica Scripta **T115**, 207 (2005).

[57] S. Fatehi, C. P. Schwartz, R. J. Saykally, and D. Prendergast, J. Chem. Phys. **132**, 094302 (2010).

[58] J. VandeVondele and M. Sprik, Phys. Chem. Chem. Phys. **7**, 1363 (2005).

[59] A. D. Becke, J. Chem. Phys. **98**, 5648 (1993).

[60] C. Lee, W. Yang, and R. G. Parr, Phys. Rev. B **37**, 785 (1988).

[61] P. J. Stephens, F. J. Devlin, C. F. Chabalowski, and M. J. Frisch, J. Phys. Chem. **98**, 11623 (1994).

[62] W. Pokapanich et al., Phys. Rev. Lett. **96**, 215502 (2006).

[63] T. Kashiwakura et al., J. Electron. Spectrosc. Relat. Phenom. **79**, 207 (1996).

[64] C. P. Schwartz, unpublished work, May 2010.

[65] C. D. Cappa, J. D. Smith, B. M. Messer, R. C. Cohen, and R. J. Saykally, J. Phys. Chem. A **111**, 4776 (2007).

[66] A. Botti, F. Bruni, S. Imberti, M. A. Ricci, and A. K. Soper, J. Chem. Phys. **120**, 10154 (2004).

[67] S. Imberti et al., J. Chem. Phys. **122**, 194509 (2005).

[68] S. E. McLain et al., Phys. Rev. B **74**, 094201 (2006).

[69] T. Megyes et al., J. Chem. Phys. **128**, 044501 (2008).

[70] R. Vácha, T. Megyes, I. Bakó, L. Pusztai, and P. Jungwirth, J. Phys. Chem. A **113**, 4022 (2009).

[71] K. T. Wikfeldt, M. Leetmaa, M. P. Ljungberg, A. Nilsson, and L. G. M. Pettersson, J. Phys. Chem. B **113**, 6246 (2009).

[72] M. Śmiechowski and J. Stangret, J. Phys. Chem. A **111**, 2889 (2007).

[73] M. Śmiechowski and J. Stangret, J. Mol. Struct. **834**, 239 (2007).

[74] M. P. Ljungberg, A. P. Lyubartsev, A. Nilsson, and L. G. M. Pettersson, J. Chem. Phys. **131**, 034501 (2009).

[75] J. D. Smith et al., Proc. Natl. Acad. Sci. USA **102**, 14171 (2005).

[76] H. S. Lee and M. E. Tuckerman, J. Chem. Phys. **126**, 164501 (2007).

[77] S. T. Roberts et al., Proc. Natl. Acad. Sci. USA **106**, 15154 (2009).

[78] A. van der Kogel and M. Joiner, *Basic Clinical Radiobiology*, Oxford University Press, New York, 4th edition, 2009.

[79] R. W. Howell, Int. J. Radiat. Biol. **84**, 959 (2008).

[80] B. S. Teh, S. Y. Woo, and E. B. Butler, The Oncologist **4**, 433 (1999).

[81] D. J. Brenner and E. J. Hall, New Engl. J. Med. **357**, 2277 (2007).

[82] D. J. Kwekkeboom et al., J. Clin. Oncol. **23**, 2754 (2005).

[83] J. F. Hainfield, D. N. Slatkin, and H. M. Smilowitz, Phys. Med. Biol. **49**, N309 (2004).

[84] S. H. Cho, Phys. Med. Biol. **50**, N163 (2005).

[85] C. R. Patra, R. Bhattacharya, D. Mukhopadhyay, and P. Mukherjee, J. Biomed. Nanotechnol. **4**, 99 (2008).

[86] A. K. Pradhan et al., J. Phys. Chem. A **113**, 12356 (2009).

[87] D. Cabaret and C. Brouder, J. Phys.: Conf. Ser. **190**, 012003 (2009).

[88] C. Brouder, D. Cabaret, A. Juhin, and P. Sainctavit, Phys. Rev. B **81**, 115125 (2010).

[89] M. E. Tuckerman, Path integration via molecular dynamics, in *Quantum Simulations of Complex Many-Body Systems: From Theory to Algorithms*, volume 10 of *NIC Series*, page 269, John von Neumann Institute of Computing, Jülich, 2002.

[90] M. Nakamura et al., Phys. Rev. **178**, 80 (1969).

[91] M. Kato et al., J. Electron. Spectrosc. Relat. Phenom. **160**, 39 (2007).

[92] M. Coville and T. D. Thomas, Phys. Rev. A **43**, 6053 (1991).

[93] B. W. Yates et al., J. Synchrotron Radiat. **7**, 296 (2000).

[94] H. Köppel, F. X. Gadea, G. Klatt, J. Schirmer, and L. S. Cederbaum, J. Chem. Phys. **106**, 4415 (1997).

[95] G. Nicolas and F. X. Gadea, J. Chem. Phys. **111**, 10537 (1999).

[96] C. Kolczewski et al., J. Chem. Phys. **115**, 6426 (2001).

[97] A. B. Trofimov, T. E. Moskovskaya, E. V. Gromov, H. Koppel, and J. Schirmer, Phys. Rev. A **64**, 022504 (2001).

[98] A. B. Trofimov et al., J. Phys. B: At. Mol. Opt. Phys. **36**, 3805 (2003).

[99] D. Duflot, J.-P. Flament, I. C. Walker, J. Heinesch, and M.-J. Hubin-Franskin, J. Chem. Phys. **118**, 1137 (2003).

[100] I. Minkov et al., J. Chem. Phys. **121**, 5733 (2004).

[101] I. Minkov et al., J. Phys. Chem. A **109**, 1330 (2005).

[102] S. Carniato, R. Taïeb, E. Kukk, Y. Luo, and B. Brena, J. Chem. Phys. **123**, 214301 (2005).

[103] D. Duflot, S. Zeggari, and J.-P. Flament, Chem. Phys. **327**, 518 (2006).

[104] D. Duflot, J.-P. Flament, A. Giuliani, J. Heinesch, and M.-J. Hubin-Franskin, Int. J. Mass Spectrom. **277**, 70 (2008).

[105] V. Ilakovac et al., Phys. Rev. A **77**, 012516 (2008).

[106] G. Herzberg, *Spectra of Diatomic Molecules*, Van Nostrand Reinhold Co., New York, 2nd edition, 1950.

[107] D. A. McQuarrie, *Quantum Chemistry*, University Science Books, Sausalito, CA, 1983.

[108] J. L. McHale, *Molecular Spectroscopy*, Prentice-Hall, Inc., Upper Saddle River, NJ, 1999.

[109] C. T. Chen, Y. Ma, and F. Sette, Phys. Rev. A **40**, 6737 (1989).

[110] R. J. LeRoy, Y. Huang, and C. Jary, J. Chem. Phys. **125**, 164301 (2006).

[111] T. Bally and G. N. Sastry, J. Phys. Chem. A **101**, 7923 (1997).

[112] D. T. Colbert and W. H. Miller, J. Chem. Phys. **96**, 1982 (1992).

[113] R. J. Gdanitz, Chem. Phys. Lett. **283**, 253 (1998).

[114] Y. Shao et al., Phys. Chem. Chem. Phys. **8**, 3172 (2006).

[115] G. Herzberg and H. C. Longuet-Higgins, Discuss. Faraday Soc. **35**, 77 (1963).

[116] J. Wang and R. M. Hochstrasser, J. Phys. Chem. B **110**, 3798 (2006).

[117] C. R. Jacob and M. Reiher, J. Chem. Phys. **130**, 084106 (2009).

[118] F. A. Cotton, *Chemical Applications of Group Theory*, John Wiley & Sons, New York, 3rd edition, 1990.

[119] R. Zwanzig, Annu. Rev. Phys. Chem. **16**, 67 (1965).

[120] P. H. Berens and K. R. Wilson, J. Chem. Phys. **74**, 4872 (1981).

[121] J. S. Bader and B. J. Berne, J. Chem. Phys. **100**, 8359 (1994).

[122] S. A. Egorov, K. F. Everitt, and J. L. Skinner, J. Phys. Chem. A **103**, 9494 (1999).

[123] H. Ahlborn, B. Space, and P. B. Moore, J. Chem. Phys. **112**, 8083 (2000).

[124] W. H. Miller, J. Chem. Phys. **125**, 132305 (2006).

[125] G.-C. Wick, Phys. Rev. **96**, 1124 (1954).

[126] R. P. Feynman and A. R. Hibbs, *Quantum Mechanics and Path Integrals*, McGraw-Hill Book Company, New York, 1st edition, 1965.

[127] H. F. Trotter, P. Am. Math. Soc. **10**, 545 (1959).

[128] M. Parrinello and A. Rahman, J. Chem. Phys. **80**, 860 (1984).

[129] K. S. Schweitzer, R. M. Stratt, D. Chandler, and P. G. Wolynes, J. Chem. Phys. **75**, 1347 (1981).

[130] M. E. Tuckerman, B. J. Berne, and G. J. Martyna, J. Chem. Phys. **97**, 1990 (1992).

[131] M. E. Tuckerman, B. J. Berne, G. J. Martyna, and M. L. Klein, J. Chem. Phys. **99**, 2796 (1993).

[132] H. C. Andersen, J. Chem. Phys. **72**, 2384 (1980).

[133] G. J. Martyna, M. L. Klein, and M. E. Tuckerman, J. Chem. Phys. **97**, 2635 (1992).

[134] G. J. Martyna, M. E. Tuckerman, D. J. Tobias, and M. L. Klein, Mol. Phys. **87**, 1117 (1996).

[135] M. E. Tuckerman, Y. Liu, G. Ciccotti, and G. J. Martyna, J. Chem. Phys. **115**, 1678 (2001).

[136] M. F. Herman, E. J. Bruskin, and B. J. Berne, J. Chem. Phys. **76**, 5150 (1982).

[137] T. M. Yamamoto, J. Chem. Phys. **123**, 104101 (2005).

[138] R. W. Hall and B. J. Berne, J. Chem. Phys. **81**, 3641 (1984).

[139] A. Pérez, M. E. Tuckerman, and M. H. Müser, J. Chem. Phys. **130**, 184105 (2009).

[140] M. P. Allen and D. J. Tildesley, *Computer Simulation of Liquids*, Clarendon Press, Oxford, 1st pbk. edition, 1989.

[141] G. Jacucci and A. Rahman, Il Nuovo Cimento **4D**, 341 (1984).

[142] J. R. Taylor, *An Introduction to Error Analysis: The Study of Uncertainties in Physical Measurements*, University Science Books, Sausalito, CA, 2nd edition, 1997.

[143] R. Kubo, J. Phys. Soc. Jpn. **12**, 570 (1957).

[144] B. J. Braams and D. E. Manolopoulos, J. Chem. Phys. **125**, 124105 (2006).

[145] J. Cao and G. A. Voth, J. Chem. Phys. **101**, 6168 (1994).

[146] T. D. Hone, P. J. Rossky, and G. A. Voth, J. Chem. Phys. **124**, 154103 (2006).

[147] T. F. Miller, III and D. E. Manolopoulos, J. Chem. Phys. **122**, 184503 (2005).

[148] T. F. Miller, III, D. E. Manolopoulos, P. A. Madden, M. Konieczny, and H. Oberhofer, J. Chem. Phys. **122**, 057101 (2005).

[149] I. R. Craig and D. E. Manolopoulos, Chem. Phys. **322**, 236 (2005).

[150] M. Boninsegni, Phys. Rev. B **79**, 174023 (2009).

[151] T. E. Markland, S. Habershon, and D. E. Manolopoulos, J. Chem. Phys. **128**, 194506 (2008).

[152] T. F. Miller, III and D. E. Manolopoulos, J. Chem. Phys. **123**, 154504 (2005).

[153] S. Habershon, B. J. Braams, and D. E. Manolopoulos, J. Chem. Phys. **127**, 174108 (2007).

[154] T. E. Markland and D. E. Manolopoulos, J. Chem. Phys. **129**, 024105 (2008).

[155] B. J. Braams, T. F. Miller, III, and D. E. Manolopoulos, Chem. Phys. Lett. **418**, 175 (2005).

[156] S. Habershon, G. S. Fanourgakis, and D. E. Manolopoulos, J. Chem. Phys. **129**, 074501 (2008).

[157] I. R. Craig and D. E. Manolopoulos, J. Chem. Phys. **122**, 084106 (2005).

[158] I. R. Craig and D. E. Manolopoulos, J. Chem. Phys. **123**, 034102 (2005).

[159] R. Collepardo-Guevara, Y. V. Suleimanov, and D. E. Manolopoulos, J. Chem. Phys. **130**, 174713 (2009).

[160] R. Collepardo-Guevara, I. R. Craig, and D. E. Manolopoulos, J. Chem. Phys. **128**, 144502 (2008).

[161] T. F. Miller, III, J. Chem. Phys. **129**, 194502 (2008).

[162] A. R. Menzeleev and T. F. Miller, III, J. Chem. Phys. **132**, 034106 (2010).

[163] J. Cao and G. A. Voth, J. Chem. Phys. **100**, 5093 (1994).

[164] J. Cao and G. A. Voth, J. Chem. Phys. **100**, 5106 (1994).

[165] S. D. Ivanov, A. Witt, M. Shiga, and D. Marx, J. Chem. Phys. **132**, 031101 (2010).

[166] J. Liu et al., J. Chem. Phys. **131**, 164509 (2009).

[167] J. O. Richardson and S. C. Althorpe, J. Chem. Phys. **131**, 214106 (2009).

[168] W. H. Miller, unpublished notes, July 2005.

[169] D. Cruz-Uribe and C. J. Neugebauer, J. Inequal. Pure and Appl. Math. **3**, 49 (2002).

[170] H. Wang, X. Sun, and W. H. Miller, J. Chem. Phys. **108**, 9726 (1998).

[171] L. Gaul, S. Bohlen, and S. Kempfle, Mech. Res. Commun. **12**, 187 (1985).

[172] C. Venkataraman, private communication, April 2006.

[173] L. Wittgenstein, *Tractatus Logico-Philosophicus*, Cosimo, Inc., New York, 2007.

[174] D. W. Marquardt, J. SIAM **11**, 431 (1963).

[175] T. Williams et al., GNUPLOT, `http://www.gnuplot.info`, (Online; accessed 28$^{\text{th}}$ June, 2010).

[176] P. M. Morse, Phys. Rev. **34**, 57 (1929).

[177] C. L. Pekeris, Phys. Rev. **45**, 98 (1934).

[178] C. Berkdemir and J. Han, Chem. Phys. Lett. **409**, 203 (2005).

[179] Wikipedia contributors, Voigt profile — Wikipedia, the free encyclopedia, `http://en.wikipedia.org/w/index.php?title=Voigt_profile`, (Online; accessed 28th June, 2010).

[180] J. J. Olivero and R. L. Longbothum, J. Quant. Spectrosc. Ra. **17**, 233 (1977).

[181] G. K. Wertheim, M. A. Butler, K. W. West, and D. N. E. Buchanan, Rev. Sci. Instrum. **45**, 1369 (1974).

[182] K. S. Kölbig, CWERF, `http://cernlib.web.cern.ch/cernlib/download/2006_source/src/mathlib/gen/c/cwerf64.F`, (Online; accessed 28th June, 2010).

[183] W. Gautschi, SIAM J. Numer. Anal. **7**, 187 (1970).

[184] K. S. Kölbig, Comm. ACM **15**, 465 (1972).

[185] W. Gautschi, Error Function and Fresnel Integrals, in *Handbook of Mathematical Functions with Formulas, Graphs, and Mathematical Tables*, edited by M. Abramowitz and I. A. Stegun, chapter 7, page 295, Dover Publications, Inc., New York, 1972.